

Integrated metamaterials and nanophotonics in CMOS-compatible materials

A thesis presented

by

Orad Reshef

to

The School of Engineering and Applied Sciences

in partial fulfillment of the requirements

for the degree of

Doctor of Philosophy

in the subject of

Applied Physics

Harvard University

Cambridge, Massachusetts

August 2016

©2016 - Orad Reshef

All rights reserved.

Thesis advisor

Eric Mazur

Author

Orad Reshef

Integrated metamaterials and nanophotonics in CMOS-compatible materials

Abstract

This thesis explores scalable nanophotonic devices in integrated, CMOS-compatible platforms. Our investigation focuses on two main projects: studying the material properties of integrated titanium dioxide (TiO_2), and studying integrated metamaterials in silicon-on-insulator (SOI) technologies.

We first describe the nanofabrication process for TiO_2 photonic integrated circuits. We use this procedure to demonstrate polycrystalline anatase TiO_2 ring resonators with high quality factors. We measure the thermo-optic coefficient of TiO_2 and determine that it is negative, a unique property among CMOS-compatible dielectric photonic platforms. We also derive a transfer function for ring resonators in the presence of reflections and demonstrate using full-wave simulations that these reflections produce asymmetries in the resonances.

For the second half of the dissertation, we design and demonstrate an SOI-based photonic-Dirac-cone metamaterial. Using a prism composed of this metamaterial, we measure its index of refraction and unambiguously determine that it is zero. Next, we take a single channel of this metamaterial to form a waveguide. Using interferometry, we independently confirm that the waveguide in this configuration preserves

the dispersion profile of the aggregate medium, with a zero phase advance. We also characterize the waveguide, determining its propagation loss. Finally, we perform simulations to study nonlinear optical phenomena in zero-index media. We find that an isotropic refractive index near zero relaxes certain phase-matching constraints, allowing for more flexible configurations of nonlinear devices with dramatically reduced footprints.

The outcomes of this work enable higher quality fabrication of scalable nanophotonic devices for use in nonlinear applications with passive temperature compensation. These devices are CMOS-compatible and can be integrated vertically for compact, device-dense industrial applications. It also provides access to a versatile, scalable and integrated medium with a refractive index that can be continuously engineered between $n = -0.20$ and $n = +0.50$. This opens the door to applications in high-precision interferometry, sensing, quantum information technologies and compact nonlinear applications.

Contents

Title Page	i
Abstract	iii
Table of Contents	v
List of Figures	viii
List of Tables	x
Citations to previously published work	xi
Acknowledgments	xiii
Dedication	xviii
1 Introduction	1
1.1 Organization of the dissertation	3
2 Nanofabrication of TiO₂ waveguides	5
2.1 Introduction	5
2.2 Fabrication process	6
2.3 Optimizations in electron-beam lithography	10
2.3.1 Resist selection	10
2.3.2 Spinning of HDMS to protect from humidity	11
2.3.3 Multi-pass exposure	12
2.3.4 Cold development	13
2.4 Optimizations in the etch mask	15
2.4.1 Etch mask material selection	15
2.4.2 Chromium deposition optimization	17
2.4.3 Lift-off recipe	19
2.4.4 Treatment prior to metal mask removal	19
2.5 Improvements to the etch procedure	21
2.5.1 Recipe optimization	21
2.5.2 Etch rate estimation with AFM	22
2.6 Cleaving the sample	23
2.7 Conclusion	25

3 Anatase ring resonators with negative thermo-optic coefficient	26
3.1 Introduction	27
3.2 Theory	28
3.2.1 Transmission characteristics of a micro-ring resonator	28
3.2.2 Effective thermo-optic coefficients	30
3.3 Experimental	32
3.3.1 Fabrication	32
3.3.2 Measurement setup	33
3.4 Results	33
3.5 Discussion and conclusion	37
4 Asymmetric resonances in micro-ring resonators	43
4.1 Introduction	44
4.2 Theory	45
4.2.1 Standard symmetric transfer function	45
4.2.2 Asymmetric transfer function	47
4.2.3 Asymmetry threshold	50
4.3 Results and Discussion	51
4.3.1 Device geometry and simulation parameters	51
4.3.2 Symmetric resonances	52
4.3.3 Asymmetric resonances	53
4.4 Conclusion	57
5 CMOS-compatible zero-index metamaterials	59
5.1 Introduction to zero-index metamaterials based on photonic Dirac cones	60
5.2 Dirac cones in square arrays of holes in a dielectric matrix	62
5.3 Dirac cones in silicon-on-insulator technologies	64
5.4 Effective refractive index determination	70
5.4.1 Parameter retrieval	70
5.4.2 Experimental verification	71
5.5 Discussion and conclusion	73
6 Zero-index waveguides	76
6.1 Introduction	76
6.2 Design and simulation	78
6.2.1 On-chip photonic band gap materials	78
6.2.2 Waveguide propagation	79
6.3 Experimental	82
6.3.1 Fabrication	82
6.3.2 Index retrieval	82
6.3.3 Propagation loss	88
6.4 Conclusion	89

7 Towards simultaneous phase matching in zero-index metamaterials	90
7.1 Introduction	91
7.1.1 Phase matching in nonlinear optics	91
7.1.2 Simultaneous phase matching in isotropic zero-index media	94
7.2 Theory	96
7.2.1 Effects of dispersion on phase matching	96
7.2.2 Coherence length	99
7.2.3 Dispersion profile and related coherence length for zero-index metamaterials	101
7.3 Simulations	102
7.3.1 Nonlinear scattering theory in bulk materials	102
7.3.2 Phase-matching in photonic Dirac-cone-based ZIMs	103
7.3.3 Nonlinear finite-difference time-domain simulations	104
7.4 Conclusion	108
8 Summary and outlook	109
A Nonlinear scattering theory	114
A.1 Introduction	114
A.2 Solution to the inhomogeneous wave equation with a source current .	115
A.3 Lorentz reciprocity theorem	116
A.4 Example 1: A Hertzian dipole source	118
A.5 Example 2: A plane wave source	120
A.6 Second Harmonic Generation in a 1D nonlinear medium	121
Bibliography	124

List of Figures

2.1	Fabrication process for TiO ₂ nanophotonic devices	7
2.2	Comparison between photoresists	10
2.3	Effects of multi-pass exposure on line edge roughness	12
2.4	Example of line edge roughness reduction due to cold development . .	13
2.5	Effects of cold development on line edge roughness	14
2.6	Comparison between etch masks	16
2.7	SEM comparing different deposition rates of Cr	18
2.8	AFM comparing different deposition rates of Cr	18
2.9	Effect of descumming treatment prior to metal mask removal	20
2.10	Etch rate estimation with AFM	22
2.11	Cleaving a sample	24
2.12	A fabricated anatase TiO ₂ waveguide	25
3.1	Fabricated anatase ring resonator	31
3.2	Performance of anatase TiO ₂ ring resonators	34
3.3	Effective of temperature on resonance wavelength	35
4.1	Schematic of ring resonator surrounded by reflectors	45
4.2	Extracting propagation losses from ring resonators	54
4.3	Effect of stitching errors	54
4.4	Extracted propagation losses for resonances in the presence of asymmetries	55
5.1	The band structure of a two-dimensional square lattice photonic crystal (reproduced from Ref. [97])	60
5.2	Photonic Dirac cones in square arrays of holes in bulk silicon (2D calculation)	63
5.3	Photonic Dirac cones in SOI (3D calculation)	65
5.4	Sensitivity of modal degeneracy to fabrication imperfections	66
5.5	3D Dispersion surface for an SOI-based photonic Dirac cone	68
5.6	Equifrequency contours for an SOI-based photonic Dirac cone	69
5.7	Retrieved complex refractive index for an SOI-based photonic Dirac cone	71

5.8	Prism experiment schematic	72
5.9	Far-field patterns	73
6.1	1-channel-wide zero-index waveguides	80
6.2	FDTD simulations of zero-index waveguides	81
6.3	Fabricated zero-index waveguides	83
6.4	Effective refractive index extraction procedure	86
6.5	Absolute value of the effective refractive index of a 1-channel-wide zero-index waveguide	87
6.6	Propagation losses for a 1-channel-wide zero-index waveguide	88
7.1	Phase-matching in bulk media	92
7.2	A silicon-based zero-index metamaterial coupled to a standard silicon-on-insulator waveguide	94
7.3	Four equivalent phase-matching configurations for four-wave mixing in a zero-index metamaterial	95
7.4	Dispersion properties for integrated zero-index metamaterials	101
7.5	Verification of nonlinear scattering theory in bulk media	103
7.6	Calculated band structures for 2-dimensional Dirac cone metamaterials	103
7.7	Generated nonlinear signal in photonic Dirac-cone-based zero-index metamaterials	104
7.8	Nonlinear finite-difference time-domain simulation of zero-index waveguide	106
A.1	Comparison between direct solutions of the nonlinear wave equation and nonlinear scattering theory (reproduced from Ref. [44])	123

List of Tables

2.1	HDMS spin parameters	8
2.2	ZEP 520a spin parameters	8
2.3	CYTOP polymer spin parameters	9
2.4	Shipley S1822 spin parameters	10
2.5	Surface roughnesses and sheet resistivities for the deposited Cr films .	19
2.6	Metal lift-off procedure for Cr on TiO ₂	20
2.7	Etch recipe for pattern transfer from Cr to TiO ₂	21
3.1	Free spectral range and propagation losses near $\lambda = 1550$ nm for different devices and coupling gaps	36
3.2	Simulated power confinement factors for a 900×250 nm TiO ₂ waveguide	37
4.1	Device geometry	52

Citations to previously published work

Parts of this dissertation cover research reported in the following articles:

1. J. D. B. Bradley, C. C. Evans, J. T. Choy, O. Reshef, P. B. Deotare, F. Parsy, K. C. Phillips, M. Lončar, and E. Mazur, “Submicrometer-wide amorphous and polycrystalline anatase TiO₂ waveguides for microphotonic devices,” *Optics Express*, **20**, 23821-31, 2012.
2. C. C. Evans, K. Shtyrkova, J. D. B. Bradley, O. Reshef, E. Ippen and E. Mazur, “Spectral broadening in anatase titanium dioxide waveguides at telecommunication and near-visible wavelengths,” *Optics Express*, **21**, 18582-91, 2013.
3. L. Jiang, C. C. Evans, O. Reshef and E. Mazur, “Optimizing anatase-TiO₂ deposition for low-loss waveguides.,” *Proc. SPIE - Oxide-based Materials and Devices IV*, **86261D-8**, San Francisco, California, 2013.
4. C. C. Evans, K. Shtyrkova, O. Reshef, M. G. Moebius, J. D. B. Bradley, S. Griesse-Nascimento, E. Ippen and E. Mazur, “Multimode phase-matched third-harmonic generation in sub-micrometer-wide anatase TiO₂ waveguides,” *Optics Express*, **23**, 7832-41, 2015.
5. O. Reshef, K. Shtyrkova, M. G. Moebius, S. Griesse-Nascimento, S. Spector, C. C. Evans, E. Ippen and E. Mazur, “Polycrystalline anatase titanium dioxide micro-ring resonators with negative thermo-optic coefficient,” *Journal of the Optical Society of America B*, **32**, 2288-2293, 2015.

6. Y. Li*, S. Kita*, P. Muñoz, O. Reshef, D. I. Vulis, M. Lončar, and E. Mazur, "On-chip zero-index metamaterials," *Nature Photonics*, **9**, 738-742, 2015.
7. M. G. Moebius, F. Herrera, S. Griesse-Nascimento, O. Reshef, C. C. Evans, G. G. Guerreschi, A. Aspuru-Guzik, and E. Mazur, "Efficient photon triplet generation in integrated nanophotonic waveguides," *Optics Express*, **24**, 9932-54, 2016.
8. O. Reshef, Y. Li, M. Yin, L. Christakis, D. I. Vulis, P. Camayd-Muñoz, S. Kita, M. Lončar, and E. Mazur, "Phase-Matching in Dirac-Cone-Based Zero-Index Metamaterials," *CLEO: Applications and Technology JTU5A.53* San Jose, CA, 2016.
9. O. Reshef, M. G. Moebius, and E. Mazur. "Asymmetric resonances in micro-ring resonators due to accidental reflections," *Under review*, 2016.
10. S. Kita, Y. Li, P. Camayd-Muñoz, O. Reshef, D. I. Vulis, R. W. Day, E. Mazur, and M. Lončar, "On-chip all-dielectric fabrication-tolerant zero index metamaterials," *Under review*, 2016.
11. Y. Li*, D. I. Vulis*, O. Reshef*, P. Camayd-Muñoz, M. Yin, S. Kita, M. Lončar, and E. Mazur, "Monolithic integrated zero-index metamaterials," *Under review*, 2016.
12. O. Reshef*, P. Camayd-Muñoz*, D. I. Vulis, Y. Li, E. Mazur, and M. Lončar, "Observing phase-free propagation in integrated zero-index waveguides," *Manuscript in preparation*.

Acknowledgments

Life is what happens when you're busy making other plans.

— “Beautiful Boy” by John Lennon, *Double Fantasy* (1980)

I cannot believe that it is finally time to submit my thesis. No pressure. Well, I guess a little bit of pressure — I’m fully well aware that there is a nonzero chance that this page will be the only part that ever gets read by anyone. While you’re here, I recommend you skim through the conclusion as well, since that summarizes the next hundred or so pages and gives a bit of insight on potential future research directions.

First, I would like to thank my wife Stephanie, to whom this thesis is dedicated. I don’t know how I convinced you to come along on this wild ride with me, but your support, especially in the most stressful times, has played a key role in all of my successes at Harvard. I also cannot thank you enough for what you have sacrificed for my work and my career. I will never forget it.

Next, of course, I want to thank my advisor Eric Mazur. The Mazur group definitely provides its students with opportunities for unique experiences. As a member of the group (and as such, the extended Mazur group family), I have been extremely fortunate to share many of these kinds of experiences (in the lab, at Eric’s house, in the wilderness, *etc*). Eric has given me an incredible sense of independence and ownership over my work, and he has taught me about his very refined sense of experimental taste. (*Orad, it’s interesting, I guess... the signal is not obvious. What could we do to make it more obvious?*) Eric, your voice will be resonating within my head for the rest of my career. Thank you for everything.

In the Mazur group, I have too many people to name and thank, but I’ll try. I begin with a special thanks to my senior graduate students and postdoc mentors:

Chris Evans, Jon Bradley, Paul Peng and Yang Li. I have waited six years to be able to name you here in person to thank you by name. I'll also never forget a few key pieces of advice that Julie Schell, Valeria Nuzzo, Brian Lukoff, Jason Dowd, Yu-Ting Lin and Sally Kang have given me when I was struggling. Phil Muñoz (and Grant England, our third musketeer), Kasey Philips (and Alex, as always), Michael Moebius, Daryl Vulis, and Sébastien Courvoisier, you guys were all the greatest of friends during trying times. Kelly Miller, Benjamin Franta and Alex Raymond, thank you for your friendship in the tryingest times. Phil, you were my partner in crime, both in the lab and in the bar. I'm especially looking forward to seeing what you will produce in the next chapter of your career. As for the remaining group members (Sarah, Nabiha, Marinna, Olivia, Hemi, Weilu and more, including the temporary ones like Lili, Dario and Lysander), I will always be your loud Canadian brother. Let me know if you ever need anything.

The Lončar group has been my second family during my time at Harvard. Birgit Hausmann, Anna Schneidman, Parag Deotare, Mike Burek, Jennifer Choy, Paweł, Srujan, Young-ik, *etc.* You guys have welcomed me into your lab with open arms. Shota Kita, you are a god among men, and it was an absolute pleasure to work with you. All of the Hu group members and Capasso group members, of which there are way too many to mention (Christine Zgrabik, Shanying Cui, Mikael Kats to name a few) have also been incredible sources of inspiration and friendship (and sometimes, really accurate ellipsometric data) for me during my PhD. To my other collaborators at Harvard (the Aspuru-Guzik group), at MIT (Katia and Erich Ippen) and at Lincoln Labs, thank you for all of the hard work. Katia, thank you especially

for all of the training you didn't realize you were giving me, and for your friendship in my times of need. I look forward to reading the great things all of you will produce in the future.

All of you guys at CNS (JD Deng, Mac Hathaway, John Tsakirgis, Steve Paolini, Dave Lafleur, Jason Tresback, Dave Lange, Ling Xie, Ameha Gebreyohannes, Guixiong Zhong, Yuan Lu, Arthur McClelland and last but not least Ed Macomber) are absolute angels for dealing with us users. Thank you for all that you do to keep the cleanroom running (*especially* the RIE), and thanks for the patience in responding to my never-ending questions. I am a greater researcher and fabber for it. We all appreciate you even if we don't tell you that every day.

Last but not least, I would like to thank my parents. You have always been caring and supportive of my work and my ambitions. In fact, I'm not even sure that I know about all that you have done to get me to where I am today. It seems to me, however, that whatever it was — you did good. I have read before that, "we don't accomplish anything in this world alone... and whatever happens is the result of the whole tapestry of one's life and all the weavings of individual threads from one to another that creates something." Thank you for working so *so* hard on my tapestry. All of my success is your success, and I hope I have made you proud. I love you.

To the younger graduate students who have accidentally stumbled upon this paragraph while going through this thesis somewhere in the future, I leave the following advice: don't worry, work hard, and be a good person. As long as you keep your head down and your mind open, you'll be ok. (Isn't that how you got into grad school in the first place? And weren't you also worried when you were an undergrad?)

It worked out, right? How quickly did you forget that lesson?) It's certainly hard to see it that way when you're in the thick of it, but trust me — 75% of the work in this dissertation was completed while I was trying to develop other things, and yet it still developed into a cohesive story of which I'm still so very proud. As hard as you try (and as much as you might want to) you can't always just *will* an experiment into existence. Just do your best. Your peers will know.

Orad Reshef

September 8, 2016

Ottawa, Ontario

Acknowledgements of Financial Support

This thesis is based on work funded by the National Science Foundation under contracts ECCS-0901469, ECCS-1201976, PHY-1415236 and DMR-1360889, the Fonds de recherche du Québec – Nature et technologies, the Natural Sciences and Engineering Research Council of Canada, the Harvard Quantum Optics Center, the Air Force Office of Scientific Research under contracts FA8721-05-C-0002, FA9550-12-1-0499 and FA9550-14-1- 0389, the Harvard Graduate Prize Fellowship, the Kavli Institute at Cornell for Nanoscale Science Postdoctoral Fellowship, the National Defense Science and Engineering Graduate Fellowship under contract 32 CFR 168a and the National Science Foundation Graduate Research Fellowship Program under contract DGE1144152. This work could not be accomplished without the use of the facilities in the Center for Nanoscale Systems, which was supported by the National Science Foundation's National Nanotechnology Infrastructure Network and which is now a member of the National Nanotechnology Coordinated Infrastructure Network

(NNCI), which is supported by the National Science Foundation under NSF award no. 1541959. CNS is part of Harvard University.

*To my loving and supportive wife, Stef, who has dedicated as much of her life to this
work as I have. Thank you, Love.*

Chapter 1

Introduction

The field of integrated optics began with the promise of replacing electronics. Optical waveguiding had been shown to be intrinsically lossless due to its lack of Ohmic heating [1, 2]. This fact had already been exploited to great effect for long-haul communications, where optical fibers routed information literally around the world. The hope had been that the move from integrated circuits to photonic integrated circuits would decrease the total power consumption of consumer devices, with potential increases to cost effectiveness and operating speeds [3, 4].

To date, replacing electronics in shorter range communications has proven to be a challenging, and perhaps even misguided pursuit. The consensus has become that photonics will play a complementary role to electronic circuits instead of evolving into a complete replacement for our everyday information technology needs [5]. Nevertheless, many interesting and unforeseen fundamental questions and applications have been explored with the introduction of nanophotonics, such as photonic crystal cavities, on-chip frequency combs and non-volatile optomechanical-memory [6–8].

Like the move from transistors to the integrated circuit, bulky free-space optical phenomena have been dramatically reduced in scale and integrated onto a chip. These devices can be mass-produced and have the greatest opportunity to make an immediate impact on society.

So far, research and development in integrated photonics have mainly focused on the silicon-on-insulator (SOI) platform [9–11]. Silicon is cheap, abundant, nontoxic, and already has established fabrication capabilities bolstered by the semiconductor industry [12]. It also has many attractive optical properties, such as a large linear and nonlinear index of refraction [13]. For these reasons, silicon is still the dominant material platform for photonic demonstrations.

Many efforts have been made towards developing alternative materials for photonic applications, however. I have chosen to focus part of my dissertation on titanium dioxide (TiO_2). Like silicon, TiO_2 is an abundant, non-toxic semiconductor that has large linear and nonlinear coefficients [14–17]. In addition to these properties, TiO_2 is completely transparent in the visible spectrum down to $\lambda = 400 \text{ nm}$ and does not suffer from two-photon absorption or three-photon absorption in the telecom regime. These properties make it a promising platform for integrated nonlinear devices. Another interesting property of this material is its negative thermo-optic coefficient [18,19]. Other than TiO_2 , polymers are the only dielectric materials known to possess a negative thermo-optic coefficient [20]. This trait enables entirely passive temperature compensation, a critical property for sensitive interferometric applications.

Despite the fact that silicon as a material has its limitations, its mature fab-

rication ecosystem allows for the quick and easy exploration of different research ideas [21]. Currently, a popular area of research is to create sub-wavelength structures that can trick light into demonstrating properties that are not present in its constituent materials. These kinds of structures, called metamaterials, can even be designed to exhibit material responses that do not appear in nature, such as magnetic responses at optical frequencies [22,23], extremely small or negative indices of refraction [24,25], and tunable optical activity [26,27]. In the second half of my thesis, I exploit the ubiquity and fabrication precision of silicon photonics to demonstrate and explore an integrated metamaterial with a refractive index near zero.

A flexible integrated zero-index metamaterial enables many applications, including in quantum optics, interconnects and wavefront engineering [28–33]. Of particular interest to me are the unique nonlinear phenomena that are made possible by zero-index media [34,35]. Nonlinear effects are essential to fundamental optical phenomena and applications, such as frequency conversion and lasing [36,37]. For any nonlinear effect to develop efficiently, it must be phase-matched. A photon in a zero-index medium experiences no phase-advance during propagation, introducing a new degree of freedom to the standard phase-matching toolkit. In the final chapter of my thesis, I explore this idea theoretically and numerically.

1.1 Organization of the dissertation

In Chapter 2, we describe the fabrication procedure for TiO_2 photonic devices in detail. We then follow this procedure to fabricate photonic integrated circuits from a polycrystalline anatase TiO_2 thin film in Chapter 3. We use ring resonators to

evaluate the quality of the fabrication and to extract the thermo-optic coefficient for this material platform.

In Chapter 4, we derive and verify a generalized transfer function for an integrated ring resonator in the presence of back-reflections. Using full wave simulations, we compare the performance of this model to the transfer function of an ideal ring resonator.

In Chapter 5, we present an entirely silicon-based integrated zero-index metamaterial. We discuss how to design this metamaterial and we experimentally demonstrate this metamaterial. In Chapter 6, we fabricate and characterize a 1-dimensional waveguide formed of this metamaterial. In Chapter 7, we explore the behaviour of nonlinear interactions within zero-index structures.

In Chapter 8, we will summarize the results from this dissertation and provide context and potential research directions for future aspiring young researchers.

Finally, in Appendix A, we present and demonstrate nonlinear scattering theory, a nonlinear simulation method based on Lorentz reciprocity and the undepleted pump approximation.

Chapter 2

Nanofabrication of TiO₂ waveguides

We present the fabrication procedure for titanium dioxide photonic integrated circuits. We then provide the details on specific improvements to the lithography, the selection and deposition parameters of the etch mask, the etching process and the cleaving procedure. These improvements increase the fabrication yield, while producing smoother, higher quality features.

2.1 Introduction

Propagation losses in optical waveguides are a major consideration in designing photonic devices, particularly when discussing nonlinear pulse propagation. The loss in a waveguide originates from multiple sources, including film impurities and Rayleigh scattering. Reducing propagation losses is an active area of research when working with a new photonic platform such as titanium dioxide. Defects that produce losses in optical waveguides are introduced both during the deposition of the film, or during

the structuring process. Once the film has been deposited, there are many steps in the fabrication process that can each be optimized to ensure high quality fabrication and low propagation losses. In this chapter, we will focus on the many improvements to the waveguide-structuring process that have been developed in order to increase fabrication quality, produce smoother features, and increase the fabrication yield.

First, we will describe the final completed fabrication process, including improvements to Bradley and Choy's original process described in their pioneering TiO₂ photonic papers [15,38]. In the following subsections we will discuss the improvements to the lithography (Section 2.3), the etch mask (Section 2.4) the etching procedure (Section 2.5) and the cleaving procedure (Section 2.6).

2.2 Fabrication process

The complete waveguide-fabrication process is illustrated in Fig. 2.1. We begin the structuring process by depositing a device layer of TiO₂ several hundred nm thick upon a thermally oxidized silicon wafer using radio frequency (RF) magnetron sputtering. The deposition parameters have remained unchanged since the original work of Bradley and Choy [15, 38]. The thickness can be tuned to suit the application and can yield both an amorphous or a polycrystalline anatase TiO₂ film. We cleave the samples into chips approximately 1.5 cm × 1.5 cm in size, and then solvent clean them. The cleaning procedure consists of 5 minutes in an acetone sonication bath, followed by 5 minutes in an isopropyl alcohol (IPA) sonication bath. The samples are then dried by blowing N₂ and are soft-baked on a hot plate at 180 °C for 10 minutes to remove any remaining moisture. The final step in the cleaning procedure consists

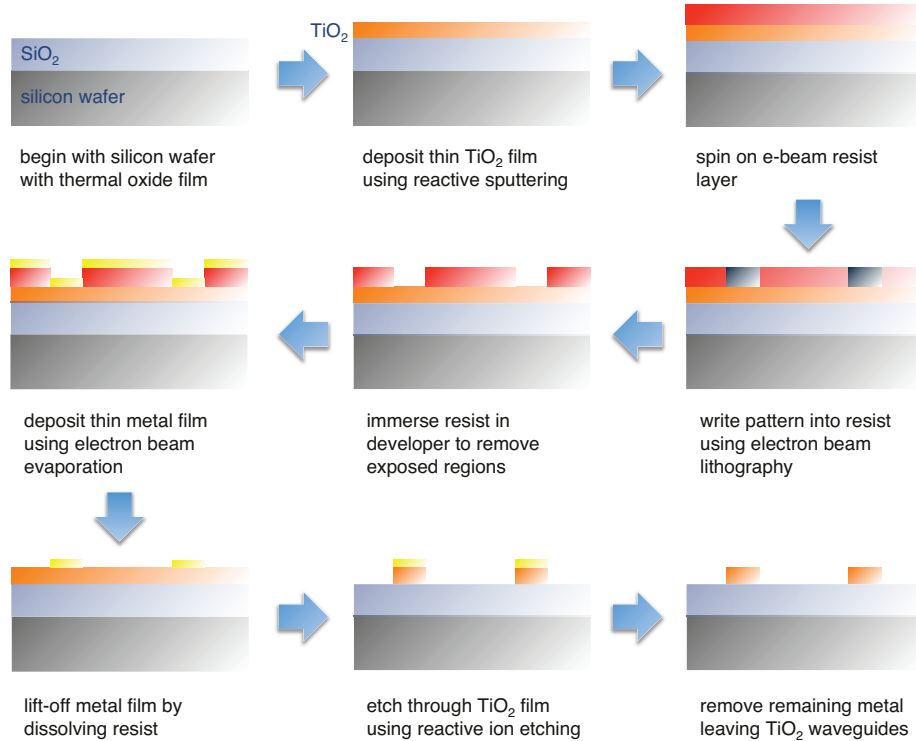


Figure 2.1: Fabrication process for TiO_2 nanophotonic devices.

of an O_2 descum, where we expose the sample to a flow of 40 sccm of oxygen plasma for 2 minutes at 80 W.

We spin-coat a layer of hexamethyldisilazane (HDMS), followed by ZEP-520a (Zeon Chemicals), a positive-tone resist. We then soft-bake the sample on a hot plate at 180°C for 3 minutes (spin parameters are listed in Tables 2.1 and 2.2). This produces a layer of resist that is about 250 nm thick.

For optical waveguides on the order of 300 nm wide, the correct charge area D is found to be near $480 \mu C/cm^2$. To obtain this dose, we select the following exposure parameters: we employ a current I of 12 nA, a write-window W_R of 500 μm , and $N = 50,000$ dots/line. This large current permits us to write 30 waveguides the length of the chip every 10 minutes. These parameters correspond to a dwell time t_d

Step	Time	Speed	Acceleration
1	45 s	5000 rpm	2500 rpm/s

Table 2.1: HDMS spin parameters. This should be done immediately when the sample is removed from the hot plate after the cleaning process. This is followed by the ordinary resist spin process (Table 2.2).

Step	Time	Speed	Acceleration
1	5 s	500 rpm	500 rpm/s
2	40 s	6000 rpm	1000 rpm/s

Table 2.2: ZEP 520a spin parameters. This is followed by 3 minutes on a hot plate set to 180°C. This yields a 250-nm-thick film.

of 0.04 μ s, which is calculated using

$$t_d = \frac{D}{I} \left(\frac{W_R}{N} \right)^2.$$

To reduce line-edge roughness, we write the pattern twice at half the dwell time, *e.g.*, $t_d = 0.02 \mu$ s $\times 2$ (see Sec. 2.3.3).

After exposure, the samples are developed at room temperature in ortho-xylene (o-xylene) for 30 seconds with a gentle agitation. This is followed by a stop bath in IPA.

Next, we deposit a 50-nm-thick layer of Chromium (Cr) at a rate of 5 Å/s using electron-beam evaporation (see Sec. 2.4.2). This layer will act as an etch mask. We perform lift-off using sonication in Remover PG (Microchem) at room temperature. Multiple cups of the solvent are used in order to avoid the redeposition of lifted material. This is followed by a quick rinse in acetone and IPA. This step leaves a Cr mask with the desired pattern above the TiO_2 layer.

Step	Time	Speed	Acceleration
1	5 s	500 rpm	500 rpm/s
2	40 s	2000 rpm	1000 rpm/s

Table 2.3: CYTOP polymer spin parameters. This is followed by 2 hours in an oven set to 200°C. Yields a 0.8 μm -thick film.

The pattern is transferred into the device layer using electron cyclotron resonance reactive plasma etching (Nexx Cirrus 150) in a $CF_4:H_2$ atmosphere, at a ratio of 4:1. This step is followed by another O_2 descum using the same parameters as in the cleaning procedure outlined above. The Cr is removed from the sample in a wet etch step using Cr etchant (Transene 1020, composed of nitric acid and ceric ammonium nitrate), followed by a rinse in multiple cups of distilled water.

A cladding is now optionally deposited. We deposit up to 4 μm of SiO_2 using plasma-enhanced chemical vapor deposition (Surface Technology Systems) or we spin-coat 1.5 μm of CYTOP polymer (see Table 2.3). These claddings are both used as a low-index guiding layer and a protective cladding. Alternatively, we may spin-coat the sample with a 2.6- μm -thick layer of positive-tone resist (Shipley S1822) to act as a protective layer (see Table 2.4).

The final step involves cleaving the facets to obtain access to the waveguides. If one has been deposited, the protective layer of resist is removed with a final quick solvent rinse, without sonication.

Step	Time	Speed	Acceleration
1	5 s	500 rpm	500 rpm/s
2	45 s	3000 rpm	1000 rpm/s

Table 2.4: Shipley S1822 spin parameters. This is followed by 1 minute on a hot plate set to 115°C. Yields a 2.6 μm -thick film, to be used as a protective layer.

2.3 Optimizations in electron-beam lithography

2.3.1 Resist selection

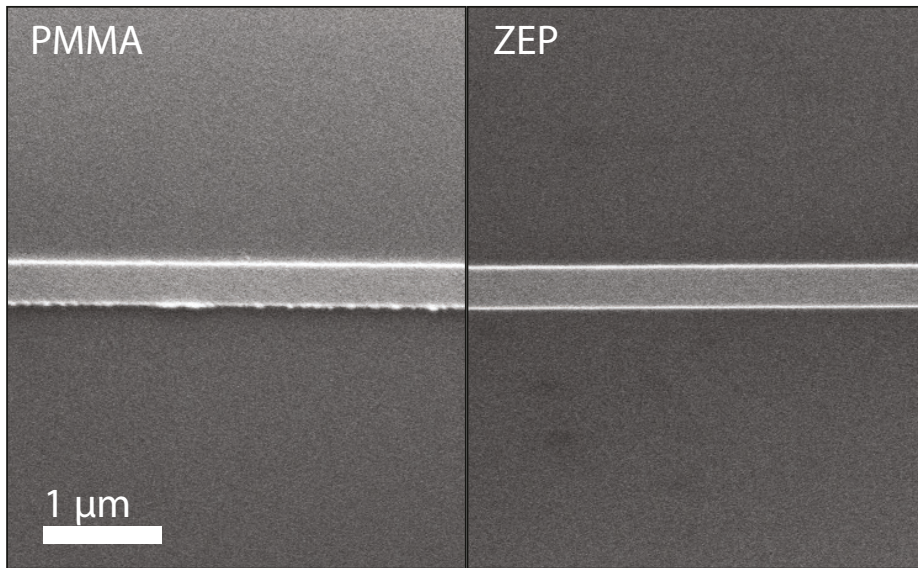


Figure 2.2: Comparison between photoresists. The sidewall that is produced using ZEP is much smoother than what is produced using PMMA as a positive-tone resist.

Instead of using ZEP 520a as our resist, we considered using polymethyl methacrylate (PMMA), which is also used as a positive-tone resist in electron-beam lithography processes [39, 40]. This resist is much more cost-effective than ZEP (\$700/L *vs.*

\$25,000/L) and can also employ the same reflow techniques that have been developed in ZEP in order to achieve smoother sidewalls [41–43]. Additionally, PMMA can be deposited with methyl methacrylate (MMA) as a bilayer to drastically aid in the liftoff process [44].

We compare the line edge roughness that is introduced by the different resists during the lithography step. We spin-coat two samples of amorphous TiO_2 with different configurations (ZEP, PMMA) and perform a dose test for a 350-nm-wide waveguide. Next, we deposit a Cr layer on all of the samples simultaneously to ensure identical processing conditions. We perform lift-off and image the residual Cr etch masks on the samples (Fig. 2.2).

Samples that were processed using ZEP produced considerably better results than samples that were processed using PMMA. The sidewalls are qualitatively much smoother when using ZEP. Additionally, the liftoff procedure worked more consistently. For these reasons, we have been using ZEP in all the subsequent fabrication, despite the additional cost.

2.3.2 Spinning of HDMS to protect from humidity

Often, the humidity in the cleanroom causes the resist to spin unevenly on samples, especially on the most humid days in the summer time. A solution is to spin an ultra-thin (~ 5 nm) layer of hexamethyldisilazane (HDMS) before spin-coating the sample with ZEP. Because of the thickness of the HDMS layer, this process does not drastically affect the doses or lift-off procedures.

2.3.3 Multi-pass exposure

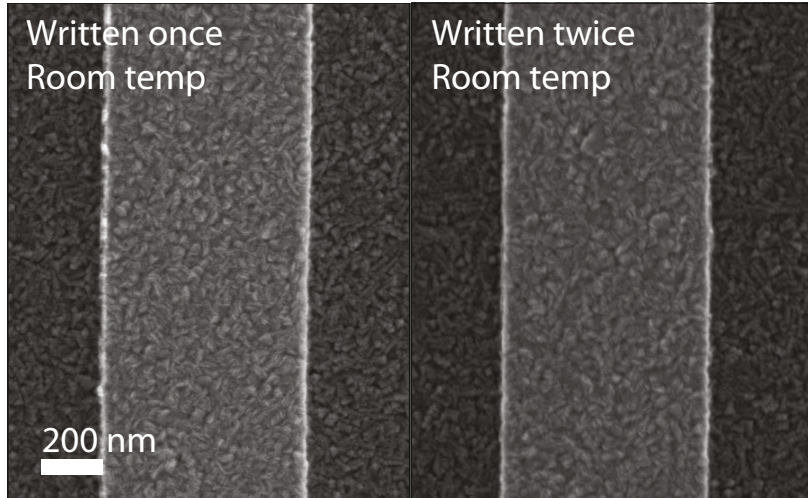


Figure 2.3: When a pattern is written in the resist twice at half the area dose (*i.e.*, the same total area dose), the sidewall that is obtained is smoother.

Due to the interaction between the many electron transport methods within the resist during the electron-beam lithography process, a line edge roughness is inherently introduced into the resist during exposure. We have found that re-writing the pattern multiple times mitigates this random roughness, leading to smoother sidewalls. To study this, we process a chip with the same pattern in two separate locations. In one location, we write a dose test at the full area dose. In the second location, we write half of this dose test twice. We develop the chip at room temperature, deposit a Cr layer and perform a lift-off procedure. By writing both sets of dose tests on the same chip, we ensure identical processing conditions for both sets of devices. In Fig. 2.3, we show a comparison between a pair of waveguides written with the same total area dose ($D = 480\mu C/cm^2$) with the different exposure schemes. The dimensions remain consistent for different devices written with the same total area dose, regardless of the exposure scheme. However, we find that waveguides written with a multi-pass

exposure scheme have a visibly smoother sidewall throughout the length of the device.

2.3.4 Cold development

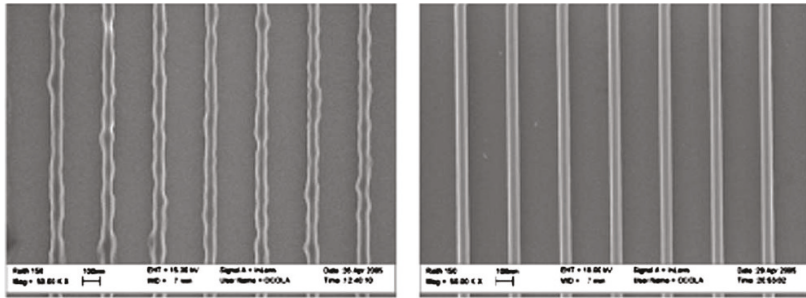


Figure 2.4: Example of line edge roughness reduction due to cold development. Left is ZEP developed at room temperature, right, is ZEP developed at -4°C . Feature sizes are 160 nm space and 40 nm line. Taken from Ocola et al. [39].

In 2006, Ocola *et al.* demonstrated that smaller and smoother features can be produced using resists that are exposed by polymer chain scission if the resists are developed at lower temperatures (*e.g.*, 0°C) after exposure [39]. Additionally, it was shown that the blur (*i.e.*, the standard deviation between the designed and fabricated feature size) is drastically reduced as well. For certain nonlinear applications, such as third-harmonic generation, it is often critically important to fabricate a device within a tolerance of only a few nanometres in order to satisfy phase-matching constraints [45, 46].

To test this, we process a pair of samples with identical dose tests. As in Section 2.3.3, we perform a multi-pass exposure in a second location to take advantage of the line edge roughness reduction, as well. We develop the first chip in o-xylene at room temperature and the second in a beaker of o-xylene that has been cooled in an ice bath. We then deposit a Cr layer and perform a lift-off procedure. We image

the resulting Cr masks using an SEM. We find that the total area dose required to achieve the desired feature size is much larger when the resist is developed at colder temperatures (800 *vs.* 480 $\mu\text{C}/\text{cm}^2$), as expected. In Fig. 2.5, we show SEMs comparing the Cr masks written by both single and multi-pass exposure, both developed at 0°C. We add the previous best result, written by multi-pass exposure and developed at room temperature, as an additional comparison.

We find that resist development at 0°C does in fact reduce the line edge roughness. However, it does not seem to improve upon the multi-pass exposure sample that is developed at room temperature. Additionally, developing a multi-pass exposure sample at 0°C does not further improve upon the roughness. For this reason, we have decided to continue developing the sample at room temperature.

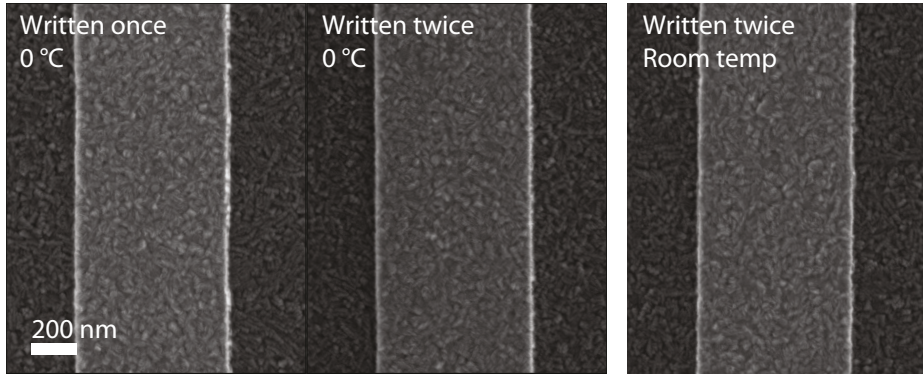


Figure 2.5: Developing ZEP in an ice bath yields a smoother line edge roughness. When compared with the line edge produced using multi-pass exposure, this improvement is comparatively less drastic.

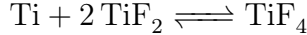
2.4 Optimizations in the etch mask

2.4.1 Etch mask material selection

The etch chemistry used in the dry etching step affects which etch mask material is ultimately selected. TiO_2 itself is inactive to fluorine or chlorine, the halogen gases we have available in the RIE, primarily due to the oxide component. In order to render it reactive, we need to add hydrogen gas to reduce TiO_2 to pure titanium:



Following this step, the titanium atoms can react with fluorine to form titanium tetrafluoride (TiF_4):



Thus, we need a mask that is resistant to being etched in a fluorine environment. Two candidate materials are alumina (Al_2O_3), first used in a fluorine environment by Henry *et al.* [47–49] and chromium (Cr), which was originally used by Bradley *et al.* in the original recipe [15, 38, 50]. Henry *et al.* claimed that sputtered Al_2O_3 would provide for a more faithful feature transfer than any metal liftoff process.

In order to compare the two masks, we structure 500-nm-wide waveguides on two samples of TiO_2 (Fig. 2.6). For one mask, we deposit a layer of Cr using e-beam evaporation to act as an etch mask, whereas on the other we deposit Al_2O_3 using reactive sputtering. The samples are both successfully lifted off and processed in the RIE. Figure 2.6 also shows the samples after the dry etch but before the wet etch that removes the etch masks. The Cr mask outperforms the alumina mask in terms

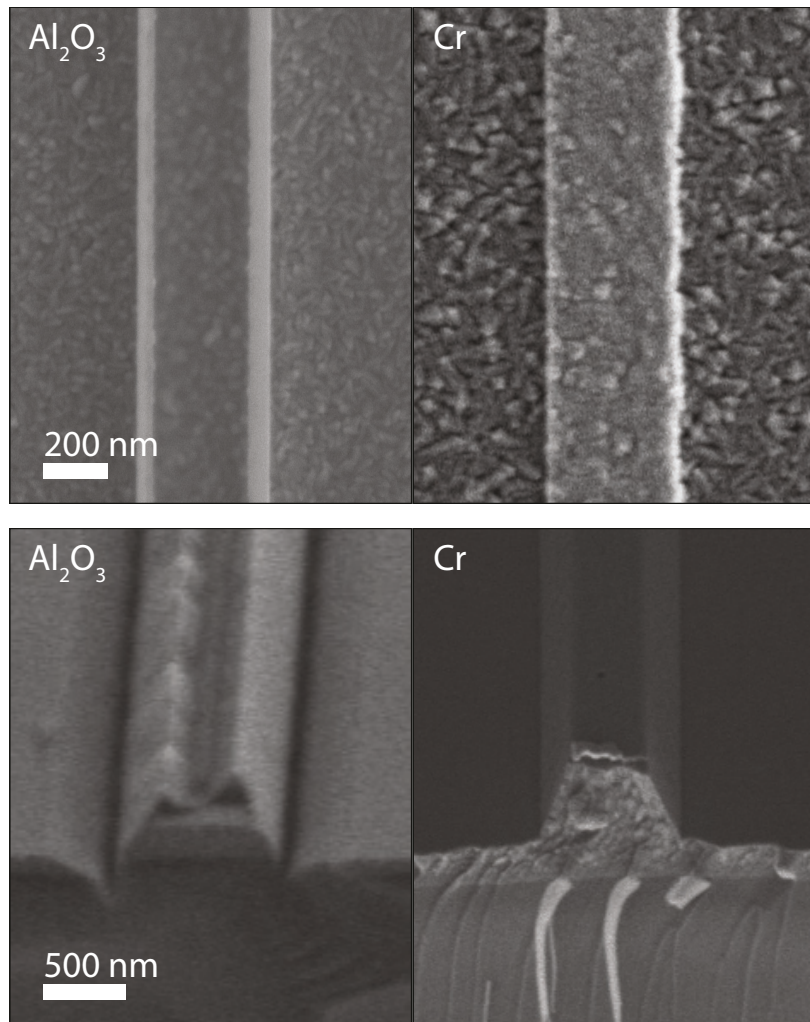


Figure 2.6: Comparison between etch masks. (Top) The sidewall is initially smoother using the Al_2O_3 mask when compared to the Cr mask. (Bottom) However, the etch selectivity is much better using the Cr mask.

of etch resistance to the fluorine. On the alumina mask, we see significant trenching, which is a signature of an overly physical etch [51, 52]. As both masks are etched on top of identical TiO_2 substrates, we hypothesize that the trenching is caused by redeposition of Al_2O_3 or AlF_x etch-product on to the waveguide sidewalls during the etch process. This trenching could perhaps be avoided with further optimization of the etch recipe.

2.4.2 Chromium deposition optimization

During the pattern transfer process, any features in the mask pattern are etched directly into the substrate underneath, and are exaggerated by the etching process. For this reason, it would be best to achieve as smooth an etch mask as possible. Unfortunately, a Cr film is formed of finite grains — ideally, we would design the metal-deposition process so that the grain size is minimized. In the following section, we deposit Cr at multiple deposition rates to obtain the best quality Cr film possible.

We use electron-beam evaporation to deposit 80 nm of Cr at deposition rates of 20, 10, 5 and 0.5 Å/s onto clean silicon samples. We control for all other conditions. All films are deposited at room temperature after 3 hours of pumping down the vacuum chamber. The deposition pressure was 8×10^{-7} Torr for all samples. After deposition, the chamber remained under vacuum for an additional 10 minutes in order to prevent additional oxidation of the Cr films.

We image the surfaces of the films using scanning electron microscopy (SEM) (Fig. 2.7). At lower magnification, the samples look very similar. At higher magnification, we see that Cr deposited at the higher rates is composed of longer filaments.

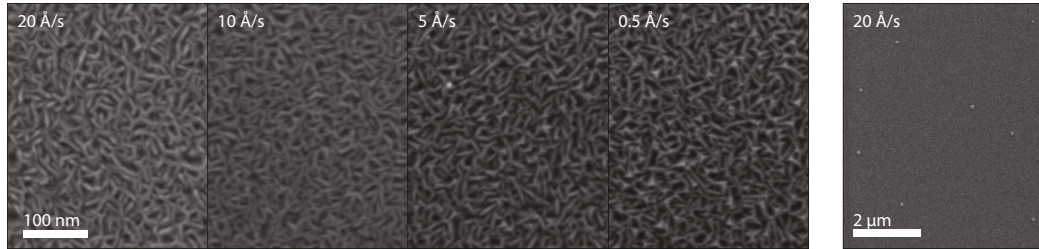


Figure 2.7: SEM comparing different deposition rates of Cr. At the highest rate (20 \AA/s), large particles are formed on the surface of the film.

At smaller rates, more pitting appears. At the very highest rate (20 \AA/s), very large particles appear. They do not appear for samples deposited at all the other rates.

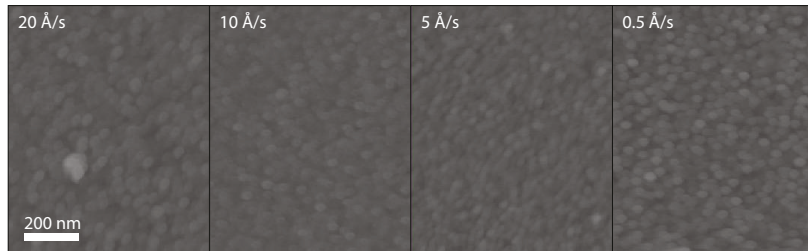


Figure 2.8: AFM comparing different deposition rates of Cr.

Using atomic force microscopy (AFM), we scan the surfaces of the different films (Fig. 2.8) and measure their respective surface roughnesses. We note that it was difficult to scan the 20 \AA/s sample because the particles would break the AFM tips, indicating that they are very large in size. We also measure the sheet resistivity using a 4-point probe station. The extracted values are summarized in Table 2.5.

In conclusion, we find that at the higher rates, unwanted large particles appear. At the lower rates, the surface seems to be rougher. Resistivity measurements show the lowest resistance for 5 \AA/s films, indicating the highest quality material. Ultimately, we select the deposition rate of 5 \AA/s , which yields a smoother, higher quality film than what had been used previously while avoiding the large particles.

Deposition rate ($\text{\AA}/\text{s}$)	RMS surface roughness (nm)	Sheet resistivity (Ω/sq)
20	0.72	0.377
10	0.66	0.359
5	0.77	0.293
0.5	1.09	0.329

Table 2.5: Surface roughnesses and sheet resistivities for the deposited Cr films.

2.4.3 Lift-off recipe

Because the Cr mask is formed of grains, it is challenging to lift the entire mask simultaneously in a single step. We find that the mask separates into particles and frequently redeposits onto the surface of the device layer. We have solved this problem by sonicating the mask during lift-off and by replacing the fluid intermittently. Though the act of sonication does directly break the mask up into particles, redeposition is ultimately avoided by replacing the solvent frequently. Through trial and error, we have developed a lift-off recipe with carefully designed steps that are long enough to release the pattern, but not too long to allow for any deposition or to damage the fine features in the mask (Table 2.6).

2.4.4 Treatment prior to metal mask removal

Following the dry etching step, the samples are processed in a wet etch in order to remove the remaining metal mask. Critically, the samples need to be put through another O_2 descum before this step. Otherwise, the etchant reacts with residual

Step	Solvent	Time (min:sec)
1	Remover PG	0:30
2	Remover PG	1:30
3	Remover PG	2:30
4	Acetone	0:30
5	IPA	0:30

Table 2.6: Metal lift-off procedure for Cr on TiO₂. The use of multiple steps is to avoid redeposition of the lifted off material. The sample should be sonicated at room temperature at the most gentle setting.

polymer particles that are created during etch procedure and creates particles that cannot be removed from the sample (Fig. 2.9). Following the descum, the samples are dipped in Cr etchant at room temperature with thorough agitation, followed by multiple rinses in distilled water.

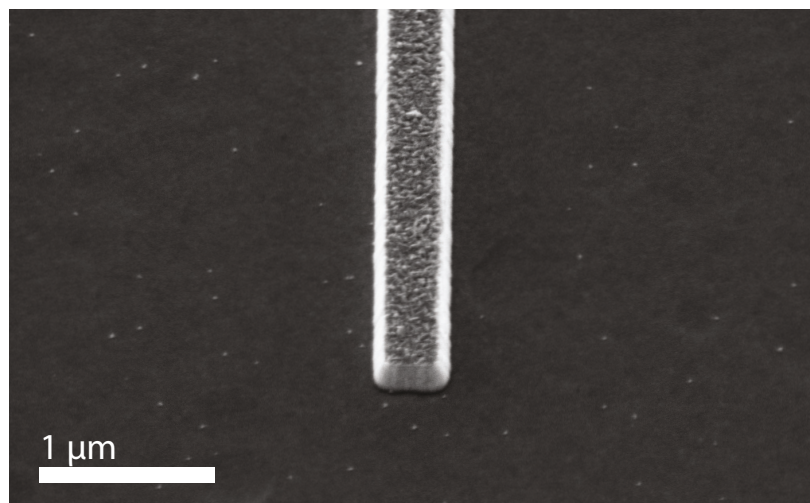


Figure 2.9: If a sample is not descummed before being placed in the Cr etchant, particles are formed that can ruin a sample.

Parameter	Bradley et al. [15]	This work
CF ₄ flow rate (sccm)	16	16
H ₂ flow rate (sccm)	4	4
Pressure (mT)	5	8.5
μW power (W)	300	230
RF power (W)	150	150

Table 2.7: Etch recipe for pattern transfer from Cr to TiO_2 .

2.5 Improvements to the etch procedure

2.5.1 Recipe optimization

There are a number of parameters that can be adjusted during an etch process, including the microwave power (μW) which ignites and sustains the plasma, the RF power which accelerates the ions onto the sample, the flow rates of individual gases and the chamber pressure setting. The recipe used by Bradley *et al.* is presented in Table. 2.7 alongside the recipe developed in this work.

Using Bradley's recipe, it is challenging for the chamber pressure to stabilize — the mass flow controller on the etcher often fluctuates its settings wildly for up to a minute before it settles and yields the desired chamber pressure. Once the power ignites the plasma, it takes an additional minute to settle, as well. This, in turn, often extinguishes the plasma mid-process, leaving the user to guess at how long to keep the sample in the etcher. By raising the desired chamber pressure from 5 mT to 8.5 mT, the desired pressure becomes easily achievable with the given flow rate, and

the pressure stabilizes almost immediately.

Next, we adjusted the input powers. By tuning these two values, we can control how physically- or chemically-active an etching process is. Ideally, the μW power should be as large as possible to generate as much plasma as possible and increase the etch rate. However, if the power is too high, it becomes more challenging to sustain the plasma, and the etch rate becomes unstable. In order to improve the stability of the plasma, we dropped the μW power from 300 W to 230 W. This is the highest power achievable that was found to maintain the plasma for several minutes without the plasma spontaneously extinguishing.

2.5.2 Etch rate estimation with AFM

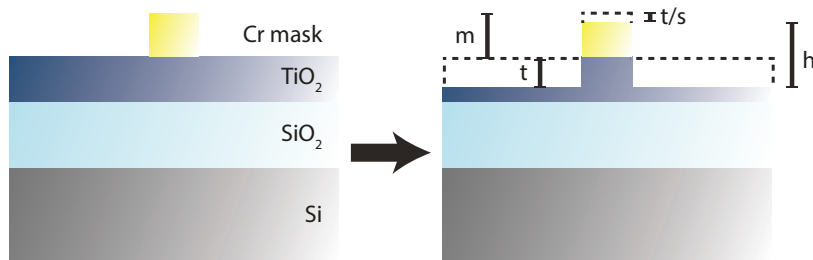


Figure 2.10: When placed in the etcher, the TiO_2 film etches faster than the Cr mask by a ratio of $s \approx 9$. The only height that can be measured using an AFM or a scanning profilometer is a sum of the remaining mask height ($m - t/s$) and the height that is etched t .

With the updated recipe, the plasma is now stable during the entire etch process. However, the etch rate can still vary between each use because of factors beyond the user's control, such as the condition of the chamber. We would like the ability to consistently etch away a very specific thickness. To do so, we need a way to monitor the amount of material that has been etched away during the process. The only

accurate and quantitative measurement we can make at this scale is to use an atomic-force microscope (AFM) to measure the height of the device features. The height h that is retrieved consists of both the height of the device and the remaining mask that has yet to be etched away. The final height is related to the etched thickness t , the measured mask thickness m , and the selectivity s by

$$h = t + (m - t/s). \quad (2.1)$$

Despite the inconsistency in the etch rate, we have found that the selectivity between Cr and TiO_2 remains around 9 quite reliably. We can measure the height of a test region on the sample using an AFM before and after an etch and use Eq. 2.1 to obtain the thickness t that was etched. We use this value to estimate what the etch rate is during any individual step, and estimate the remaining time necessary to achieve our desired thickness. In order to etch away the entire device layer, (*i.e.*, to completely remove the TiO_2 slab surrounding the waveguides) we obtain a final target height from Eq. 2.1 by replacing t with the total film thickness, a value that is easily obtained using ellipsometry.

2.6 Cleaving the sample

The final step in the fabrication process involves cleaving the edges of the samples in order to expose an open waveguide through which we can couple in light. This step needs to be done carefully, and because it is done manually, unfortunately it carries an element of luck and randomness to it. Through trial and error, we have developed a method which has a large yield and produces smooth facets that minimize scattering

and can yield insertion losses as low as several dB/facet [53].

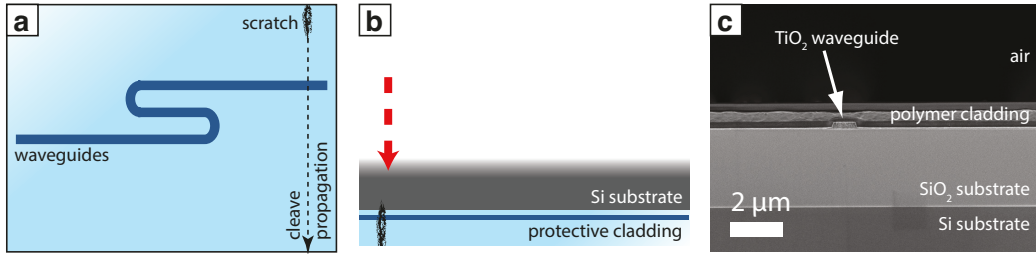


Figure 2.11: Cleaving a sample. **a)** Top-down view of the sample, indicating the location to scratch. **b)** Side-view of the sample, face-down after being scratched. The red arrow shows where to press on the chip in order to initiate the cleave propagation. **c)** A cross-section SEM of a cladded anatase TiO_2 waveguide cleaved using the described method. This facet was not polished before imaging.

The sample must first be cladded with a protective layer. If the device did not already necessitate a cladding, a thick layer of resist can be deposited (*e.g.*, 2.6 μm of Shipley S1822 resist). We locate the end of the waveguides by eye and use a diamond scribe to mark the cleave location in the edge of the chip (Fig. 2.11). The scratch must be deep enough to penetrate through the cladding and the device layer in order to reach the silicon substrate. The device is then placed face-down onto a dry, clean and powder-free wipe. Next, we apply some gentle pressure on the edge of the chip above the location of the scratch. This is done with the butt end of a pair of tweezers. It is important to apply this pressure using a blunt tool with a large area so that the cleave can begin propagating at the location marked using the diamond scribe in the previous step. Using a sharp object instead can initiate cleavage propagation along a different crystal plane. The edge facets are then optionally mechanically polished to obtain an even smoother face. If a protective layer of resist is deposited on the sample, this layer can be removed in a quick solvent rinse.

2.7 Conclusion

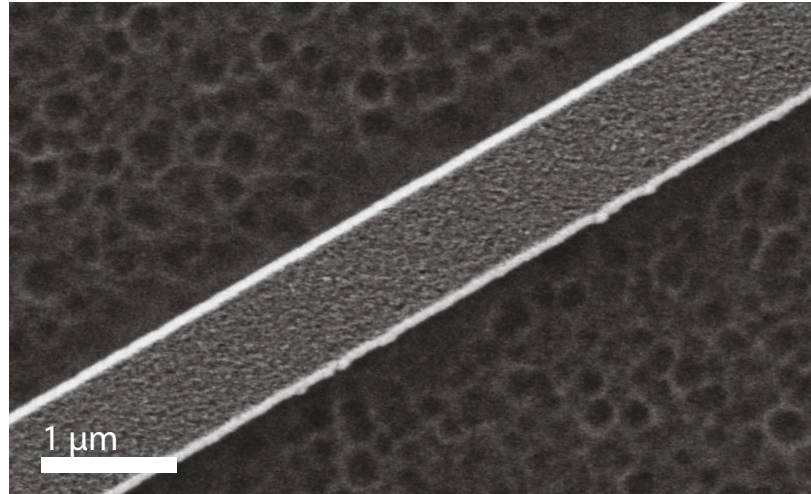


Figure 2.12: An anatase TiO_2 waveguide fabricated using the above parameters.

The development of these more sophisticated procedures have produced higher quality devices (Fig. 2.12). By reducing the number of over-etched samples and devices lost to failed cleaves, they have greatly increased the fabrication yield from below 25% to well above 75%. As will be discussed in Chapter 3, these procedures have succeeded in lowering waveguide propagation losses in anatase TiO_2 to the intrinsic propagation loss of the film, around 4 dB/cm at $\lambda = 1550$ nm [53].

Chapter 3

Anatase ring resonators with negative thermo-optic coefficient

We fabricate polycrystalline anatase TiO_2 micro-ring resonators with loaded quality factors as high as 25,000 and average losses of 0.58 dB/mm in the telecommunications band. Additionally, we measure a negative thermo-optic coefficient dn/dT of $-4.9 \pm 0.5 \times 10^{-5} \text{ K}^{-1}$. The presented fabrication uses CMOS-compatible lithographic techniques that take advantage of substrate-independent, non-epitaxial growth. These properties make polycrystalline anatase a promising candidate for the implementation of athermal, vertically-integrated, CMOS-compatible nanophotonic devices for nonlinear applications.

3.1 Introduction

Titanium dioxide (TiO_2) is a promising nanophotonic material due to its high transparency in the visible [15, 38, 54–59] and its applications for integrated nonlinear optics [17, 45, 60, 61]. Its multiple phases (rutile, anatase and brookite) each possess a large bandgap greater than 3 eV [14], yielding high transparency for wavelengths $\lambda \geq 400$ nm spanning the visible and telecommunication bands. Unlike other high-index photonic platforms such as silicon or chalcogenide glasses, TiO_2 photonic circuits can operate with virtually no two-photon absorption for $\lambda \geq 800$ nm and without three-photon absorption over the entire telecom band [17]. TiO_2 has a linear index above $n = 2.4$ in the optical regime and a nonlinear index approximately 30 times that of silica, making it favorable to transparent materials such as Al_2O_3 , SiO_2 , SiN_x or diamond for nonlinear applications. TiO_2 has the potential to achieve larger effective nonlinearities than these alternative materials [61]. These properties make TiO_2 an interesting platform for nonlinear optics research in the near infrared.

Recently, TiO_2 has attracted attention for its use in athermal (*i.e.*, temperature insensitive) photonic devices, particularly for applications that are wavelength sensitive [18, 19, 56, 62–65]. Athermal operation can be achieved using the material's negative thermo-optic coefficient (TOC, dn/dT , where n is the refractive index and T is the temperature) when paired with a positive TOC material. For example, ring resonators fabricated from silicon (*i.e.*, a materials with a positive TOC) have been clad with amorphous TiO_2 in order to obtain an effective TOC near zero for over 30 °C at 1.3 and 1.55 μm [19, 56, 64, 66]. Although this effect has also been achieved using polymers [67], which are widely known to possess negative TOCs [20], anatase TiO_2

has the benefit of being able to withstand modest temperatures, making it CMOS-compatible. Anatase TiO₂ can therefore be used in vertical integration schemes, drastically increasing device density on a chip [68].

In this chapter we demonstrate the first anatase TiO₂ micro-ring resonators and use them to evaluate the quality of our fabrication process and to confirm the expected negative TOC of anatase. While the TOC of other phases of TiO₂ have been reported [18, 19, 65], the TOC of the anatase phase has not been studied in the telecommunications band. So far, anatase is unique in that it is the only phase of TiO₂ in which nonlinear processes such as spectral broadening [61] and third-harmonic generation [45] have been reported in a photonic integrated circuit. In contrast, these observations have remained elusive in rutile and amorphous TiO₂ due to their challenging fabrication and photochromism, respectively [58, 69, 70]. Finally, polycrystalline anatase TiO₂ can be deposited at low temperatures (*e.g.*, 600 K) on amorphous substrates, ensuring compatibility with a variety of CMOS processes.

3.2 Theory

3.2.1 Transmission characteristics of a micro-ring resonator

The spectral dependence of the transmission of a ring resonator with an input port and no add or through port has been thoroughly characterized and can be derived analytically using the scattering matrix approach [71–73]:

$$T = \left| \frac{t - \alpha e^{i\phi}}{1 - \alpha t e^{i\phi}} \right|^2, \quad (3.1)$$

where t is the transmission (or self-coupling) coefficient corresponding to the fraction of the field that does not couple into the ring after a single pass, α is the total relative field that is not lost in a round trip and ϕ is the round trip phase shift. ϕ varies as a function of wavelength λ , effective index n_{eff} , and propagation length L :

$$\phi = 2\pi \frac{n_{\text{eff}}}{\lambda} L. \quad (3.2)$$

The transmission curve has characteristic resonance peaks at the points where the numerator of Eq. 3.1 goes to zero. Additionally, significantly strong reflections at the facets create simultaneous counter-propagation within the ring that yields asymmetric resonances [74, 75]. Using the scattering matrix approach [72], we derive the asymmetric transmission for this type of device to be

$$T = \left| \frac{(1 - \alpha t e^{i\phi})(t - \alpha e^{i\phi})}{\gamma e^{i\varphi}(t - \alpha e^{i\phi})^2 - (1 - \alpha t e^{i\phi})^2} \right|^2, \quad (3.3)$$

where the additional coefficients φ and γ determine the shape and magnitude of the asymmetry. The variables φ and γ correspond, respectively, to the phase difference between the two counter-propagating waves and the losses resulting from both propagation through the waveguide and transmission through the facets at the ends. By fitting Eq. 3.3 to a particular resonance, we can extract α and use it to compute a propagation loss α_z for the waveguide that makes up the ring resonator. For a critically-coupled resonator ($\alpha = t$), the propagation loss can also be estimated using the group index n_g and the loaded Q to be [68]

$$\alpha_z = \frac{\pi n_g}{Q \lambda_0}. \quad (3.4)$$

These equations provide a method for accurately characterizing fabricated ring resonators, and extracting propagation losses.

3.2.2 Effective thermo-optic coefficients

Heating the sample induces a temperature-dependent refractive index change in the constituent materials, which can be characterized very precisely using a resonator. In a cavity structure such as a ring resonator, changing the temperature tunes the resonant wavelength λ_0 by changing the index of the resonator material and via thermal expansion of the substrate. We quantify this change using [67, 76]

$$\frac{d\lambda_0}{dT} = \left(\frac{dn_{\text{eff}}}{dT} + n_{\text{eff}}\alpha_{\text{Si}} \right) \frac{\lambda_0}{n_g}. \quad (3.5)$$

Eq. 3.5 includes a term for the thermal expansion coefficient of silicon ($\alpha_{\text{Si}} = 2.59 \times 10^{-6} \text{ K}^{-1}$) [77]. Due to the geometry, the silicon substrate dominates the mechanical properties and thermal expansion of the sample. This new term represents the primary effect of thermal expansion on our device, which is to increase the diameter of the rings and shift the resonances towards longer wavelengths. Because the change in waveguide cross-section due to thermal expansion is negligible, the group index does not change significantly to a first approximation.

We use the measured value of $d\lambda_0/dT$ to estimate the change in index of the component materials. A waveguide that consists of a substrate, a core material, and an over-cladding material has an effective index n_{eff} that we approximate by

$$n_{\text{eff}} \approx \Gamma_s n_s + \Gamma_c n_c + \Gamma_o n_o, \quad (3.6)$$

where Γ represents the power confinement factor within the individual materials and the subscripts s, c, and o stand for substrate, core, and over-cladding materials, respectively. This equation yields a very good first approximation for dn_{eff}/dT by

differentiating [63]:

$$\frac{dn_{\text{eff}}}{dT} \approx \Gamma_s \frac{dn_s}{dT} + \Gamma_c \frac{dn_c}{dT} + \Gamma_o \frac{dn_o}{dT}. \quad (3.7)$$

For small changes in material index, we assume that the power confinement factors remain constant. Given measured TOCs of the cladding materials, we use Eq. 3.7 with Eq. 3.5 to estimate the thermo-optic coefficient of the core material.

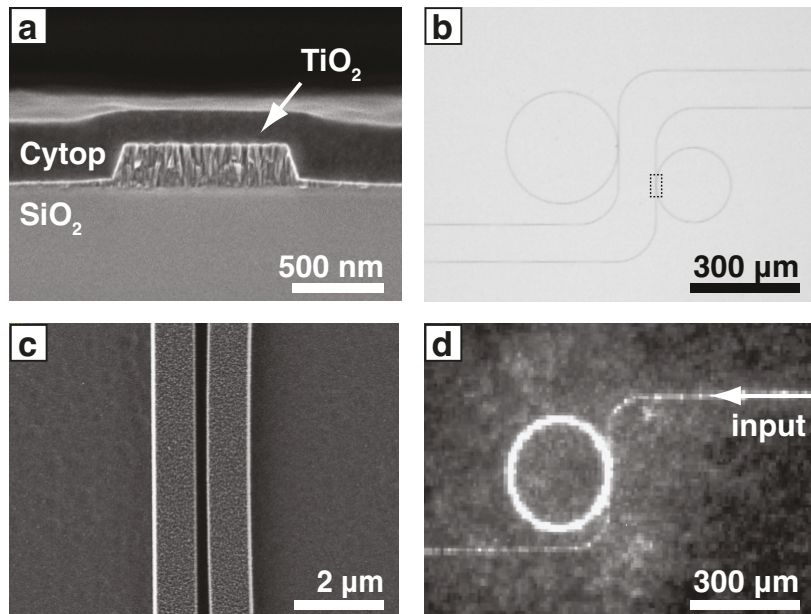


Figure 3.1: **a)** Cross-section of the TiO_2 waveguide, showing the embedded polycrystalline grains. The device is composed of a TiO_2 waveguide on a thermal oxide substrate and cladded by a CYTOP polymer. The sidewalls are sloped at 75° . **b)** Microscope image of a pair of anatase micro-ring resonators with coupling bus waveguides. **c)** Scanning electron microscope image of the coupling region indicated in (b), showing the polycrystalline grains on the surface and a 250-nm gap. **d)** A 300- μm diameter anatase micro-ring operating near $\lambda = 1550$ nm.

3.3 Experimental

3.3.1 Fabrication

We fabricate devices using methods described by Bradley et al [15]. We structure waveguides from a 250-nm thick polycrystalline anatase film that is deposited using RF magnetron sputtering at 600 K on an oxidized silicon substrate. The waveguides are defined by electron beam lithography and reactive ion etching, leaving our final desired structures on the silica substrate. The final fabricated chip is top-cladded with a low-index ($n = 1.33$ at $\lambda = 1550$ nm) transparent polymer (CYTOP) to further reduce losses and protect the devices (Fig. 3.1a). The ends of the chip are cleaved to prepare end facets.

The waveguides are designed to support a single mode throughout the wavelengths of operation (1525 – 1575 nm). The waveguides are trapezoidal in shape, with a width of 900 nm on top, 1035 nm at the base, and a sloped sidewall of approximately 75° due to the etch chemistry and substrate power (Fig. 3.1a). This structure supports hybrid modes with $< 1\%$ polarization mixing; therefore we treat them as pure modes (Fig. 3.2a). The ring resonators are coupled via a single 6.4-mm-long bus waveguide and have ring-waveguide coupling-gaps of 250, 300, and 350 nm, and ring diameters of 200 and 300 μm (Fig. 3.1b-c). These dimensions are designed to ensure a free spectral range larger than 1.2 nm (150 GHz) and to achieve near critical-coupling within the wavelengths of operation.

3.3.2 Measurement setup

We couple in and out of the waveguides using a pair of 0.85-NA objectives on 3-axis stages. We launch 1525 – 1575 nm light using a tunable laser source with an input power of 4.1 mW and a resolution of 5 pm (Fig. 3.1d). We select only transverse magnetic-(TM-)polarized light (*i.e.*, electric field polarized perpendicular to the plane of the device). We use a pellicle beam splitter before the devices and a pair of InGaAs photodiode detectors to measure the output power and the input power simultaneously to normalize the total transmission.

To measure the thermo-optic coefficient, the fabricated chip is placed on a conductive aluminum slab mounted on a heater. The light is coupled in and out of the waveguides using a tapered lensed fiber with a 2.5- μm spot size on the input and a microscope objective on the output facet. The objective directs the output light onto either an IR camera used for alignment or an InGaAs detector used for taking data. A polarizer located between the objective and the detector allows us to determine the input and output polarizations of light. We excite the TM-mode and measure the spectrum of several high- Q resonances at multiple temperatures from 24 – 37 °C.

3.4 Results

We couple into and out of the TiO₂ bus waveguides, yielding total insertion losses off-resonance as low as 10 dB for the propagation of the TM-polarized mode. Fig. 3.2b shows a typical transmission spectrum for a ring with a diameter of 300 μm and coupling gap of 300 nm. It shows distinct, equally spaced resonances that deepen

for longer wavelengths with extinction ratios ranging from 2.3 to 10.5 dB, achieving near-critical coupling at the longest wavelengths. Some of the resonances show an asymmetry. This asymmetry is independent of wavelength sweep direction or input power. The measured free spectral range (FSR) for the 200- and 300- μm diameter rings is 236 and 157 GHz, respectively. We compare these values to theoretical values computed using $\text{FSR} = c/(n_g L)$ using a simulated group index of $n_g = 2.03$. We calculate the FSR of the 200- and 300- μm diameter rings to be 235 and 157 GHz, respectively (Table 3.1).

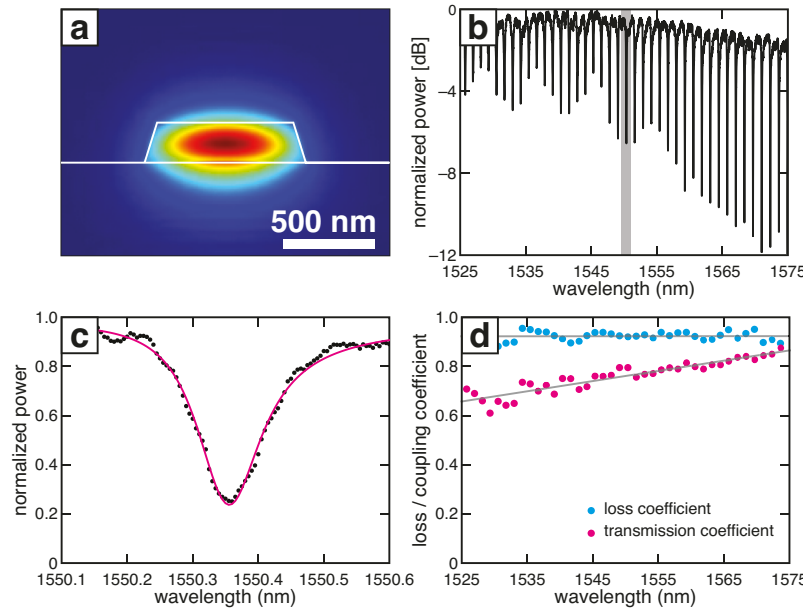


Figure 3.2: **a)** Energy density for TM-polarized guided mode at $\lambda = 1550 \text{ nm}$. **b)** Transmission spectrum of a 300- μm diameter, 300-nm gap anatase ring resonator. The resonances get deeper for longer wavelengths, with a loaded quality factor as high as 2.0×10^4 at $\lambda = 1571 \text{ nm}$. **c)** A fit to an asymmetric resonance at $\lambda = 1550 \text{ nm}$ indicated in gray in (b). This fit yields a transmission coefficient t of 0.798 and a loss coefficient α of 0.911, corresponding to a propagation loss of 0.77 dB/mm. **d)** Extracted transmission coefficients t and loss coefficients α for each resonance. The linear fits are a guide to the eye, showing that α remains constant, indicating that the propagation loss does not change significantly over this wavelength range.

For the 200- μm diameter rings, we obtain Q -factors of 10^3 with a maximum observed loaded Q -factor of 5.5×10^3 with a gap of 250 nm. For the 300- μm diameter rings, we obtain Q -factors of 10^4 with a maximum observed loaded Q -factor of 2.5×10^4 with a gap of 250 nm.

We fit the transmission spectra for asymmetric resonances from $\lambda = 1525$ to 1575 nm to Eq. 3.3 (Fig. 3.2c) and extract the transmission coefficient t and the loss coefficient α (Fig. 3.2d). We note that the loss coefficients are smaller for the larger ring diameter. The transmission coefficient is larger for the larger ring diameter as well. We calculate the corresponding power propagation losses for the fundamental TM-polarized mode directly from α using $\alpha^2 = e^{-\alpha_z 2\pi R}$. We average the propagation losses extracted from $\lambda = 1545$ to 1555 nm and tabulate them in Table 3.1. Taking the geometric mean of the values in Table 3.1 yields an average propagation loss of 2.48 dB/mm for the 200- μm rings, with a lower average loss of 0.58 dB/mm for the 300- μm rings. The lowest propagation loss obtained is 0.40 dB/mm found for a 300- μm ring.

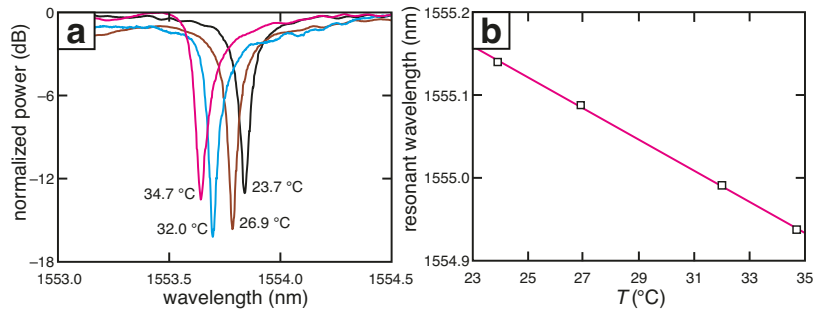


Figure 3.3: **a)** Raising the temperature blueshifts the resonance, corresponding to a negative TOC. **b)** Fitting to the positions of the resonance peaks as a function of temperature yields a rate of $d\lambda_0/dT = -19 \text{ pm/K}$, corresponding to a dn_{TiO_2}/dT of $-4.9 \pm 0.5 \times 10^{-5} \text{ K}^{-1}$. The height of the box symbol represents the error in the fit to the curves in (a).

Table 3.1: Free spectral range and propagation losses near $\lambda = 1550$ nm for different devices and coupling gaps. The propagation losses are calculated directly from α .

Ring diameter	Gap size	Theoretical FSR	Measured FSR	Propagation loss
[μm]	[nm]	[GHz]	[GHz]	α_z [dB/mm]
200	250	235	235	1.90
200	300	235	235	2.58
200	350	235	238	3.10
300	250	157	156	0.40
300	300	157	157	0.69
300	350	157	158	0.72

We vary the temperature and we probe a 300-μm-diameter ring with a gap of 300 nm around $\lambda = 1555$ nm. We observe that the location, symmetry, and depth of one of the sharper resonances in the spectrum change as a function of temperature (Fig. 3.3a). At higher temperatures, the location of the resonance blueshifts at a rate of $d\lambda_0/dT = -19$ pm/K (Fig. 3.3b), corresponding to a change in effective index of $dn_{\text{eff}}/dT = -2.86 \times 10^{-5} \text{ K}^{-1}$.

The TOC of the anatase thin film is difficult to measure directly as it is deposited on a thick oxide substrate. The thickness of the substrate creates many fringes in the ellipsometric profile, making it difficult to obtain an accurate fit for the optical constants. To determine the contribution of each layer to the measured dn_{eff}/dT of the device, we simulate the power confinement factors for the three regions using a commercial finite-element eigenmode solver, setting both the substrate and over-

cladding thickness to 3 μm (Table 3.2). Changing the cladding index from 1.33 to 1.45 has a minimal effect on the core confinement of the mode. The errors in the power factors are estimated using the errors in the measurement for the material parameters, the measurement error for the waveguide geometry (determined using SEM and AFM) and the finite mesh used in the solver. We measure dn/dT for SiO_2 and CYTOP thin films directly using temperature-controlled ellipsometry (Table 3.2). Inserting these values into Eq. 3.7 yields a TOC for TiO_2 of $dn_{\text{TiO}_2}/dT = -4.9 \pm 0.5 \times 10^{-5} \text{ K}^{-1}$.

Table 3.2: Simulated power confinement factors for a $900 \times 250 \text{ nm}$ TiO_2 waveguide. The TOC for SiO_2 and CYTOP were measured on thin films using temperature-controlled ellipsometry. The TOC for TiO_2 was calculated using Eq. 3.7.

Region	Material	Confinement		TOC $dn/dT [\text{K}^{-1}]$
		factor Γ		
Cladding	CYTOP	$24.2 \pm 0.4\%$	$-9.7 \pm 0.2 \times 10^{-5}$	
Core	TiO_2	$29.4 \pm 1.6\%$	$-4.9 \pm 0.5 \times 10^{-5}$	
Substrate	SiO_2	$46.4 \pm 1.4\%$	$2.0 \pm 0.2 \times 10^{-5}$	

3.5 Discussion and conclusion

To quantify the accuracy of our fabrication and measurement process, we compare our measured FSRs to simulation results. The measured FSRs increase as the ring circumferences decrease and agree with theoretical values within 0.5%. Additionally, these results, as well as the lack of additional resonances, confirm that we are exciting only TM-polarized modes within the resonators. TE-polarized modes yield drastically

smaller FSRs of 127 and 190 GHz for the 300 and 200- μm diameter rings, respectively, because their group index is comparatively larger (*e.g.*, $n_g = 2.51$ for TE *vs.* $n_g = 2.03$ for TM) than for a TM-polarized mode. This agreement affirms the robustness of our simulations, material parameters, and tight fabrication tolerance.

We can verify the fits to Eq. 3.3 by reviewing the extracted coefficients in Fig. 3.2d. First, we observe little variation in α , as expected from Rayleigh scattering within this wavelength range. Conversely, t changes with wavelength. A constant coefficient is observed in all of the measured devices, and it is how we unambiguously distinguish α from t [73].

These fits also yield coefficients from which we can estimate the propagation loss within the rings. The mean propagation loss for the larger rings is 0.58 dB/mm at $\lambda = 1550$ nm. This value is comparable to the propagation losses that have been previously cited for polycrystalline anatase (0.4 – 0.8 dB/mm) [15, 61]. Additionally, it is calculated based on the more accurate resonator-based method than the top-down imaging-based loss extraction method used previously. A loss of 0.58 dB/mm compares favorably to early results using polycrystalline silicon, another material which is expected to exhibit similar scattering losses and has reported propagation losses as low as 0.9 dB/mm for films of a similar thickness [78]. The grains in these polycrystalline films, which contribute to the surface roughness and thus the scattering loss [15, 68], are on the order of 50 nm, less than $\lambda/30$. Prism coupling measurements for TM-polarized light at $\lambda = 1550$ nm in the thin films fabricated for this work yield losses of 0.33 dB/mm. Our lowest device losses (0.40 dB/mm) are similar to these planar-waveguide measurements, indicating that the film itself is a limiting source of

loss in our devices.

The propagation losses take into account both bending losses and scattering losses due to the polycrystalline structure and fabrication imperfections. The measured propagation loss in the rings increases by a factor of 4 when decreasing the bend radius from 300 to 200 μm ($0.58 \text{ vs. } 2.48 \text{ dB/mm}$). A larger propagation loss implies that bending losses have become significant. However, finite element simulations predict no large bending loss associated with a 100- μm bend radius. Alternatively, since a guided mode is pushed towards the outer wall in a ring with sharper bends, larger losses imply that the sidewalls of the waveguide have an increased roughness due to the fabrication process. Thus, we conclude that fabrication imperfections are the dominant contribution to the propagation losses in this context. This also explains why devices performed better under TM excitation when compared to TE excitation: the TE mode suffers from higher losses due to stronger localization of the fields near the rough fabrication boundaries. Our fabrication methods can be further optimized to minimize propagation losses by adopting a more optimal etch chemistry [79] or by using resist reflow techniques [43].

Minimum total insertion losses of 10 dB with a minimum waveguide propagation loss of 0.40 dB/mm are realistic values for our devices. Given a 6.4-mm-long waveguide, we calculate a waveguide loss of 2.4 dB giving an insertion loss of 3.7 dB/facet. Finite element simulations yield a power overlap of 66.0% between the fundamental TM mode and a focused Gaussian beam spot using a numerical aperture of 0.85. This accounts for 1.8 dB of the insertion loss per facet, with the remaining 1.9 dB/facet arising due to scattering created during facet cleavage. The insertion loss could be

lowered by mechanically polishing the waveguide facets.

Using the extracted losses above and Eq. 3.4, we estimate that the largest intrinsic quality factor Q_0 for these rings is 89,000, corresponding to a theoretical maximum loaded Q of 44,500. However, the maximum observed loaded Q of 25,000 does not reach this limit. We attribute this discrepancy to the fact that the resonators are operating in the over-coupled regime, which is confirmed by the fact that t is less than α (Fig. 3.2d), as more light is lost to coupling than to propagation around the ring. The estimated Q_0 still compares favorably to early results using polycrystalline silicon of 40,000 [68]. However, it remains an order of magnitude smaller than the highest reported Q -factors achieved in sol-gel-based amorphous TiO₂ whispering gallery micro-cavities [57] and lifted-off amorphous TiO₂ ring resonators [45]. Q -factors on the order of 10^4 are large enough to observe some nonlinear processes, such as low-threshold harmonic generation, but improvements are necessary to demonstrate on-chip frequency combs or nonlinear interferometers, which typically require loaded quality factors greater than 10^5 [80, 81].

The blueshifting of the resonance as a function of temperature depicted in Fig. 3.3 is consistent with a negative TOC, as has been reported previously for TiO₂. This shift cannot be attributed only to the change in the resonator geometry caused by thermal expansion because that would contribute solely to a redshift, displacing resonances towards longer wavelengths. We attribute the change in the depth of the resonances to a changing asymmetric phase term φ , corresponding to the round-trip phase in the bus waveguide. This term also changes as a function of effective index. Because we normalize the measured intensity to its maximum value, different

asymmetries appear to produce different extinction values.

Our measured value of $dn_{\text{TiO}_2}/dT = -4.9 \pm 0.5 \times 10^{-5} \text{ K}^{-1}$ is within an order of magnitude of prior literature values for the TOC of amorphous TiO_2 (-1 to $-2 \times 10^{-4} \text{ K}^{-1}$) [19, 57]. A more extensive study that varies the waveguides geometry and that probes a larger temperature range would be beneficial to further understand and optimize athermal anatase devices. This TOC enables athermal device designs that consist solely of TiO_2 waveguides on a substrate, without the need for a negative TOC cladding. A standard oxide cladding, such as SiO_2 , can provide the balancing positive TOC. Using a finite element eigenmode solver and the TOC values reported above, we predict athermal operation dimensions for a TiO_2 ring resonator cladded in SiO_2 on a silicon substrate at $\lambda = 1550 \text{ nm}$. For TE polarization, the waveguide cross-sectional dimensions are 390-nm wide \times 250-nm thick, while for TM polarization, the dimensions are 479-nm wide \times 300-nm thick. These designs can form the basis for vertically-integrated athermal photonic devices relying on a robust oxide material platform with high core-cladding index contrast.

In conclusion, we have fabricated and characterized high- Q polycrystalline anatase TiO_2 micro-ring resonators. The material platform and fabrication techniques are scalable, CMOS compatible, do not require specialized substrates, and support vertically integrated photonic devices. Using these methods, we have obtained intrinsic Q -factors of up to 89,000, corresponding to losses as low as 0.40 dB/mm at $\lambda = 1550 \text{ nm}$. We report the first measurement of a negative TOC in anatase TiO_2 at telecommunication wavelengths, which can be used in conjunction with CMOS-compatible positive TOC materials to fabricate vertically-integrated athermal optical devices. Given

these properties, anatase TiO_2 is well-positioned to become an important material for wavelength-insensitive, device-dense integrated nanophotonics.

Chapter 4

Asymmetric resonances in micro-ring resonators

Propagation losses in micro-ring resonator waveguides can be determined from the shape of individual resonances in their transmission spectrum. The losses are typically extracted by fitting these resonances to an idealized model that is derived using scattering theory. Reflections caused by waveguide boundaries or stitching errors, however, cause the resonances to become asymmetric, resulting in poor fits and unreliable propagation loss coefficients. In this chapter, we derive a model that takes reflections into account and, by performing full-wave simulations, we show that this model accurately describes the asymmetric resonances that result from purely linear effects, yielding accurate propagation loss coefficients. This work will enable more accurate fabrication characterization for integrated platforms.

4.1 Introduction

Ring resonators are one of the simplest and most commonly used components in photonic integrated circuits. Their high quality factors and ease of fabrication in any photonic platform make them useful for applications in wavelength-selective filters and multiplexers [82,83], optical delay lines [84], switches and modulators [85,86], and in other nonlinear applications enabled by the resonantly-enhanced intensity build-up [7,36,80,87–89]. Additionally, due to their simple analytic transfer function, ring resonators are also used for fabrication characterization; the individual resonances in the transmission spectrum of a ring can be measured and fit to extract propagation losses [53,73].

This fitting method has been shown to yield accurate propagation losses for ideal devices [73]. However, fitting experimental resonances to the transfer function often does not capture all of the physics properly and thus yields poor fits. Doing so generates unreliable values for propagation losses, making it more difficult to assess fabrication quality.

Back-reflections, which are common in realistic devices, can cause the resonances to exhibit asymmetries that are linear in origin [38,53,74,75,90]. These asymmetries are strictly unrelated to asymmetries caused by nonlinear interactions, such as by optical bistability [91–93]. For example, fabrication defects in the waveguide leading to and from the resonator can cause partial reflections that yield asymmetric Fano-like resonances in the otherwise symmetric spectrum of a ring resonator [38,53,74,86]. These asymmetries are most prevalent in smaller, low-loss systems with high quality factors, and pose an increasing challenge as fabrication quality further improves.

In this chapter, we generalize the familiar transfer function for micro-ring resonators to develop a model that includes the interference caused by accidental reflections in waveguides. Using full-wave simulations we demonstrate that these asymmetries are caused by reflections and are independent of input power. We also discuss situations in which reflections become significant. We use this generalized transfer function to extract the propagation loss of the simulated devices, and demonstrate that the model remains reliable in the presence of strong reflections, unlike the standard symmetric model. This generalized transfer function is important in the experimental characterization of micro-ring resonators with inherent reflections.

4.2 Theory

4.2.1 Standard symmetric transfer function

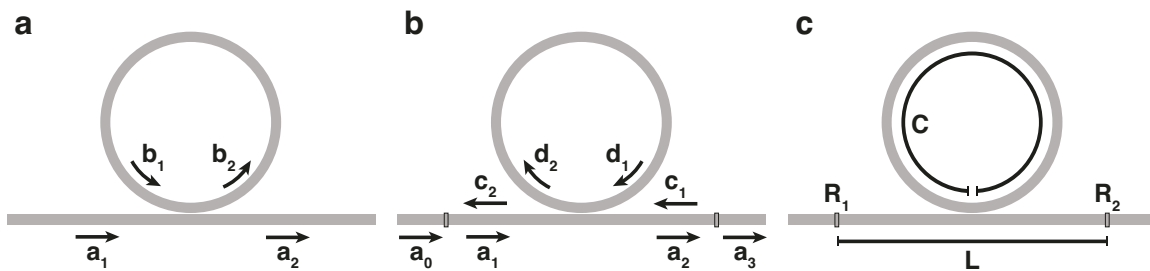


Figure 4.1: **a)** The right-traveling field in the waveguide excites a counter-clockwise-propagating mode b_2 and another right-traveling mode a_2 . These two modes interfere destructively when operating on resonance. **b)** Partial reflectors at the input and output of the waveguide enable left-traveling fields and clockwise-propagating modes. These fields form a secondary resonance (*i.e.*, $a_1 \rightarrow a_2 \rightarrow c_1 \rightarrow c_2 \rightarrow a_1$) that interferes with the whispering gallery modes in the ring to produce asymmetries in the combined spectrum. **c)** The simulated device: a ring resonator of circumference C coupled to a bus waveguide of length L between a pair of reflectors R_1 and R_2 .

The transmission of a micro-ring resonator coupled to a single waveguide (*i.e.*, an input port and no add or through port) has been well characterized and can be derived using scattering theory [71–73, 93, 94]. We begin by describing the set of interactions that yield the standard symmetric transfer function. The complete set of electric fields is illustrated in Fig. 4.1. The input and output fields are denoted by a_1 and a_2 , respectively. The input field a_1 is incident on a directional coupler which excites a counter-clockwise-propagating mode b_2 :

$$b_2 = \sqrt{1 - t^2} a_1, \quad (4.1)$$

where t is the transmission (or self-coupling) coefficient that corresponds to the field that remains in the waveguide after traversing the coupling region.

While propagating through the circumference C of the ring, the field b_2 accumulates a phase $\phi = \omega C / c = 2\pi n_{\text{eff}} C / \lambda$ and experiences a propagation loss α_z due to scattering and fabrication imperfections, yielding a field b_1 :

$$b_1 = e^{-\alpha_z C/2} e^{i\phi} b_2. \quad (4.2)$$

The total propagation loss in the ring is denoted by α :

$$\alpha^2 \equiv e^{-\alpha_z C}, \quad (4.3)$$

so that $\alpha \rightarrow 1$ in the lossless case and $\alpha \rightarrow 0$ as the propagation loss approaches infinity.

Part of the field b_1 couples back into b_2 . Adding this contribution to Eq. 4.1, we obtain

$$\begin{aligned} b_2 &= \sqrt{1 - t^2} a_1 + t b_1 \\ &= \sqrt{1 - t^2} a_1 + t \alpha e^{i\phi} b_2. \end{aligned} \quad (4.4)$$

The total output field a_2 is the sum of the field that is directly transmitted from a_1 through the coupler and the field that couples back from the ring from b_1 :

$$\begin{aligned} a_2 &= ta_1 + \sqrt{1-t^2}b_1 \\ &= ta_1 + \sqrt{1-t^2}\alpha e^{i\phi}b_2. \end{aligned} \quad (4.5)$$

The transmission for the ring resonator $T_{RR}(\phi)$ is the solution of the coupled Eqs. 4.4–4.5:

$$\begin{aligned} T_{RR}(\phi) &\equiv \left| \frac{a_2}{a_1} \right|^2 \\ &= \left| \frac{t - \alpha e^{i\phi}}{1 - \alpha t e^{i\phi}} \right|^2 \\ &= \frac{t^2 + \alpha^2 - 2\alpha t \cos \phi}{1 + \alpha^2 t^2 - 2\alpha t \cos \phi}. \end{aligned} \quad (4.6)$$

Both parameters α and t are dimensionless and range from 0 to 1. $T_{RR}(\phi)$ is a symmetric function of ϕ , which only appears in the argument of a cosine. The transfer function also remains symmetric upon interchanging α and t , as is seen more evidently in the expanded Eq. 4.6. As a consequence, the two coefficients contribute similarly to the transfer function and thus are difficult to distinguish when fitting [73]. They can be disentangled by fitting to resonances measured from multiple devices or to a range of resonances from a single device because the propagation loss should remain constant as a function of wavelength or other device parameters (*e.g.*, coupling gap, ring radius) [73].

4.2.2 Asymmetric transfer function

We now add a pair of partial reflectors with reflectivities R_1 and R_2 to the waveguide in locations that surround the ring (Fig. 4.1c). Without loss of generality, we assume

that the ring is centered between the reflectors along a bus waveguide of length L .

The additional fields that are introduced are illustrated in Fig. 4.1b.

The original output a_2 now excites an output a_3 that is behind a partial reflector R_2 . With the reflector in place, this mode now also excites a left-traveling wave c_1 , yielding the following relation:

$$a_3 = \sqrt{1 - R_2^2} e^{-\alpha_z L/4} e^{i\varphi'} a_2 - R_2 e^{-\alpha_z L/4} e^{i\varphi'} c_1. \quad (4.7)$$

Both terms include the loss accumulated from propagating along half of the waveguide, and an additional propagation phase φ' .

The left-traveling wave c_1 excites a clockwise-propagating wave d_2 . The field d_2 propagates through the circumference of the ring and excites another left-traveling wave c_2 . The interaction is described by a pair of equations that are analogous to Eqs. 4.4–4.5:

$$d_2 = \sqrt{1 - t^2} c_1 + t \alpha e^{i\phi} d_2 \quad (4.8)$$

$$c_2 = t c_1 + \sqrt{1 - t^2} \alpha e^{i\phi} d_2. \quad (4.9)$$

The left-traveling wave c_2 reflects from the partial reflector R_1 and contributes to input a_1 , yielding

$$a_1 = \sqrt{1 - R_1^2} e^{-\alpha_z L/4} e^{i\varphi'} a_0 - R_1 e^{-\alpha_z L/4} e^{i\varphi'} c_2. \quad (4.10)$$

Equations 4.7–4.10, along with Eqs. 4.4–4.5, constitute the complete set of cou-

pled equations. Solving for the transmission yields our final equation:

$$\begin{aligned} T(\phi) &= \left| \frac{a_3}{a_0} \right|^2 \\ &= (1 - R_1^2)(1 - R_2^2)e^{-2\alpha_z L} \times \\ &\quad \left| \frac{(1 - \alpha t e^{i\phi})(t - \alpha e^{i\phi})}{(\alpha t e^{i\phi} - 1)^2 - \gamma e^{i\varphi}(\alpha e^{i\phi} - t)^2} \right|^2, \end{aligned} \quad (4.11)$$

with the substitutions:

$$\gamma \equiv |R_1 R_2 e^{-2\alpha_z L}| \quad (4.12)$$

$$\varphi \equiv 2\pi(2L)n_{\text{eff}}/\lambda + \varphi_0. \quad (4.13)$$

The additional coefficients γ and φ correspond to the loss and phase contributed by the bus waveguide, respectively. This result includes a new term, $e^{-2\alpha_z L}$, accounting for the propagation loss through the waveguide between the partial reflectors, and a new pair of phase terms: $2\pi(2L)n_{\text{eff}}/\lambda$, which accumulates along the length of the waveguide, and φ_0 , which is introduced by the reflections. As expected, this result reduces to the ideal case (Eq. 4.6) when the mirrors are removed ($R_1, R_2 \rightarrow 0$). If we have no coupling to the ring ($t \rightarrow 1$), we obtain the transmission for a Fabry-Perot etalon of length L with a pair of boundaries with reflectivity R_1 and R_2 [94]:

$$T_{\text{Fabry-Perot}}(\varphi) = \left| \frac{\sqrt{1 - R_1^2}\sqrt{1 - R_2^2}e^{-\alpha_z L}}{1 - R_1 R_2 e^{i\varphi} e^{-2\alpha_z L}} \right|^2. \quad (4.14)$$

We scale Eq. 4.11 so that the peak value measured at the output is 1. Doing so normalizes away any variables that are not explicit functions of ϕ or φ , and yields

$$\begin{aligned} \tilde{T}(\phi) &= \left| \frac{(1 - \alpha t e^{i\phi})(t - \alpha e^{i\phi})}{\gamma e^{i\varphi}(t - \alpha e^{i\phi})^2 - (1 - \alpha t e^{i\phi})^2} \right|^2 \\ &= T_{\text{RR}}(\phi) \left| \frac{1}{1 - \gamma e^{i\varphi} T_{\text{RR}}(\phi)} \right|^2. \end{aligned} \quad (4.15)$$

Equation 4.15 shows that $\tilde{T}(\phi)$ is just $T_{RR}(\phi)$ with a correction term tuned by the asymmetry parameter γ .

We will show that this equation can be used to extract propagation losses, even in the presence of strong boundary reflections.

4.2.3 Asymmetry threshold

If the reflections R_1 or R_2 are small and the bus waveguide is very long, the asymmetry parameter γ is correspondingly small. One might expect the asymmetric correction to $T_{RR}(\phi)$ to become negligible. However, even small γ values can lead to pronounced asymmetries in some configurations. The term with γ in the denominator dominates when

$$1 \ll \left| \frac{2\gamma e^{i\varphi}(t - \alpha e^{i\phi})^2}{(1 - \alpha t e^{i\phi})^2} \right|. \quad (4.16)$$

This means that the reflection term γ needs to be larger than a threshold value of

$$\gamma_{\text{threshold}} \equiv \frac{(1 - \alpha t)^2}{2|t + \alpha|^2}. \quad (4.17)$$

We expect reflections (and thus γ) to be very small so as not to observe any asymmetries. However, Eq. 4.17 shows that it is easy to obtain asymmetric resonances if both α and t approach 1, as is generally desired. As was mentioned previously, large values of α correspond to smaller rings or low propagation losses. For example, for a ring resonator with a diameter of 150 μm and a propagation loss of 0.5 dB/mm, $\alpha \approx 0.95$. In this case, $\gamma_{\text{threshold}} \approx 0.015$, and so just 1.5% reflections at the boundaries cause noticeable asymmetries. Above this threshold, the standard symmetric transfer function begins to fail. Functionally, this means that asymmetries can be suppressed

in systems with considerable propagation loss or with large rings. This low threshold also explains why asymmetries are so common in high- Q systems, and why it is hard to estimate the propagation loss using rings in low-loss systems.

4.3 Results and Discussion

4.3.1 Device geometry and simulation parameters

We use a commercial 2-dimensional finite difference time domain (2D-FDTD) solver and the effective index method [95] to simulate a micro-ring resonator in order to verify these equations. The device we model consists of a lossy silicon ($n = 3.5 + 0.0002i$) micro-racetrack resonator composed of 220 nm tall \times 300 nm wide waveguides on a silica ($n = 1.45$) substrate. For simplicity, we set the constituent materials to be dispersionless. The resonator parameters include a coupling length of 10 μm , an edge-to-edge coupling gap of 90 nm and a total ring circumference of 400 μm . This device is designed to achieve critical-coupling for TM-polarized light in the center of the telecom operation range, at $\lambda = 1550$ nm. The imaginary component of the index is selected to achieve a propagation loss near 5 dB/mm (Fig. 4.2a). Though this loss might appear significant, we use a small ring for α to remain large enough ($\alpha \approx 0.75$) so as not to suppress the effects we are studying. Both of these factors contribute to minimizing the simulation time. The complete set of parameters is summarized in Table 4.1.

The effective index method yields an effective index of $n_{\text{eff}} = 1.93$ for the waveguide and $n_{\text{eff}} = 1$ for all other regions. We calculate the propagation loss for TM-

Material index	$3.5 + 2 \times 10^{-4}i$
Substrate index	1.45
Waveguide width	300 nm
Waveguide height	220 nm
Ring circumference	400 μm
Coupling length	10 μm
Gap size	90 nm

Table 4.1: Device geometry

polarized light at $\lambda = 1550$ nm by performing a virtual cut-back method [96]; we monitor the transmitted light at various positions in the waveguide and perform a linear fit (Fig. 4.2a), yielding a propagation loss of 5.2 dB/mm. For the given ring circumference and propagation loss we calculate the loss coefficient at $\lambda = 1550$ nm to be $\alpha = 0.775$. The predicted α also includes the minimal scattering loss that results from the mode mismatch between the straight and bent parts of the race-track resonator (0.2% per junction). Given the selected parameters, we estimate the maximum loaded Q -factor to be $Q = \pi n_g / (\alpha_z \lambda) = 3.3 \times 10^3$ [68].

4.3.2 Symmetric resonances

Before tackling the asymmetric case with paired partial reflections, we begin by simulating an ideal ring resonator to demonstrate the propagation loss extraction method [73]. The transmission for TM-excitation in the geometry described above is shown in Fig. 4.2b. We observe equally spaced symmetric resonance peaks with

an average free spectral range of 3.14 nm (390 GHz). They possess extinction ratios in excess of 10 dB throughout the range of operation, confirming that the resonator is near-critically-coupled to the waveguide. The largest extinction ratio observed (33 dB) is located at $\lambda = 1546.2\text{nm}$, at the center of the operation range. This resonance has a loaded Q -factor of 3.0×10^3 . The resonances are symmetric and are fit to the traditional transfer function in Eq. 4.6 (Fig. 4.2c). The fits are consistently well-behaved, and yield a loss parameter α for each resonance. We calculate the propagation losses α_z for each resonance using Eq. 4.3 and plot them in Fig. 4.2d. The loss values extracted using this method consistently agree well with the propagation loss in Fig. 4.2a, with a geometric mean of 5.2 dB/mm. This result demonstrates that fitting to Eq. 4.6 is a reliable method for estimating the propagation loss of a waveguide for symmetric resonances.

4.3.3 Asymmetric resonances

In order for asymmetries to appear in the simulated transmission spectrum, we place partial reflectors into the waveguide. We insert partial reflectors into the simulation using artificial stitching errors. These errors routinely appear during the electron-beam lithography process and are caused by the misalignment of successive write-windows (Fig. 4.3a). We simulate the reflection coefficient for different gaps and offsets that might result from a stitching error (Fig. 4.3b). For a perfectly aligned pair of waveguides (*i.e.*, no stitching error) none of the light is reflected back towards the input, as expected. As the gap or offset increases, the reflected field grows. Counter-intuitively, above a certain gap size the reflected field decreases. This decrease is due

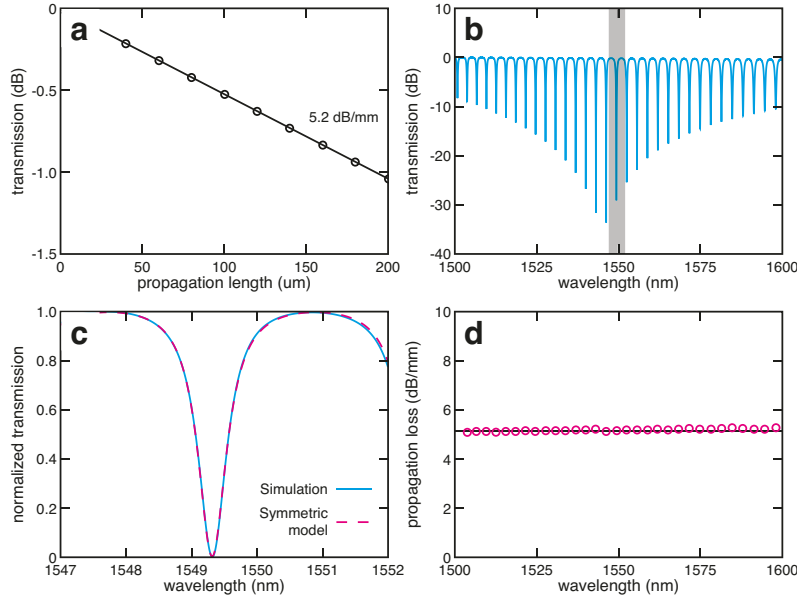


Figure 4.2: **a)** We obtain a propagation loss of 5.2 dB/mm for the waveguide used in the resonator by fitting to the transmission of a straight waveguide and extracting the slope. **b)** The transmission spectrum for TM-polarized light in a micro-racetrack resonator with a total circumference of 400 μm . We observe near-critical coupling throughout the wavelength range, peaking around $\lambda = 1550 \text{ nm}$. **c)** We fit to the resonance in the shaded region in **b** and obtain $\alpha = 0.774$. **d)** Extracted propagation loss from each individual resonance in **b** (circles). The mean propagation loss is 5.2 dB/mm, in agreement with the value fit in **a**.

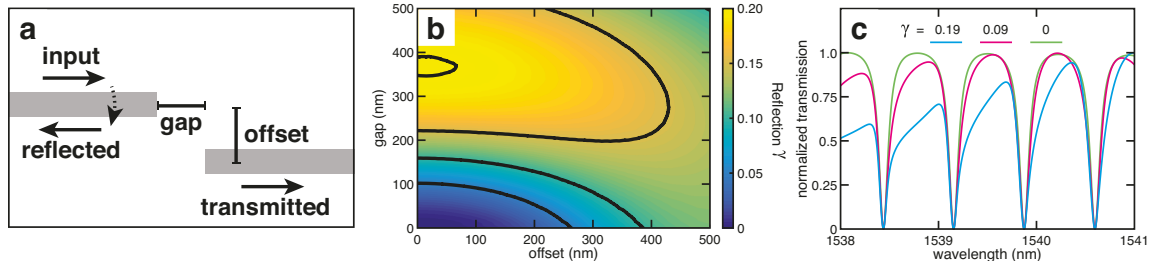


Figure 4.3: **a)** A pair of stitching errors in the waveguide surrounding the ring resonator can behave as the partial reflectors in Fig. 4.1b and cause asymmetries to form in the transmission spectrum of a ring resonator. We describe these errors using two parameters, an offset and a gap. **b)** Retrieved γ (corresponding to $|R_1 R_2|$) for different offsets and gaps. **c)** As the reflections included in the simulation become important, the asymmetries become more pronounced without displacing the original resonances.

to interference effects from the combined field within the gap — the field reflected from the end of the input waveguide interferes destructively with the field reflected from the beginning of the second waveguide. Figure 4.3b shows that stitching errors in our system yield a maximum reflection value of $\gamma = 0.2$. With $\alpha = 0.775$, Eq. 4.17 predicts that we need $\gamma > \gamma_{\text{threshold}} = 0.029$ before the transmission spectrum from the simulated device exhibits significant asymmetries.

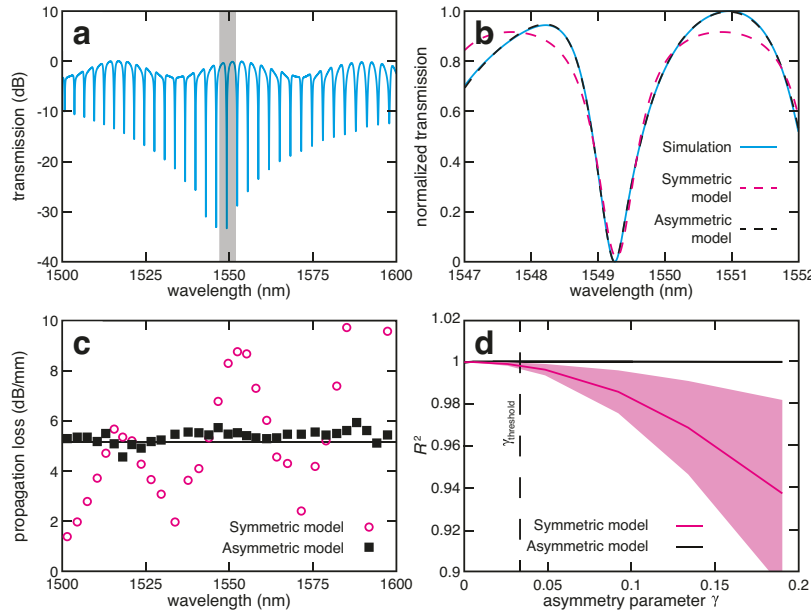


Figure 4.4: **a)** Transmission over the entire operation range for the device described in Section 4.3.3. **b)** Fits to the resonance in the shaded area in **a**, using both the standard symmetric model (red) and the asymmetric model developed in this work (black). The symmetric model fits the center of the resonances but is incapable of capturing the complete physics of the resonance. **c)** The asymmetric model predicts a propagation loss of 5.4 dB/mm while the symmetric model predicts an average propagation loss of 5.0 dB/mm. However, the standard symmetric model exhibits much larger oscillating deviations. **d)** Shaded error bar plot of averaged R^2 values of the fit to the transmission spectrum as a function of asymmetry γ . The R^2 values remain constant for all fits to the asymmetric model proposed in this work. On the other hand, the fit quality for the standard model declines once $\gamma > \gamma_{\text{threshold}}$.

We set the partial reflectors in our device to be stitching gaps that are 17 μm apart, surrounding the ring-coupling region. This length was chosen because it is not a multiple of the ring circumference (400 μm). We compare the effect of different asymmetry parameters γ by simulating devices with different stitching gap sizes of 300 nm (corresponding to $\gamma = 0.1902$), 200 nm ($\gamma = 0.1339$), 150 nm ($\gamma = 0.0921$), 100 nm ($\gamma = 0.0484$), 70 nm ($\gamma = 0.0259$) and 35 nm ($\gamma = 0.0053$). In Fig. 4.3c, we plot the transmission for the most extreme case with a gap size of 300 nm and the median case, with a gap size of 150 nm. We compare them to the ideal case from the previous section. As expected, the asymmetry increases with increasing γ .

The complete transmission spectrum for the device with the largest gap is shown in Fig. 4.4a. The familiar resonance peaks from Fig. 4.2b are superimposed with a slower secondary oscillation which adds characteristic asymmetries to the individual resonances. The resonances now also appear to possess different extinction ratios than their idealized counterparts. However, this apparent difference is an artifact of the superposition between the two oscillations.

We fit these resonances using both the standard symmetric transfer function $T_{RR}(\phi)$, and the asymmetric transfer function $\tilde{T}(\phi)$ (Fig. 4.4b). In simulation we know the length of the bus waveguide between the reflectors; however, if this length is unknown, its value could easily be determined by taking the Fourier transform of the measured transmission. The propagation loss extracted using both the symmetric and asymmetric transfer functions are plotted in Fig. 4.4c. The asymmetric function consistently predicts an average propagation loss of 5.4 dB/mm with a geometric standard deviation of 1.05, in agreement with the value extracted from the cut-back

simulation and the symmetric fits in Fig. 4.2. On the other hand, the standard transfer function $T_{RR}(\phi)$ predicts an average loss of 5.0 dB/mm with a geometric standard deviation of 1.70. This large standard deviation is evident in the drastic oscillations about the mean, with values ranging from 1.4 to 11.6 dB/mm. The asymmetric function fits the data significantly better when strong reflections are present. To demonstrate this quantitatively, we calculated the average R^2 for the fits in each spectrum. As can be seen in Fig. 4.4d, both transfer functions fit the data well when $\gamma < \gamma_{\text{threshold}} = 0.029$, but above this value the standard symmetric transfer function deviates significantly from $R^2 = 1$ with a large range of R^2 values, whereas the asymmetric transfer function remains at $R^2 = 1$ for every resonance.

4.4 Conclusion

We demonstrated that asymmetric resonances can result from purely linear effects in micro-ring resonators, such as partial reflections that are unavoidable in a realistic device or experimental setup. We derived and numerically verified a threshold above which the asymmetries become pronounced. Realistic devices easily exceed this threshold and therefore exhibit asymmetric resonances. The asymmetries are most pronounced in low-loss systems, where they appear for boundary reflections on the order of 1% or less. The reflectors do not need to be as close to each other as they are in this work — the asymmetries can just as easily originate from waveguide boundaries when the total waveguide length is comparable to the resonator length.

We derived a new transfer function that takes these asymmetries into account. The equations in this model reduce to their symmetric counterparts in the special case

of negligible reflections. This asymmetric transfer function outperforms the standard symmetric transfer function at modeling resonances from a ring resonator when the reflections are significantly above the threshold. The standard ring transfer function is therefore unreliable at extracting propagation losses, and the new asymmetric transfer function derived in this paper should be used in its place. As material deposition and fabrication techniques improve, losses will decrease and Q -factors will increase, exacerbating the prevalence of asymmetries in state-of-the-art devices and thus the need for a new model that can account for asymmetries.

Chapter 5

CMOS-compatible zero-index metamaterials

In this chapter, we present a monolithically integrated and CMOS-compatible photonic Dirac-cone-based metamaterial with an isotropic effective refractive index near zero. First, we will describe the physics and history of Dirac-cone-based metamaterials. Second, we will discuss our particular implementation and design strategies that are based on silicon-on-insulator technology. Third, we discuss the general properties of the metamaterial, including its isotropy and tolerances to fabrication imperfections. Next, we will experimentally demonstrate that this metamaterial possesses an effective refractive index of zero. Finally, we discuss the future outlook and applications of this new CMOS-compatible platform.

5.1 Introduction to zero-index metamaterials based on photonic Dirac cones

Metamaterials, composite materials with subwavelength inclusions, have allowed the photonics community to demonstrate extreme optical properties that are not typically found in nature. One exciting research direction is zero-index metamaterials (ZIMs) [25, 34, 97–100]. Materials with a refractive index of zero exhibit a number of striking and unintuitive properties, such as infinite phase velocities, large area single-mode operation, and angle-selective transmission. A flexible integrated ZIM enables many applications, such as supercoupling effects [29, 30, 33, 101] as well as fundamental tests in physics, including unique nonlinear phenomena [34, 35, 102].

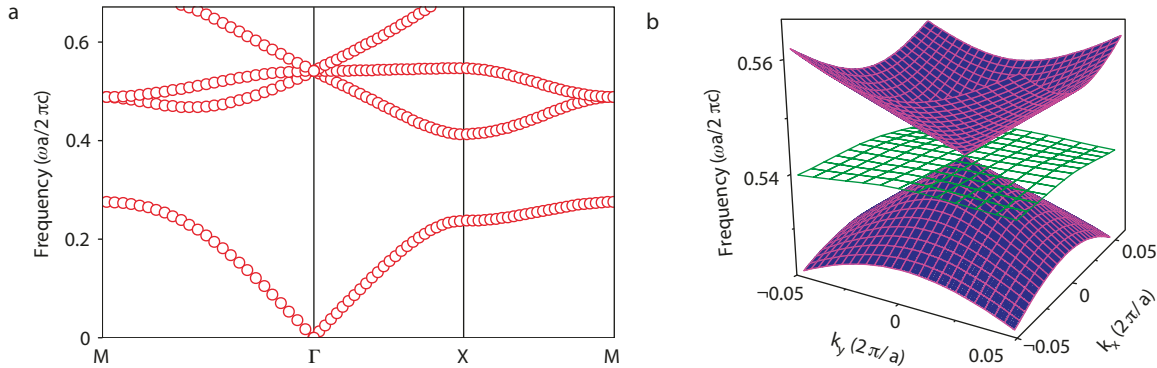


Figure 5.1: The band structure of a two-dimensional photonic crystal with a square lattice. **a)** The band structure for a 2D PC constructed of cylinders with radius $r = 0.2a$, relative permittivity $\epsilon = 12.5$ and permeability $\mu = 1$. Two linear dispersion bands intersect at the Dirac point $f = 0.541c/a$, with an additional flat band. **b)** Three-dimensional dispersion surfaces near the Dirac point frequency of the band structure shown in a, showing the relationship between the frequency and wave vectors (k_x and k_y). The linear bands (purple) form cones that touch at the Dirac point. There is an additional sheet (green) of quasi-longitudinal modes (from Ref. [97]).

In 2011, Huang *et al.* [97] used a 2-dimensional square array of infinitely-tall

dielectric pillars to design a photonic crystal that possessed a Dirac cone at the Γ -point, at the center of the Brillouin zone (Fig. 5.1). The cone was formed of a monopole mode and two dipole modes, one for each of the two propagation directions in the plane of the array. The two dipole modes combined to form a mode that points towards any arbitrary direction in the xy-plane. The parameters of the structure, which comprised the pitch a of the array, the radius r of the pillars, and the dielectric constant, were tuned so that the modes intersected at the Γ -point. They showed that this configuration corresponds to a metamaterial with an effective refractive index of zero, demonstrating near-zero phase advance at $f = 10.3$ GHz. This true “double-zero” material stands in stark contrast to “single-zero” materials, such as epsilon-near-zero (ENZ) or mu-near-zero (MNZ) materials [29, 30, 35, 103]. ENZ and MNZ materials possess impedances $\eta \equiv \sqrt{\mu/\epsilon}$ of 0 or ∞ which makes them act as perfect reflectors. By comparison, a double-zero material has both epsilon and mu gradually and simultaneously crossing zero. This yields a finite impedance and completely avoids this problem.

This work was followed by similar demonstrations in the telecom regime, using silicon pillars in glass [98, 99] or silicon pillars in air [100]. The latter demonstrations featured vertically-oriented pillars structured from a standard silicon-on-insulator (SOI) substrate. This on-chip configuration allows for flexible device design and enables integration with silicon photonic waveguides and optical components, such as resonators and interferometers. Unfortunately, the metamaterial design parameters required tall pillars — upwards of 500-nm — to obtain the desired resonances and modal degeneracy. This criterion presents many obstacles towards the adoption of the

on-chip zero-index platform. For example, single-mode operation becomes challenging in the telecom regime by necessitating prohibitively tall waveguides with large aspect ratios. These integrated ZIMs have prohibitively difficult fabrication procedures or incorporate expensive materials such as gold. These properties will ultimately slow down industry adoption of these platforms and will limit possible applications.

To address this issue, we have developed a zero-index metamaterial (ZIM) formed from a thinner base film. This was achieved by inverting the previously demonstrated structures, *i.e.*, etching circular holes into a silicon matrix. Since the background of this structure is formed from a high-index slab, the light cone is drastically raised, providing improved vertical confinement [104]. We also move towards transverse electric-(TE-)polarized operation (*i.e.*, electric field polarized parallel to the plane of the device), whose modes are better confined in thinner films due to boundary conditions [94].

5.2 Dirac cones in square arrays of holes in a dielectric matrix

We begin by studying an equivalent two-dimensional structure in order to build intuition about this inverted airhole array. We simulate a bulk silicon ($n = 3.48$) matrix and tune the parameters (pitch and radius) of a square array of infinitely-tall holes (Fig. 5.2a). For an array with a pitch of $a = 582.8$ nm and a hole radius of $r = 182.0$ nm, a Dirac cone forms at the Γ -point at $f = 193.4$ THz (*i.e.*, $\lambda = 1550$ nm). We call this frequency the zero-index frequency. In Fig. 5.2b, we plot the resulting

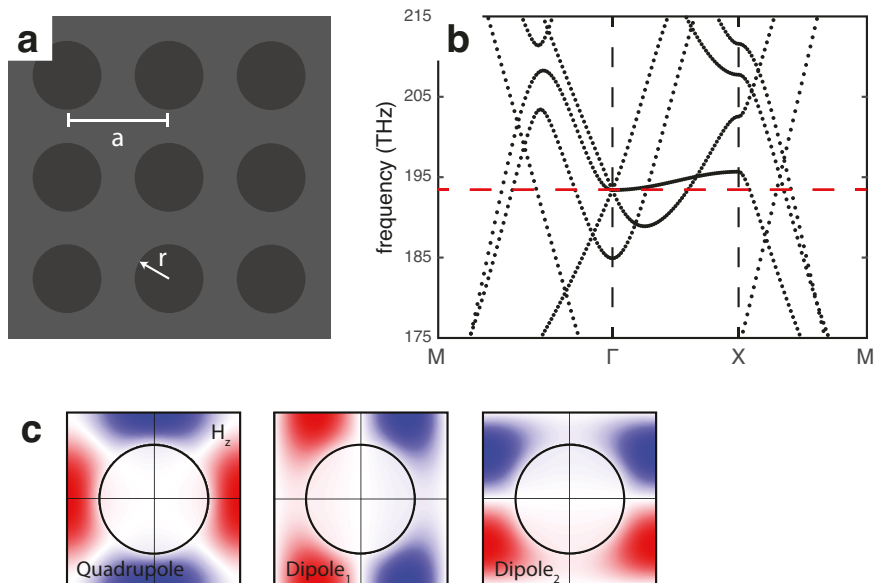


Figure 5.2: **a)** A two-dimensional square array of holes in a silicon matrix, with a lattice constant a and a radius r . **b)** The band structure for this structure with $a = 582.8$ nm and $r = 182.0$ nm. The dashed red line indicates the operating frequency, $f = 193.4$ THz. **c)** The out-of-plane component of the H-field H_z of the three modes that intersect at the Γ -point.

band structure for TE-polarized excitation. The bands that form the cone intersect linearly. At shorter frequencies, a photonic band gap appears in the Γ -X direction. In Fig. 5.2c, we show the field profiles of the three degenerate modes at the Γ -point. Here, they are composed of two dipole modes and a quadrupole mode. As in the TM-polarized rod case, the two dipole modes can be combined to form a mode that points towards any arbitrary direction in the xy-plane.

5.3 Dirac cones in silicon-on-insulator technologies

In order to adapt the presented design into a fully-fabricable 3-dimensional structure, we perform the same procedure outlined above for the case of a 220-nm tall Si-on-SiO₂ film (Fig. 5.3a). This film thickness is selected due to its compatibility with the CMOS fabrication process, and because of the well-established single-mode condition for TE-polarized light [105]. For a square array airhole structure with a pitch of $a = 728$ nm and a radius of $r = 222$ nm, we obtain the band structure in Fig. 5.3a. We observe three modes intersecting at the Γ -point, forming a photonic Dirac cone at $f = 193.4$ THz. As in the 2D case, two of the modes are dipoles and the third is a quadrupole mode. In fact, as displayed in Fig. 5.3c, slices of these modes taken at the center of the slab are extremely similar to their respective 2D counterparts in Fig. 5.2c. Unlike in the 2D case, the three bands that form the cone no longer intersect linearly. Instead, both bands possess a quadratic dispersion. This is caused by the two modes possessing radically different quality factors, which breaks the degeneracy for the complex eigenfrequencies [106]. Despite being above the light line, the quadrupole mode cannot couple to plane waves that propagate in free space due

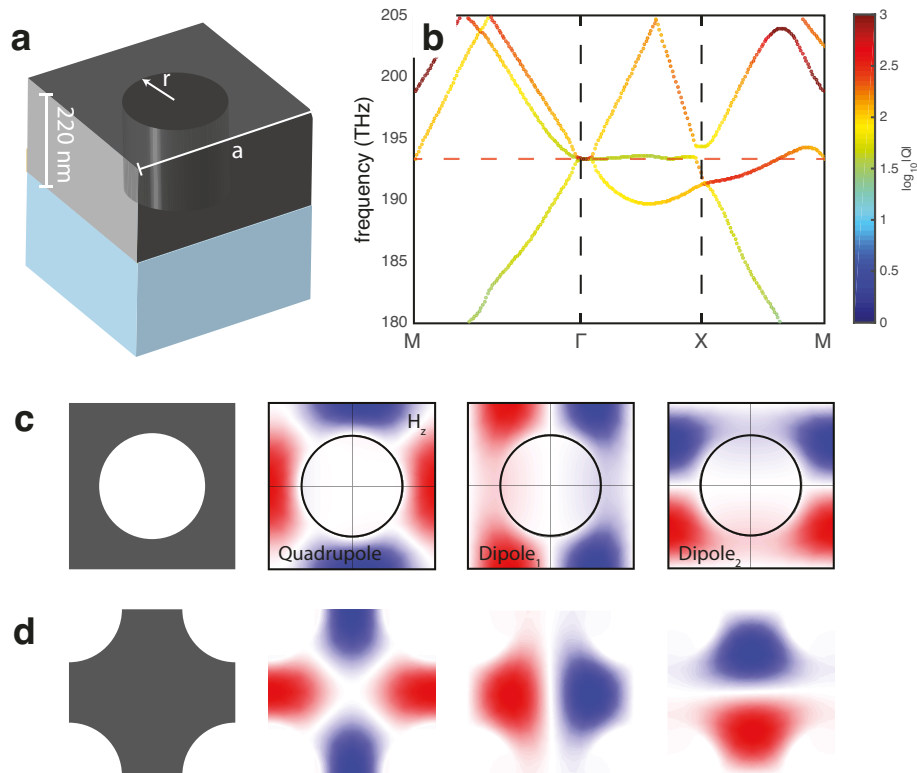


Figure 5.3: **a)** A unit cell of the designed airhole structure in a 220-nm tall Si-on-SiO₂ film. **b)** The band structure for a two-dimensional square array of this structure with a pitch of $a = 728$ nm and a radius of $r = 222$ nm. The Q -factor peaks for the modes at the Γ -point. **c)** The out-of-plane component of the H-field H_z of the three modes that intersect at the Γ -point. The modes resemble their 2D analogs in Fig. 5.2c. **d)** The modes in (c) with the resonator centered in the unit cell.

to its symmetry, leading to high quality-factors. This is clearly illustrated by the color bar in Fig. 5.3b, where the Q -factor peaks above 10^5 for one of the modes at the Γ -point. As we will demonstrate in the following section, this change in the dispersion profile does not significantly impact the device performance. Finally, we note that a limitation of the proposed design is the band gap that appears for smaller frequencies in the Γ -X direction, below $f = 189.7$ THz.

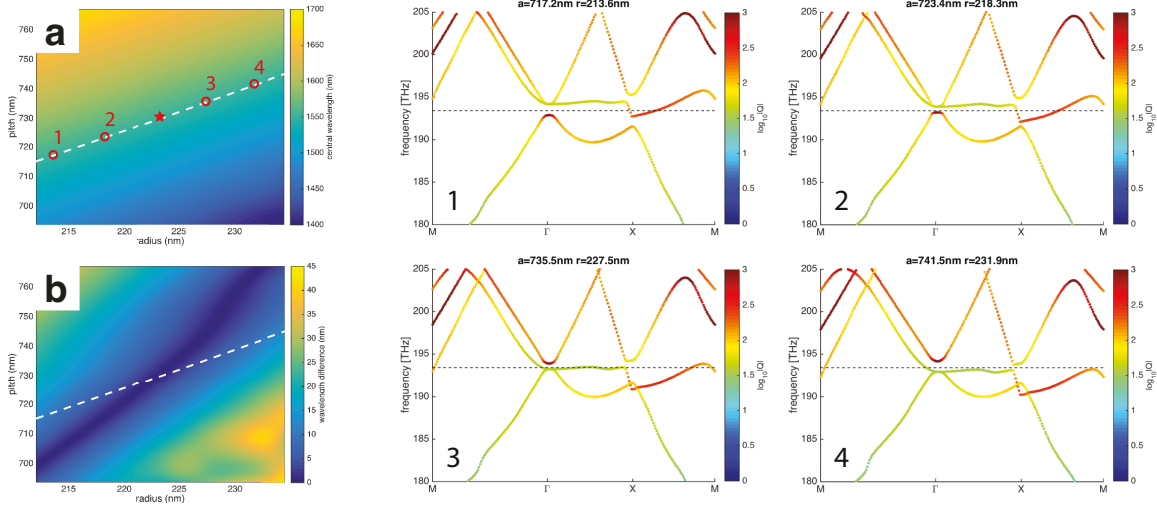


Figure 5.4: **a)** Average wavelength between the dipole and quadrupole modes at the Γ -point as a function of the lattice parameters. **b)** Size of the bandgap as a function of the lattice parameters. The line where the average eigenfrequency matches our design wavelength ($\lambda = 1550$ nm) is indicated by the dashed white line in both (a) and (b). On the right hand side, we calculate the full band structure for the structures indicated in (a). The star in the center of the simulation region corresponds to the optimal structure, which is fully described in Fig. 5.3

We study the fabrication tolerance of the design by examining the modal eigenfrequencies as a function of the lattice constants. We calculate the modes at the center of the Brillouin zone for pitches and radii that are shifted by up to $\pm 5\%$ from the optimal device parameters, with pitches ranging from about $a = 695$ nm to $a = 765$ nm

and for hole radii of about $r = 210$ nm to $r = 235$ nm. We distinguish the quadrupole modes from the dipole modes by their quality factors. In Fig. 5.4a, we plot the average eigenfrequency as a function of the lattice parameters. A valley appears where the two modes are equidistant from the operation wavelength ($\lambda = 1550$ nm), as indicated by a white dashed line. We calculate the band structure at multiple points (Fig. 5.4) along this line. As we go from smaller dimensions to larger ones, the gap between the higher frequency dipole modes and the lower frequency quadrupole mode decreases until we reach the optimal structure with modal degeneracy. For even larger sizes, the gap once again increases; however, as the eigenfrequency of the dipole modes keeps getting reduced and the eigenfrequency of the quadrupole mode keeps increasing, the position of the modes with respect to the operating frequency is actually reversed. We also show the absolute difference between the modal eigenfrequencies for the same geometries (Fig. 5.4b). We conclude that for a given operating frequency in the range of our chosen operating wavelength, there exists only a single geometry that provides perfect modal degeneracy for zero-index operation. If we allow a small bandgap of 1 nm to form between the modes, we can tolerate a fabrication imperfection of $\pm 0.3\%$ (≈ 2 nm) in the pitch and an imperfection of $\pm 0.8\%$ (≈ 2 nm) in the hole radii while still maintaining near-degeneracy at one particular wavelength.

In Fig. 5.5, we plot the complete dispersion surface for the modes that form the cone, demonstrating the finely-tuned degeneracy between the modes of interest at the selected frequency. As the operating frequency strays from the zero-index frequency, the modes supported by this structure form circles in the Brillouin zone. At larger deviations, the circles gradually relax into supercircles, which obey the relation

$x^n + y^n = r^n$. This is illustrated more clearly by slicing the cone into its equifrequency contours, as shown in Fig. 5.6a-b. We fit each contour to a supercircle, and plot the extracted radii r and supercircle orders n in Fig. 5.6c-d. The equifrequency contours fit to perfect circles when $n = 2$, indicating that the modes are isotropically distributed around the Γ -point. Fig. 5.6d indicates that the structure behaves like an isotropic metamaterial for the frequencies between $f \approx 192 - 195$ THz, corresponding to over 20 nm of bandwidth surrounding $\lambda = 1550$ nm. In Fig. 5.6c, the extracted supercircle radii first decrease and then increase as a function of frequency, both with a very linear trend ($R^2 > 0.99$), further strengthening the claim that the structure behaves like an isotropic metamaterial.

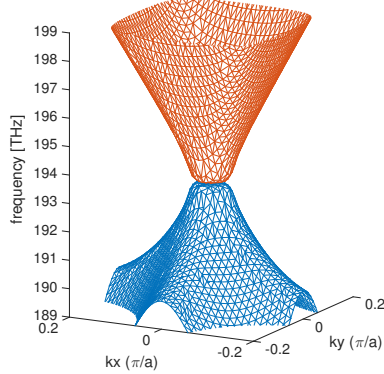


Figure 5.5: The dispersion surface at the center of the reduced Brillouin zone for the proposed structure, analogous to Fig. 5.1b. The modes form a photonic Dirac cone at the Γ -point. The flat band, which corresponds to the quasi-longitudinal dipole mode, has been omitted for clarity.

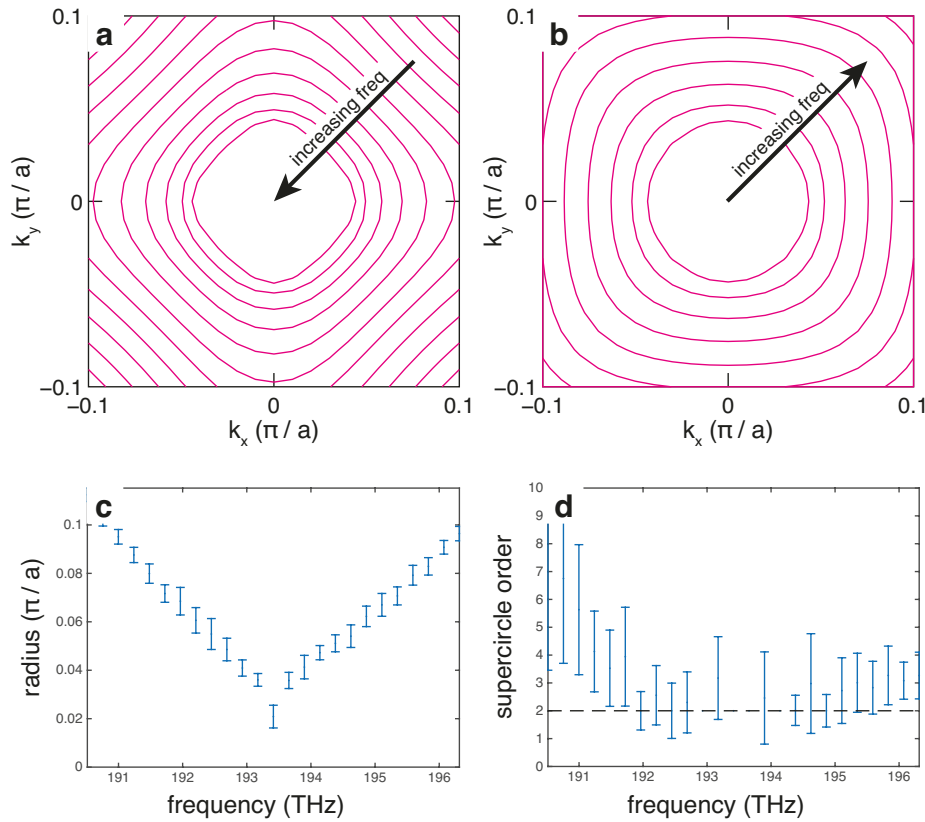


Figure 5.6: (a-b) Equifrequency contours for the dispersion surface in Fig. 5.5. The contours obey the relation $k_x^n + k_y^n = r^n$ throughout the entire range of operation studied (e.g., 191 – 196 THz). (c-d) Extracted radii r and supercircle order n with 95% confidence intervals.

5.4 Effective refractive index determination

5.4.1 Parameter retrieval

The features that we have described in the band structure so far are consistent with the claim that our proposed structure has an isotropic effective refractive index near zero. In order to more rigorously determine the index of the structure, we simulate the transmission of the fundamental TE-polarized mode of a 2D-slab through a row of airhole unit cells. We monitor the transmitted and reflected fields and perform a parameter retrieval on the scattered fields [107]. This procedure yields complex values for the effective permittivities and permeabilities, or alternatively, the effective refractive index and impedance. We plot the real and imaginary components of the effective refractive index in Fig. 5.7a. The real part of the index smoothly and linearly decreases from positive values towards negative values, with an effective index of 0 near $\lambda = 1550$ nm. The imaginary component of the refractive index at this wavelength is $\Im[n_{\text{eff}}] = 0.054$, which is comparable to the imaginary index of $\Im[n_{\text{eff}}] = 0.046$ achieved for the original integrated ZIM implementation which featured gold-clad silicon rods in a polymer (SU-8) matrix [99]. As the wavelength increases from this point, the imaginary component increases drastically. This is due to the appearance of a photonic band gap, as illustrated in Fig. 5.3b. Finally, we note that at the zero-index frequency, the real components of the retrieved effective permittivity ϵ_{eff} and permeability μ_{eff} both simultaneously cross zero, as well, corresponding to a true impedance-matched “double-zero” material.

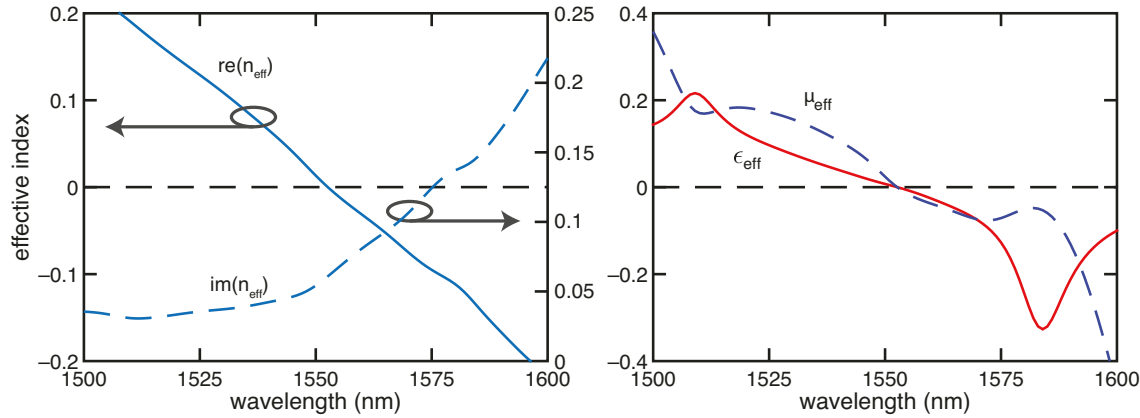


Figure 5.7: **a)** Retrieved real and imaginary components of the effective refractive index, indicating a zero-index wavelength at $\lambda = 1550$ nm. **b)** The real components of the retrieved effective permittivity ϵ_{eff} and permeability μ_{eff} both simultaneously cross zero at $\lambda = 1550$ nm.

5.4.2 Experimental verification

In order to experimentally measure the index of the material, we create a right-angled prism formed from a 20×20 cell array (Fig. 5.8a). The fabrication procedure follows a standard silicon photonics fabrication process. We begin with 220 nm-thick SOI wafer, and pattern a layer of negative-tone resist (XR 6%) in a single step of electron-beam lithography. We follow this step by inductively-coupled plasma reactive ion etching (ICP RIE) the sample in a $\text{SF}_6:\text{C}_4\text{F}_8$ atmosphere at a ratio of 13 : 8 until the pattern is completely transferred into the silicon device layer.

A TE-polarized input beam is introduced onto one face of the prism using a silicon waveguide the width of the input face of the prism. At the zero-index frequency, we expect light to exit the prism at an angle α that is normal to all of its faces ($\alpha \rightarrow 0^\circ$), regardless of the index of the surrounding medium. This is trivially

derived using Snell's law:

$$\begin{aligned}\sin(\alpha) &= \frac{n_1 \sin(45^\circ)}{n_2} \\ n_1 = 0 &\implies \alpha = 0.\end{aligned}$$

The output from the prism is collected in a 1.5- μm -tall SU-8 slab waveguide shaped like a semicircle with a diameter of 1 mm. Under the output face of the slab waveguide is a silicon ring designed to scatter light into an imaging objective above the chip. Fig. 5.8b shows the resulting image at $\lambda = 1640$ nm. This wavelength is 5% larger than the designed operating wavelength, within the expected fabrication tolerances of e-beam lithography. A beam appears at $\alpha = 0^\circ$, corresponding to refraction through a prism with a refractive index of zero. A secondary beam appears at $\alpha = 45^\circ$; this corresponds to the output for TM-polarized input, in agreement with simulations. We could eliminate this beam by using a polarizer at the input and by polishing the input facet to prevent polarization scrambling.

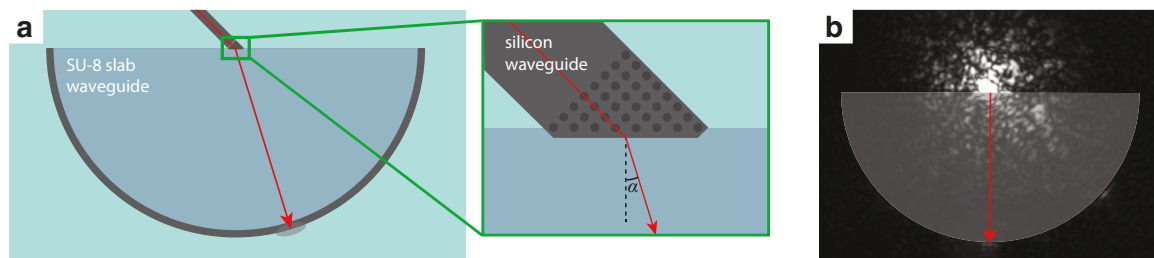


Figure 5.8: **a)** The fabricated chip and the experimental setup. **b)** An image of unpolarized light at $\lambda = 1640$ nm, showing a clear beam at $\alpha = 0^\circ$, confirming that the prism has an effective refractive index of zero. The fabricated output slab is artificially overlaid on top of the image.

We repeat the measurement by sweeping the wavelengths from $\lambda = 1480 - 1680$ nm at an interval of $\Delta\lambda = 1$ nm. The intensity at the outer scattering ring is plotted as a function of wavelength in Fig. 5.9b. We see the beam smoothly decreasing

from positive angles at shorter wavelengths to negative angles at longer wavelengths, crossing $\alpha = 0^\circ$ at around $\lambda = 1640$ nm. We interpret this to mean that the prism possesses a small positive effective refractive index at shorter wavelengths, an index of 0 around $\lambda = 1640$ nm, and a small negative index at larger wavelengths. This trend agrees qualitatively with the retrieved index in Fig. 5.7. Additionally, we show the matching simulation for the ideal device dimensions in Fig. 5.9a. We observe excellent qualitative agreement between the simulated and measured far-field patterns.

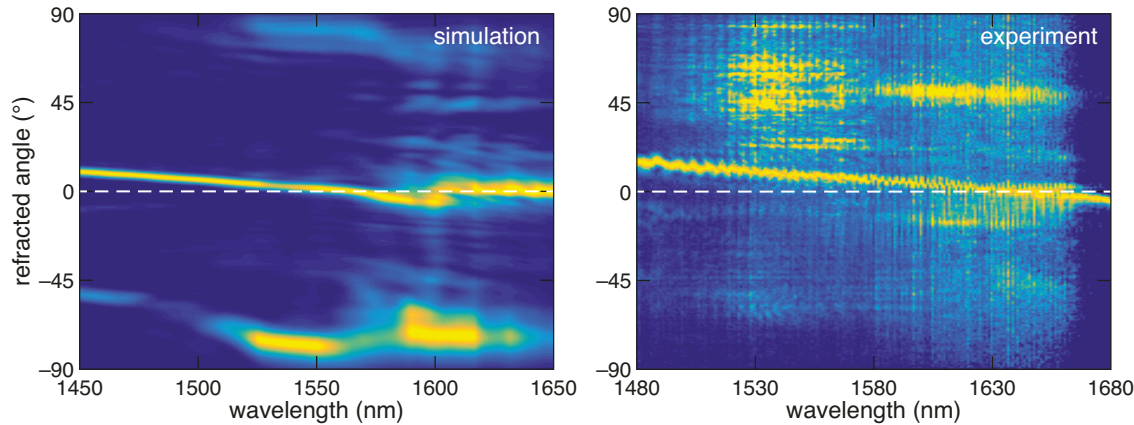


Figure 5.9: Simulated (left) and experimental (right) far-field patterns from a right-angled prism formed of 20×20 unit cells of the proposed airhole structure. The data is normalized at every wavelength. In both figures, the refracted beam crosses through $\alpha = 0^\circ$, indicating an effective refractive index of zero. The secondary dominant beam that appears at 45° in the experimental data corresponds to unfiltered TM-polarized light from the input.

5.5 Discussion and conclusion

We have designed and characterized a CMOS-compatible Dirac-cone-based metamaterial with an isotropic effective refractive index near zero. For a given polarization,

we observe refraction normal to a right-angled triangular prism of this metamaterial, consistent with an effective refractive index of zero. The presented design also provides access to small isotropic positive and negative refractive indices. Interferometric experiments would be required in order to unambiguously characterize the refractive index of this metamaterial further [108, 109].

The presented platform utilizes a structured monolithic slab of silicon with a carefully tuned square array of cylindrical holes. The design does not depend on any unique silicon material properties, and in fact could be trivially adapted to other mature transparent high-index photonic platforms. With some exploration, a recipe based on the work in this chapter could also possibly be devised for materials with lower refractive indices.

Though this latest design marks a significant improvement over previously demonstrated ZIMs in terms of practicality and integration, its modes are still located at the Γ -point above the light line. Thus, this metamaterial still possesses a considerable intrinsic loss on the order of a few dB/ μm . As these losses are purely radiative and not due to any intrinsic material properties, this can be avoided by embedding the states within a bound state in continuum [110, 111].

Unlike its predecessors, this integrated metamaterial was engineered to be structured from a relatively thin film, and it does not necessitate any additional polymers or metals. This advance was achieved by inverting the original silicon pillar design, *i.e.*, by placing “air cylinders” into a silicon background. The large effective index of the silicon slab in the background provides some additional confinement. This move enables practical integration with the wealth of silicon photonic components that have

been designed using 220-nm-thick SOI.

Chapter 6

Zero-index waveguides

We design and experimentally demonstrate 1-dimensional zero-index waveguides. We integrate the silicon-based zero-index metamaterial with photonic band gap materials to reduce the propagation losses from $1.26 \text{ dB}/\mu\text{m}$ to $0.89 \text{ dB}/\mu\text{m}$, corresponding to a 30% improvement. Finally, we propose and experimentally demonstrate a novel interferometric technique to extract the effective index of low-index waveguide channels.

6.1 Introduction

The all-dielectric zero-index platform that was presented in the previous chapter opens up many avenues for both fundamental experiments as well as photonic applications. With an integrated zero-index channel, we can arbitrarily route light along sharp bends using the super-coupling effect or study new arrangements in nonlinear phase-matching [29, 30, 33, 34, 101, 102]. However, there remain some obstacles that must be

addressed before we can begin to probe these applications.

First, it is unclear how narrow a channel can be employed (*i.e.*, how many unit cells are necessary) while still preserving the symmetry and degeneracy of the modes, maintaining an effective index of zero along the direction of propagation. If a device that is a single unit cell wide can still exhibit the correct zero-index modes, it is also unknown whether or not a single-mode SOI waveguide can excite them efficiently within the structure. Second, the nature of an isotropic zero-index material is to radiate normal to its faces, which unavoidably contributes to the propagation loss of these waveguides. Many potential applications for integrated photonics rely on long-range propagation, which would significantly limit the feasibility of zero-index devices. Finally, experiments that have so far been used to determine the effective index for these low-index platforms have necessitated that the metamaterial be in the shape of a prism [99, 100]. This further restricts the arrangement of the platform, impacting potential applications.

In this chapter, we design and characterize zero-index waveguides that are a single unit cell wide ($\approx \lambda/2$). We exploit the ease of integration with silicon photonics to partially mitigate the radiative propagation loss caused by the low effective index. Finally, we propose and experimentally demonstrate a novel interferometric technique to extract the effective index of low-index waveguide channels. Unlike previous measurements, this approach can be implemented in-situ to directly observe the effective index within a device, rather than requiring an additional interferometric measurement structure.

6.2 Design and simulation

As light propagates through any zero-index medium, it is partially emitted normal to its sides, an intrinsic property of a material with a refractive index of zero. If we were to form a waveguide of this medium, this emission would contribute to the propagation loss of the waveguide. Radiative losses could be mitigated in part if the emitted light could be reflected and returned to the waveguide with a 2π phase shift. Fortunately, at the zero-index wavelength, light couples perfectly to plane waves pointing normal to every surface. Adding a perfect reflector an appropriate distance from the waveguides could reverse these waves, completely canceling out this radiation and reducing the propagation loss of these waveguides, while maintaining an effective phase advance of zero.

6.2.1 On-chip photonic band gap materials

Since the zero-index platform is compatible with silicon photonics, we have the option to use photonic band gap materials (PBGs) as on-chip reflectors. Integrating these materials with a zero-index waveguide is seamless (Fig. 6.1). We employ a triangular lattice of holes with a lattice constant of $a_{\text{PBG}} = 450 \text{ nm}$ and a hole radius of $r_{\text{PBG}} = 124 \text{ nm}$. This geometry provides a PBG for all TE-polarized light at $f = 194.3 \text{ THz}$ ($\lambda = 1550 \text{ nm}$) with a large bandwidth of $\Delta f = 37 \text{ THz}$ (Fig. 6.1b).

We place a single row of zero-index unit cells between multiple layers of PBG. Between the zero-index waveguide and the PBGs, the silicon is entirely etched away to leave a gap. Without this gap, the zero-index resonators are no longer freestanding and the modes in the metamaterial are perturbed which impedes the desired operation

of the device.

We empirically determine the correct spacing L between the PBG and the ZIM channel by performing full-wave simulations. Using FDTD, we couple light into a device comprised of 6 unit cells of ZIM using a silicon waveguide and collect the output using a transmission monitor in another waveguide at the opposite end. We sweep the spacing L and measure the transmission into the fundamental mode of the output waveguide. The measured output is reduced by a radiative propagation loss, coupling loss to and from the device from the interfacing waveguides, and the minimal absorption losses in the silicon. As L is changed, we expect any changes in transmission to be due to a reduction in radiative losses only, so long as the modes of the structure remain unperturbed. The transmission in the fundamental mode of the output waveguide as a function of L is shown in Fig. 6.1c. As the reflectors approach from infinity, the waves reflected from the PBG begin to interfere with the light propagating in the waveguide, first constructively at a spacing of roughly $L = 1000$ nm, then destructively at a spacing of $L = 720$ nm. There is then a large region of constructive interference, ranging from a spacing of 133 nm to 573 nm, with a maximum roughly at the center, for a spacing of $L = 330$ nm. This spacing is selected as the design spacing for the reflector.

6.2.2 Waveguide propagation

As this new hybrid structure is no longer periodic along the direction of propagation, we can not calculate a band structure to examine its dispersive properties. Instead, we measure the average phase advance between unit cells using phase monitors in FDTD,

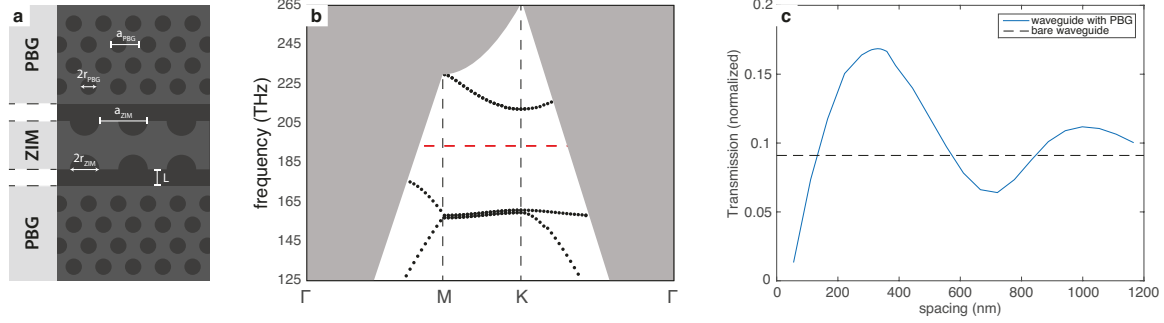


Figure 6.1: **a)** Schematic for a 1-channel-wide zero-index waveguide, cladded by a photonic crystal that possesses a band gap at the operating frequency. **b)** Photonic band structure for the PBG photonic crystal. There are no states available around the operating frequency ($f = 194.3$ THz), as indicated by the red-dash line. **c)** Transmission after propagating through 6 unit cells of the structure in (a) as a function of the spacing between the PBG lattice and the zero-index waveguide, L . An optimum at which the PBG provides the strongest constructive interference (corresponding to the overall lowest propagation loss) is found at $L = 330$ nm.

and extract an effective index which we plot in (Fig. 6.2a). We also plot the retrieved effective index of the bare zero-index waveguide on the same axes for comparison. We observe a good qualitative agreement between the two devices. Notably, we maintain a zero-index crossing at approximately the same wavelength in both devices.

Next, we look at the fields in the horizontal cross-section midway through the device (Fig. 6.2b-c). The structure of the modes excited within the device is observed to be insensitive to the addition of PBGs. In both structures, the amplitude of the fields decreases due to propagation loss; however, light excited in the waveguide cladded by PBGs decays more slowly. To estimate this change in propagation loss more quantitatively, we perform a virtual cut-back measurement by simulating waveguides with 2 – 9 pitches of ZIM waveguides both with and without the PBG cladding (Fig. 6.2d). For comparison, we also simulate a periodic zero-index metamaterial that is infinitely-wide, *i.e.*, that does not exhibit a radiation loss out of the

sides of the waveguide. We fit to the transmitted output and extract a propagation loss of $2.21 \text{ dB}/\mu\text{m}$ for the bare zero-index waveguides, and a propagation loss of $1.47 \text{ dB}/\mu\text{m}$ for the PBG-cladded zero-index waveguides, corresponding to an improvement of over 30%. The coupling loss of $0.3 \text{ dB}/\text{interface}$ is identical for both devices, further confirming that the modes are not perturbed by the presence of the PBG. The periodic structure exhibits a propagation loss of $1.12 \text{ dB}/\mu\text{m}$, which is lower than either two waveguides, as expected.

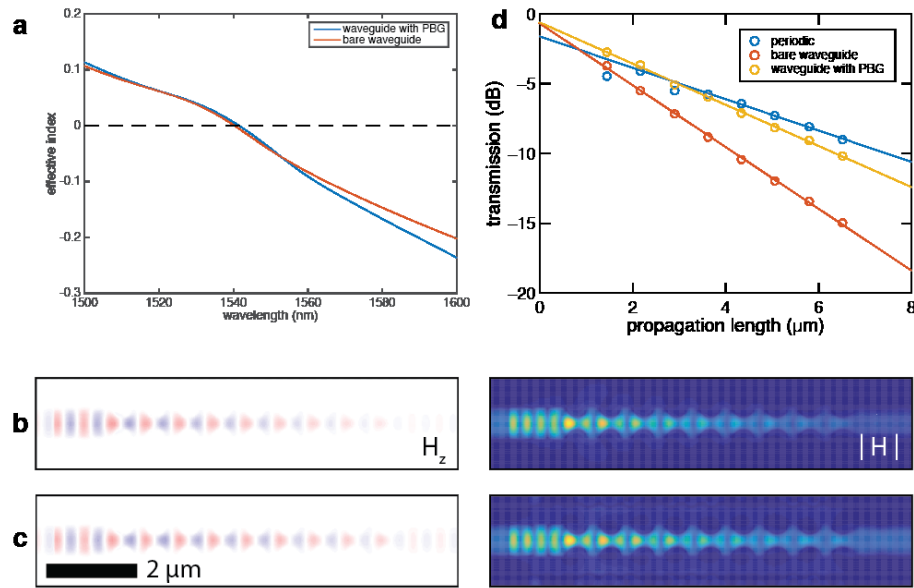


Figure 6.2: **a)** Retrieved effective index for the zero-index waveguide both with and without the PBG cladding. Both devices demonstrate a zero-crossing at approximately $\lambda = 1530 \text{ nm}$. **b)** 3D-FDTD simulation of the out-of-plane \vec{H} -field component and the magnitude of the field $|\vec{H}|$ for a bare zero-index waveguide excited by a TE-polarized single-mode waveguide. **c)** Simulated out-of-plane \vec{H} -field component and the magnitude of the field $|\vec{H}|$ for the PBG-cladded zero-index waveguide. **d)** Simulated transmission into the fundamental mode for waveguides of different lengths, which yields propagation losses. Also plotted for comparison is a simulation for a structure that is surrounded on either side by periodic boundary conditions. This structure should only have out-of-plane radiative losses.

These simulations demonstrate that a bare zero-index waveguide that is only a single unit cell wide has an effective refractive index of zero. The addition of a PBG cladding maintains this refractive index profile while reducing the propagation loss of the waveguide by 30%. Both of these waveguides couple well to ordinary silicon waveguides, with a coupling loss of 0.3 dB/interface. In the next few sections, we explore these devices experimentally.

6.3 Experimental

6.3.1 Fabrication

To fabricate the structures, we begin with a 220-nm silicon-on-insulator wafer. We spin on a layer of negative-tone resist (XR 6%) and write the pattern using electron-beam lithography. The sample is then developed in tetramethylammonium hydroxide (TMAH) and the pattern is transferred to the silicon substrate using inductively-coupled plasma reactive ion etching (ICP-RIE) in a SF₆:C₄F₈ atmosphere at a ratio of 13:8. In Fig. 6.3, we show a pair of finalized structures. Each device tapers on both sides into single mode 500 nm × 220 nm waveguides which in turn couple into large 2.5 μm × 2 μm polymer (SU-8) coupling pads. The pads are cleaved at both ends of the chip to prepare input facets.

6.3.2 Index retrieval

The shape of the zero-index waveguides, specifically their 1-dimensional nature, means that we cannot perform a refraction experiment such as the one that was done in

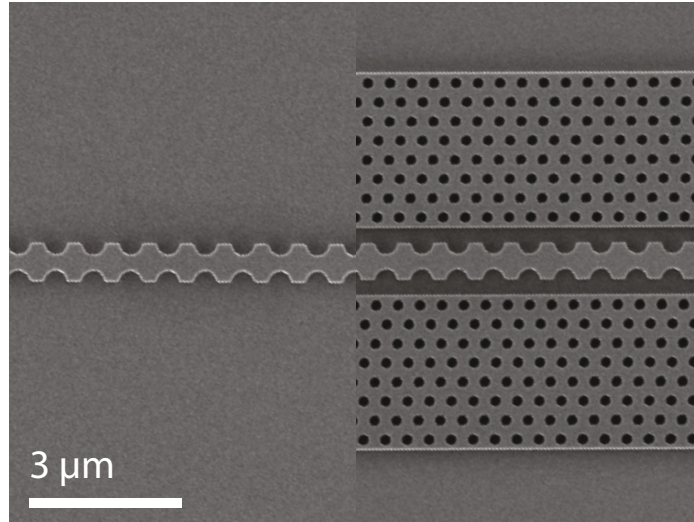


Figure 6.3: (left) Scanning electron microscope image of a bare zero-index waveguide. (right) An identical waveguide surrounded on each side by 4 pitches of a triangular-lattice PBGs.

Section 5.4.2 using a prism. In order to unambiguously characterize the effective index of an integrated waveguide structure, we would typically need to build a bulky and complicated interferometric setup and perform careful transmission and reflection measurements. Alternatively, we could design the device with an integrated silicon-based Mach-Zehnder interferometer and perform this measurement entirely on-chip. However, this kind of configuration would prevent the use of those waveguides for most other experiments.

Fortunately, the small effective index of ZIM devices enables an interferometric measurement that would be otherwise inaccessible. This technique can be used with low-index devices in any configuration with at least two inputs to determine the absolute value of their effective index. First, the device is excited from both sides. This forms a standing wave that can be imaged using an infrared camera. The combined intensity of the interference pattern formed by a pair of counter-propagating

CW waves of equal amplitude in a waveguide with an effective index of n_{eff} is

$$\begin{aligned} |\vec{E}(z)|^2 &\propto \left| e^{-i\frac{2\pi n_{\text{eff}}}{\lambda}z} + e^{i\frac{2\pi n_{\text{eff}}}{\lambda}z+\varphi} \right|^2 \\ &= 4 \cos^2 \left(\frac{2\pi n_{\text{eff}}}{\lambda}z - \frac{\varphi}{2} \right), \end{aligned} \quad (6.1)$$

where φ represents the relative phase between the two waves. Nodes appear in the intensity pattern when the argument of the cosine is

$$\frac{2\pi n_{\text{eff}}}{\lambda}z - \frac{\varphi}{2} = \frac{\pi}{2}(2m+1) \quad (6.2)$$

for some integer m . This means that the distance between successive nodes is

$$\begin{aligned} \frac{2\pi n_{\text{eff}}}{\lambda}(\Delta z) &= \pi \\ \implies \Delta z &= \frac{\lambda}{2n_{\text{eff}}}. \end{aligned} \quad (6.3)$$

In most materials, $n \geq 1$ and the distance between the nodes at optical frequencies (*e.g.*, at $\lambda = 1550$ nm) is on the order of a few hundred nanometers. This distance is below the minimum resolvable distance as predicted by the Rayleigh criterion, and so individual peaks and nodes cannot be detected. However, at the limit where the effective index is small, Eq. 6.3 tells us that this distance grows until the peaks can be individually resolved by free space objectives. By taking a Fourier transform of the infrared image of a standing wave in a low-index medium, we can determine the effective wavelength within the medium, and thus the absolute value of the effective index of the medium. Finally, this method is limited in that there is a maximum effective wavelength that can be measured due to the length of the device within which the standing wave is formed. This determines the minimum effective index that can be reliably measured.

Figure 6.4 shows the analysis done to extract the refractive index from an image of a standing wave. In Fig 6.4a, we have the raw unprocessed infrared image for the device shown in Fig. 6.3. This device is excited from both ends with TE-polarized light at $\lambda = 1585$ nm. A standing wave is clearly visible with two distinct nodes. We take 50 images of this device with a different relative phase between the counter-propagating excitations, and aggregate them to obtain a background image (Fig 6.4b). This background contains no phase information, but will clearly show any defects or scattering points in the device. It will also help calibrate the image against any imbalance in the amplitude of the different excitations. We take the original standing wave image and subtract the background to obtain a unique interference pattern for each of the 50 images (Fig 6.4c). We crop the image around the waveguide and take a 1-dimensional fast Fourier transform along the direction of propagation. This reveals the effective wavelength of the standing wave, and thus the effective refractive index of the waveguide. In Fig 6.4, the standing wave has an effective wavelength of $11.1 \mu\text{m}$, corresponding to an effective index of $n_{\text{eff}} = 0.14$. We fit to the power spectrum, extracting the effective refractive index, as well as a fit error for the index (Fig 6.4d). We apply this process to each of the 50 images taken at every wavelength to obtain a standard error on the measurement.

This measurement and analysis procedure is performed at every wavelength between $1480 - 1680$ nm. Figure 6.5 shows the effective index extracted for a PBG-cladded zero-index waveguide as a function of wavelength. The error bars correspond to 95% confidence intervals that are yielded by the fit. The effective index begins at a positive value and decreases linearly until it reaches the measurement floor,

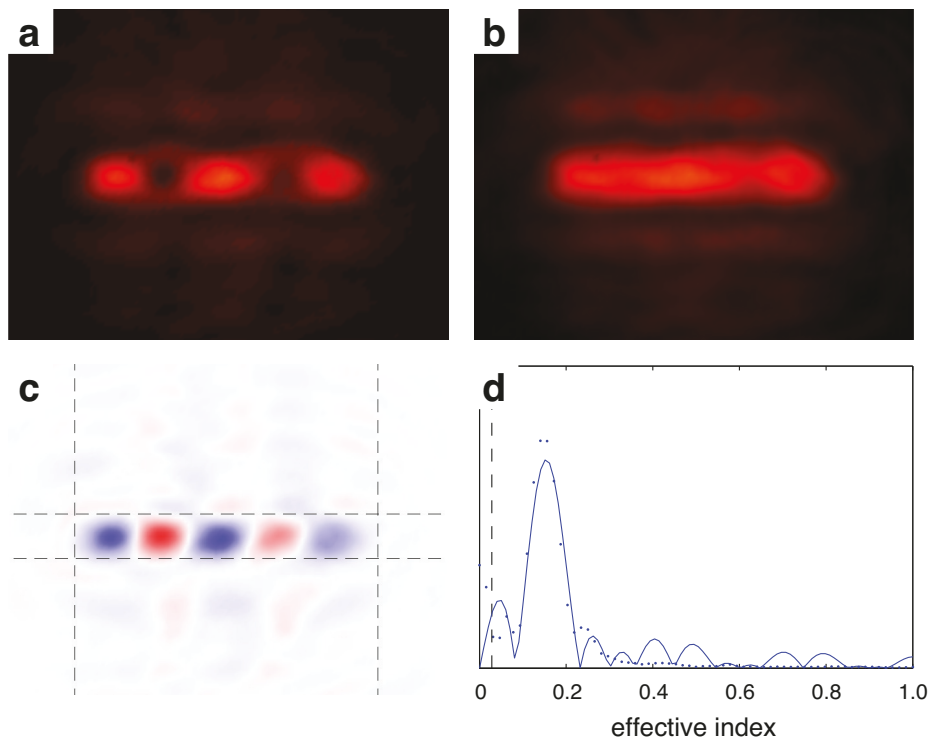


Figure 6.4: **a)** An infrared image of a representative standing wave in a 15- μm -long device, with 2 nodes approximately $5.5 \mu\text{m}$ apart. **b)** By aggregating multiple images with different relative phases, we obtain a background image. **c)** By subtracting the background image from an individual image, we obtain an interference pattern. **d)** A Fourier transform of the interference pattern yields a power spectrum that uncovers the effective index of the device. The dashed black line indicates the measurement floor.

indicated by the black dashed line, at $\lambda = 1618.7$ nm. At even longer wavelengths, the effective index increases linearly again, crossing through the measurement floor at $\lambda = 1635.8$ nm. We interpret the region to the right of the measurement floor to have a negative effective index, based on simulations and the retrieved indices, as shown in Fig. 6.2. This is justified since, as mentioned above, this index extraction method does not discriminate between positive and negative indices. The error increases as the effective index approaches the measurement floor. This is to be expected, as at this point the distance between nodes is larger than the total length of the device. A linear regression places the zero-index wavelength for this device to be at $\lambda = 1627$ nm, within 5% of the design wavelength of $\lambda = 1550$ nm. This small discrepancy is well-explained by fabrication imperfections.

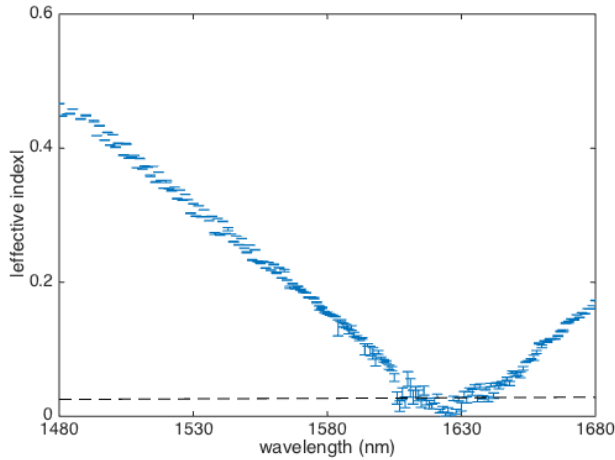


Figure 6.5: The absolute value of the effective refractive index of a 1-channel-wide zero-index waveguide cladded with PBG, achieving an index of zero at $\lambda = 1627$ nm. The error bars correspond to 95% confidence intervals yielded by the fit. The measurement floor is indicated by the black dashed line.

6.3.3 Propagation loss

In order to assess the performance of the PBG, we would like to measure the propagation loss of the two device designs and compare them. We do this by fabricating 2 sets of devices with 5, 10, 15 and 20 unit cells of ZIM, both with and without a PBG. We measure the transmission through all of these devices (Fig. 6.6a-b), a measurement that strictly could not be done with a device in the prism configuration of Section 5.4.2. Similar to what was done in Fig. 6.2d, we fit the transmission as a function of device length and extract a propagation loss (Fig. 6.6c). The PBG-cladded zero-index waveguides statistically outperform the bare zero-index waveguides in almost the entire operation range. At the zero-index wavelength, $\lambda = 1627 \text{ nm}$, the bare waveguide has a propagation loss of $1.26 \text{ dB}/\mu\text{m}$, whereas the PBG-cladded waveguide has a propagation loss of $0.89 \text{ dB}/\mu\text{m}$, a 30% improvement.

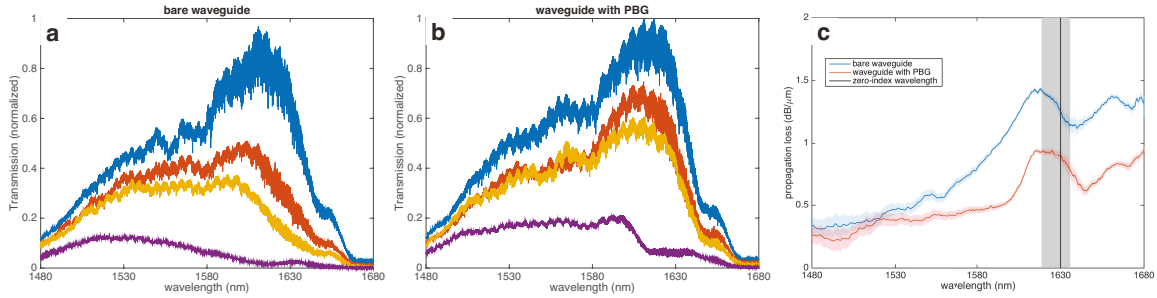


Figure 6.6: **a)** Transmission (normalized) through a bare zero-index waveguide. **b)** Transmission through a PBG-cladded zero-index waveguide. **c)** Extracted propagation loss for bare and PBG-cladded zero-index waveguides. The error bars correspond to the standard error derived from the fit. The region below the measurement floor is shaded in grey, and the zero-index wavelength is indicated by the vertical black line. The PBG reduces the propagation loss by $0.37 \text{ dB}/\mu\text{m}$ at the zero-index wavelength.

6.4 Conclusion

We have theoretically and experimentally demonstrated that a single-unit-cell wide channel of Dirac-cone metamaterial retains its refractive index near zero. Furthermore, we have designed a lower-loss variant of single-channel zero-index waveguides with the integration of photonic-band gap photonic crystals. The addition of PBGs with the correct spacing reduces propagation losses from $1.26 \text{ dB}/\mu\text{m}$ to $0.89 \text{ dB}/\mu\text{m}$, corresponding to a 30% improvement. Simulations suggest that further optimizations could eliminate the in-plane radiation completely, reducing the propagation loss by up to 50% and matching the infinitely periodic structure. The out-of-plane radiation could be reduced by embedding the low- Q dipole mode in a photonic bound state within the continuum [110, 112].

Furthermore, we have demonstrated a new interferometric technique to determine the absolute value of the effective refractive index of a low-index waveguide. This technique does not depend on the shape of the structure, and can be used to characterize low-index devices intended for other applications. Importantly, this experiment constitutes an additional independent proof that our designed metamaterial unambiguously possesses an effective refractive index of zero.

Chapter 7

Towards simultaneous phase matching in zero-index metamaterials

Zero-index metamaterials exhibit unique nonlinear properties. In this chapter, we investigate these properties using full-wave simulations. First, using nonlinear scattering theory, we simulate nonlinear signal generation in 2-dimensional zero-index metamaterials based on a photonic Dirac cone at the Γ point. We observe phase-matching in multiple simultaneous directions, consistent with a refractive index of zero. Using nonlinear finite-difference time-domain simulations, we observe simultaneous phase-matching in the forward- and backward-propagating directions in a realistic 3-dimensional zero-index metamaterial structure. These properties enable a new generation of nonlinear photonic devices with unprecedented flexibility as well as compact device footprints.

7.1 Introduction

7.1.1 Phase matching in nonlinear optics

Nonlinear optics is extremely important to our everyday lives. Nonlinear effects play key roles in fundamental optical phenomena such as quantum squeezing, frequency conversion and entangled photon generation, as well as in optical applications such as lasers, super-resolution microscopy, spectroscopy, and multiphoton lithography [36, 37, 113–124]. In dealing with any nonlinear process, one key obstacle must always be overcome: phase mismatch. Below, I will discuss how zero-index metamaterials can be used to address this challenge and the work that I have done so far demonstrating this.

Phase matching, the wave equivalent to momentum conservation, provides the guidelines that decide which nonlinear interaction will take place. In a photonic chip, satisfying this condition represents a continued obstacle and remains an active area of research. However, when employing any traditional phase-matching techniques such as birefringent phase matching, quasi-phase-matching, waveguide-dispersion engineering or higher-order-mode phase matching, the nonlinear signal is strictly generated in a predefined direction, typically along the direction of propagation (Fig. 7.1) [13, 45, 81, 125–129]. Potential applications of nonlinear optics have been gravely limited by this constraint, especially in photonic integrated circuits where devices are restricted to a plane. There has long been interest in circumventing this restriction to achieve finer control of the nonlinear output [130, 131].

Lately, there has been an increased enthusiasm in expanding the phase-matching

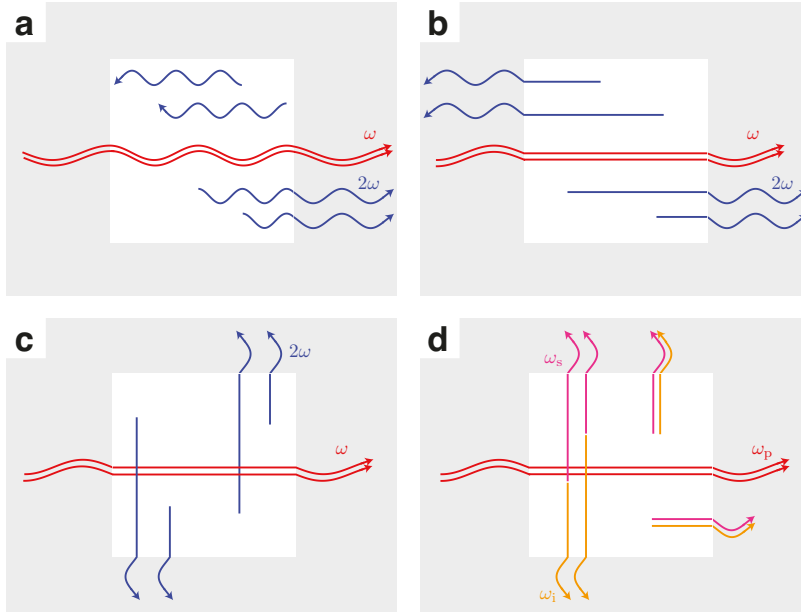


Figure 7.1: **a)** In traditional phase-matching schemes, generated photons are only phase-matched along one propagation direction. Here, pairs of pump photons of frequency ω (red) combine to form photons of frequency 2ω (blue). Photons that are generated traveling in the forward direction are phase-matched and interfere constructively. Those traveling in any other direction interfere destructively and cancel out. **b)** In an anisotropic zero-index material (ZIM), we expect the phase matching to occur in both forward and backward directions. **c)** In an isotropic ZIM, nonlinear processes should be phase-matched in all directions simultaneously. **d)** An easier nonlinear process to demonstrate using photonic Dirac-cones with linear dispersion is four-wave-mixing, where pairs of pump photons combine to form pairs of signal photons ($\omega_p + \omega_p \rightarrow \omega_s + \omega_i$).

toolkit with the use of metamaterials [132–137]. For example, negative-index phase matching, where the generated nonlinear signal propagates in the direction counter to the pump, was demonstrated in plasmonic waveguides [138]. The ultimate manifestation of this principle is zero-index phase matching, where the pump source excites a medium at a wavelength where its refractive index nears zero. The total incoming momentum at this wavelength is zero; thus the total outgoing momentum must necessarily sum up to zero, as well. The physical meaning of this is that no propagation directions are preferred; thus, the generated nonlinear signal is simultaneously phase-matched in all directions. Suchowski *et al.* have demonstrated this simultaneous phase-matching property using a zero-index metamaterial (ZIM) formed of a fishnet structure [34]. This demonstration suffers from two severe limitations, however. First, the length of propagation within the ZIM was only 1600 nm, which is approximately one operating wavelength ($\lambda = 1550$ nm). This distance may be shorter than a coherence length for a poorly phase-matched process. The fabrication procedure for a fishnet process makes achieving an interaction length that is much longer than this impractical. Second, the fishnet metamaterial used in this work is anisotropic and only exhibits a refractive index of zero along the direction of propagation (Fig. 7.1b). In this system, the physics of a multi-directional simultaneously phase-matched material could not be fully explored, once again handicapping potential applications.

The on-chip configuration of the zero-index platform developed in previous chapters allows for device lengths that are not limited by fabrication constraints — it is trivial to fabricate wafer-scale devices on the order of inches [99, 100]. It also enables the exploration of novel nonlinear phenomena.

7.1.2 Simultaneous phase matching in isotropic zero-index media

Within a ZIM, the crystal momentum of photons is identically zero. For this reason, as long as a photon is coupled into a ZIM structure, it contributes to the nonlinear interaction, regardless of its origin. In the ZIM platform we developed, light can be efficiently coupled into or out of the zero-index mode from any side, including from out of the plane of the device (Fig. 7.2b-c).

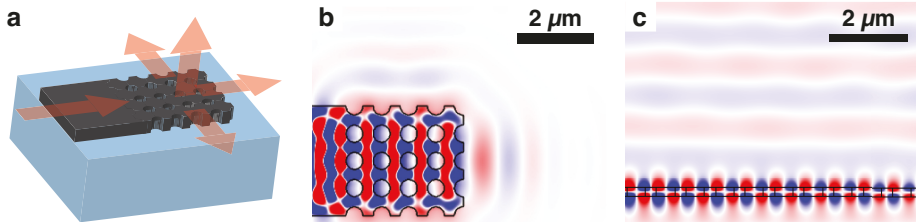


Figure 7.2: A silicon-based zero-index metamaterial coupled to a standard silicon-on-insulator waveguide. **a)** Light incident on the device couples efficiently to all directions. **b)** 3D FDTD simulation of the structure at $\lambda = 1550$ nm, demonstrating in-plane radiation (top view). **c)** Simulation demonstrating radiation normal to the plane of the device (side view).

This effect can be exploited to pumping a device from different directions (Fig. 7.3), something that has yet to be demonstrated in an integrated device. Another characteristic signature of phase matching in a zero-index metamaterial is that each additional unit cell contributes to the phase-matched signal, meaning that the generated signal is proportional to the device area instead of just the total propagation length.

This ZIM platform is uniquely suited to perform tests of these new effects and to perform the first unambiguous demonstration of simultaneous phase matching in multiple directions by studying intrapulse spontaneous four-wave mixing [34] (Fig. 7.1d).

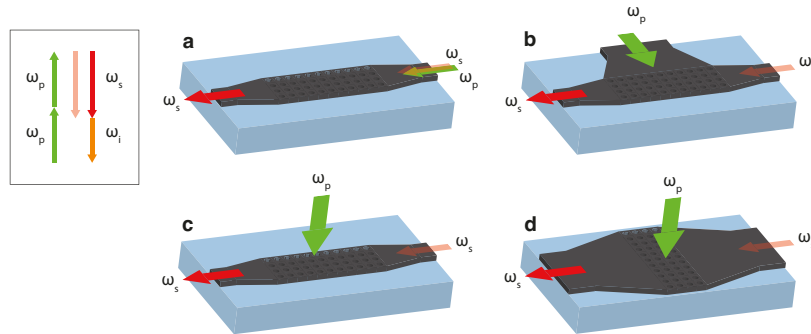


Figure 7.3: Four equivalent phase-matching configurations for four-wave mixing in a zero-index metamaterial. **inset)** Energy diagram illustrating the stimulated $\chi^{(3)}$ process, where two pump fields interact with a weak probe field and amplify it, also producing an idler field (omitted in figures for clarity). **a)** In traditional phase-matching schemes, all interacting fields co-propagate in the nonlinear medium. **b)** By using a zero-index medium, we obtain the additional flexibility to introduce one of the fields from a different direction while still maintaining phase-matching constraints. **c)** This excitation can even come from out-of-the-plane of the device layer. **d)** Since the generated nonlinear signal is proportional to the device area instead of the propagation length, the device can be arbitrarily reconfigured in order to reduce propagation losses or to maximize field overlap.

By changing the length or area of a device, this flexible platform can be used to study the nonlinear behaviour of a zero-index medium when reconfigured into arbitrary shapes for the first time. In this chapter, we will discuss the theory and some preliminary simulation results that probe the question of simultaneous phase matching in integrated photonic Dirac-cone-based ZIMs.

7.2 Theory

7.2.1 Effects of dispersion on phase matching

For the first experimental studies of nonlinear optics, CMOS-compatible Dirac-cone-based zero-index metamaterials can be used to demonstrate spectral broadening, a $\chi^{(3)}$ process controlled by self-phase modulation (SPM), cross-phase modulation (XPM) and four-wave mixing (FWM). In these nonlinear processes, all of the spectral components within a pulse combine to create new spectral components just outside of the spectral bandwidth:

$$\begin{aligned}\omega_p + \omega_p &\rightarrow (\omega_p + \Delta\omega) + (\omega_p - \Delta\omega) \\ &= \omega_s + \omega_i.\end{aligned}$$

In the simple degenerate case above, two photons at the pump frequency ω_p combine to form 2 photons at frequencies shifted by $\pm\Delta\omega$. These new photons are called the signal s and idler i photons by convention. The changes in frequency need to be symmetric in order to conserve energy. Conservation of momentum provides the

following additional constraint:

$$\vec{k}_p + \vec{k}_s \rightarrow \vec{k}_s + \vec{k}_i. \quad (7.1)$$

where \vec{k}_p , \vec{k}_s and \vec{k}_i are the momenta associated with the photons at the frequencies above. The amount by which they differ, $\Delta k = |2\vec{k}_p - \vec{k}_s - \vec{k}_i|$ is called the phase mismatch.

Given these constraints, the amount of spectral broadening provided by the nonlinearity will be due to the sum of contributions from *all* of the $\omega \pm \Delta\omega$ frequency pairs that are also phase-matched. This family of interactions originates from the following nonlinear polarization:

$$\vec{P}_i^{\text{NL}}(\omega - \Delta\omega) = \chi_{ijkl}^{(3)} E_j(\omega) E_k(\omega) E_l^*(\omega + \Delta\omega). \quad (7.2)$$

In the traditional case, all of the beams are collinear, leading to a linear phase-matching condition of

$$\Delta k_L = 2k_p - k_s - k_i. \quad (7.3)$$

For large pump powers or large nonlinearities, an additional amount of nonlinear phase also contributes to the phase mismatch [88, 139]:

$$\Delta k_{\text{NL}} \approx 2\gamma P - \Delta k_L, \quad (7.4)$$

where γ is some effective nonlinearity for the structure and P is the pump power.

The sign of the linear phase mismatch suddenly becomes critical. If perfect linear phase-matching cannot be achieved, but $\Delta k_L > 0$, then any linear mismatch can be compensated by increasing the pump power P . However, if $\Delta k_L < 0$, then a true $\Delta k_{\text{NL}} = 0$ phase-matching condition is unobtainable for any power.

At a given frequency, if $\Delta k_L > 0$, then

$$\begin{aligned} 2k(\omega_p) - k(\omega_i) - k(\omega_s) &> 0 \\ k(\omega_s + \Delta\omega) - k(\omega_s) &> k(\omega_p + \Delta\omega) - k(\omega_p). \end{aligned}$$

where we make use of the definitions of ω_s and ω_i from Eq. 7.1. By dividing both sides by an arbitrarily small $\Delta\omega$ and taking the limit where it vanishes, we obtain

$$\begin{aligned} \lim_{\Delta\omega \rightarrow 0} \frac{k(\omega_s + \Delta\omega) - k(\omega_s)}{\Delta\omega} &> \lim_{\Delta\omega \rightarrow 0} \frac{k(\omega_p + \Delta\omega) - k(\omega_p)}{\Delta\omega} \\ \rightarrow \frac{\partial k(\omega_s)}{\partial \omega} &> \frac{\partial k(\omega_p)}{\partial \omega}. \end{aligned}$$

Repeating this procedure again yields

$$\beta_2 \equiv \frac{\partial^2 k(\omega_p)}{\partial \omega^2} < 0. \quad (7.5)$$

Thus, spectral broadening processes are phase-matched so as long as the structure supports a region where $\beta_2 < 0$. This regime is formally known as the anomalous dispersion regime. For fibers, an equivalent but different definition for the dispersion parameter, called D , is given as

$$D_\lambda = -\frac{2\pi c}{\lambda^2} \frac{\partial^2 k}{\partial \omega^2} [\text{ps/nm/km}]. \quad (7.6)$$

This definition is attractive for fiber optic and photonic integrated circuit applications because of its units: a pulse will spread by approximately D (in ps) per unit bandwidth (in nm) per unit distance travelled (in km). Commercial mode solvers (like Lumerical MODE Solutions) can often directly solve for D .

7.2.2 Coherence length

If a nonlinear process is not phase-matched within a device, there typically still exists a given propagation distance below which this process can still produce a signal. This distance is called the coherence length, and is defined as a function of Δk as

$$L_{\text{coh}} = \frac{\pi}{\Delta k}. \quad (7.7)$$

For this reason, a nonlinear signal can often be detected for very thin films, even for a poorly phase-matched process. Calculating or measuring the coherence length can help establish how severe the phase mismatch is in a process. From Eq. 7.3, we know that the linear phase mismatch for co-propagating light in a four-wave mixing interaction in an ordinary material with a refractive index of n is

$$\begin{aligned} \Delta k_L^{\text{FW}} &= 2k_p - k_s - k_i \\ &= \frac{2\omega_p n_p}{c} - \frac{\omega_s n_s}{c} - \frac{\omega_i n_i}{c} \\ &= \frac{2\omega_p n_p}{c} - \frac{(\omega_p - \Delta\omega)n_s}{c} - \frac{(\omega_p + \Delta\omega)n_i}{c}. \end{aligned}$$

To first order, we set the material to be dispersionless, so that $n = n_p \approx n_i \approx n_s$, which yields

$$\begin{aligned} \Delta k_L^{\text{FW}} &= \frac{1}{c} (2\omega_p n - (\omega_p - \Delta\omega)n - (\omega_p + \Delta\omega)n) \\ &= \frac{1}{c} (2\omega_p n - \omega_p n + \Delta\omega n - \omega_p n - \Delta\omega n) \\ &= 0. \end{aligned}$$

As expected, the fields are phase-matched, corresponding to an infinite coherence length in the forward-propagation direction. As an aside, the addition of dispersion terms typically reduces this length by introducing some correction terms to the

mismatch:

$$\Delta k_L^{\text{FW}} = -\frac{(\Delta\omega)^2}{c} [n'(\omega_p) + \omega_p n''(\omega_p)]. \quad (7.8)$$

These terms explicitly outline the role of dispersion in limiting a nonlinear process such as self-phase modulation, as is discussed in Section 7.2.1. Fortunately, the dispersion profile of a waveguide or other nanophotonic device could however still be tuned quite trivially to achieve perfect phase-matching [140–144].

We can repeat these calculations for any signal photons that are generated in the backward-propagating direction by setting $k_s \rightarrow -k_s$:

$$\begin{aligned} \Delta k_L^{\text{BW}} &= 2k_p - (-k_s) - k_i \\ &= \frac{2\omega_p n}{c} + \frac{(\omega_p - \Delta\omega)n}{c} - \frac{(\omega_p + \Delta\omega)n}{c} \\ &= \frac{1}{c} (2\omega_p n + (\omega_p - \Delta\omega)n - (\omega_p + \Delta\omega)n) \\ &= \frac{2n}{c} (\omega_p - \Delta\omega). \end{aligned}$$

To first order, this means that the coherence length is

$$L_{\text{coh}}^{\text{BW}} = \frac{\pi c}{2n\omega_p}. \quad (7.9)$$

The coherence length for a backward-propagating signal from a nonlinear process is thus inversely proportional to the index of the medium! For $\lambda = 1550$ nm, the coherence length is $L_{\text{coh}} \approx 400$ nm/ n , starting at 400 nm in a vacuum and only getting shorter for ordinary materials. In order to achieve a backward-propagating phase-matched nonlinear signal, a material with an index below 1 is necessary. The typical dispersion correction methods cited earlier simply cannot overcome this limitation, which is why it took 10 years for the first official demonstration of backwards phase matching to materialize [130, 131, 138].

7.2.3 Dispersion profile and related coherence length for zero-index metamaterials

We can use the equations developed in the previous section to estimate the coherence length for the backward-phase-matching nonlinear process in the CMOS-compatible ZIM platform. The dispersion parameter D can be directly calculated from a structure's effective refractive index using Eq. 7.6. In Chapter 5, complex retrieval is performed in FDTD to extract the effective refractive index of the ZIM. This result is reproduced in Fig. 7.4a. In Fig. 7.4b, we show the D parameter that is calculated using this index profile. Throughout most of the operation range, the amount of dispersion is very low, with $|D| < 25 \text{ ps/nm/km}$. Below $\lambda = 1600 \text{ nm}$, D indicates that a waveguide formed of this material will exhibit either anomalous dispersion, or no dispersion at all. Thus, this material has the appropriate dispersion profile to phase-match four-wave mixing processes. In Fig. 7.4c, we plot the coherence length for a pump set at $\lambda = 1550 \text{ nm}$ as a function of one of the signal wavelengths. We see extremely large coherence lengths, confirming this result.

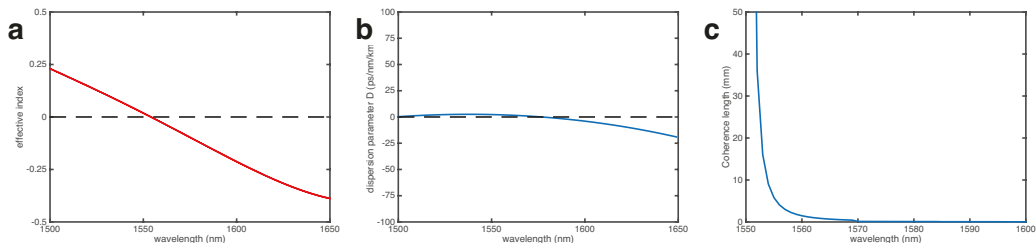


Figure 7.4: **a)** The complex retrieved index of CMOS-compatible ZIM, with linear dispersion and a zero-crossing near $\lambda = 1550 \text{ nm}$. **b)** The D parameter defined in Eq. 7.6, calculated from the index in (a). D shows anomalous dispersion or no dispersion at all for over 100 nm of bandwidth surrounding the zero-index wavelength. **c)** The coherence length is correspondingly large for a pump near this wavelength.

7.3 Simulations

The analytical calculations above all assume propagation in an effective medium. Though this makes for a good first approximation, a more rigorous calculation should include the actual structures we are studying. To do this, we will first use nonlinear scattering theory, as described in Appendix A. We will verify this method by simulating purely bulk (*i.e.*, unstructured) materials and comparing the result of the simulation to the theoretical results obtained above. Following this, we will use nonlinear scattering theory to simulate Dirac-cone metamaterials at their zero-index wavelengths. Following this, we will perform nonlinear finite-difference time-domain (NL-FDTD) simulations of pulses propagating through zero-index waveguides.

7.3.1 Nonlinear scattering theory in bulk materials

According to nonlinear scattering theory, the intensity of the nonlinear signal generated within a medium is proportional to the square of an overlap integral between the nonlinear polarization and a field that originates from the direction of propagation:

$$I_{\text{NL}} \propto \left| \chi^{(3)} \int \vec{E} \cdot \vec{P}_{\text{NL}} dV \right|^2. \quad (7.10)$$

The nonlinear polarization is constructed from pump fields, *e.g.*, for FWM processes we would use Eq. 7.2. We simulate degenerate FWM ($\omega + \omega \rightarrow \omega + \omega$) within bulk materials with dispersionless refractive indices of $n = 2, 1, 0.5$, and 0.01 in Fig. 7.5.

As expected, the coherence lengths for these interactions are infinite for light that is generated in the forward-propagating direction, regardless of the material index. On the other hand, the coherence length increases in the backward-propagating

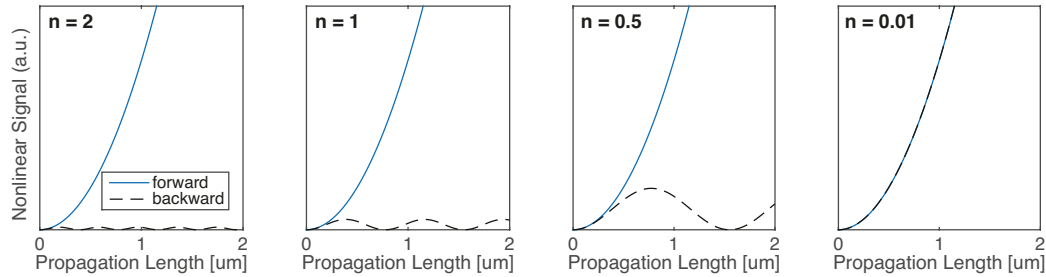


Figure 7.5: Nonlinear signals computed using the nonlinear scattering method for dispersionless bulk media, exhibiting different backward-phase-matching behavior as a function of index. Near $n = 0$, the backward-phase-matched signal and the forward-phase-matched signal overlap.

direction as the index decreases, in good agreement with the predicted value in Eq. 7.9.

7.3.2 Phase-matching in photonic Dirac-cone-based ZIMs

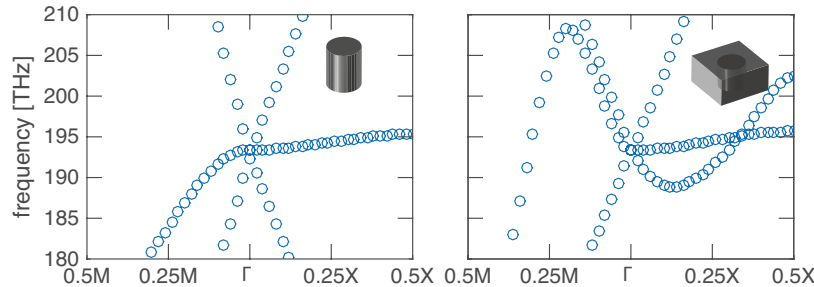


Figure 7.6: The band structures for 2D square arrays of rods (left) and air-holes (right) are designed to exhibit Dirac cones at the center of the Brillouin zone.

Next, we investigate two platforms: a 2D square array of silicon pillars in air (pitch = 845 nm, radius = 171 nm) and a 2D square array of airholes in a silicon bulk (pitch = 583 nm, radius = 182 nm). These metamaterials are designed to exhibit a Dirac cone at the center of their respective Brillouin zones (Fig. 7.6), indicating an effective refractive index of zero. Additionally, being 2-dimensional simulations, they are both free from any radiative losses. Thus, we will use these platforms to build an

intuition for phase matching in photonic Dirac-cone-based ZIMs.

We calculate the nonlinear signal generated in both the rod-based and airhole-based ZIMs as a function of propagation length (Fig. 7.7a-b). We normalize the intensities to the peak intensity along each propagation direction. The generated intensities all grow quadratically in all propagation directions, indicating perfect phase-matching. This result qualitatively resembles the $n = 0.01$ case in Fig. 7.5. Surprisingly, we also observe phase-matching behaviour when increasing the size of the ZIM laterally, orthogonally to the direction of the input pump (Fig. 7.7c).

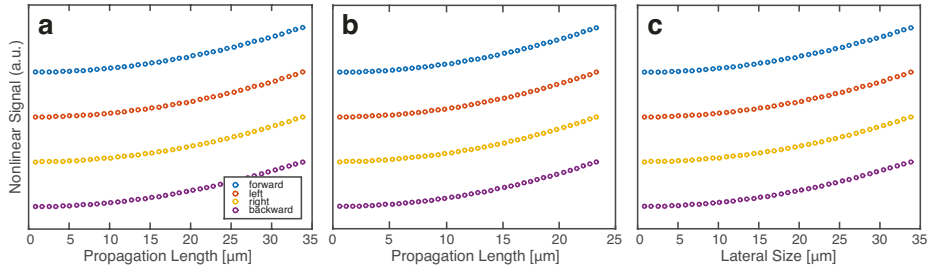


Figure 7.7: Nonlinear signals computed for (a) rod-based and (b) airhole-based ZIMs as a function of propagation length. (c) The nonlinear signal also grows quadratically as the device increases in the orthogonal direction. The intensities are artificially offset for clarity.

7.3.3 Nonlinear finite-difference time-domain simulations

The previous simulations based on nonlinear scattering theory provided us with a confirmation that photonic Dirac-cones can exhibit simultaneous multi-directional phase-matched processes, in agreement with the theoretical predictions. Additionally, they provided another independent confirmation that these metamaterials have an effective refractive index of zero, as they agreed qualitatively with simulations of bulk zero-refractive-index media.

One unavoidable shortcoming of this method is that it is ultimately based on a set of time-harmonic simulations. Thus, certain assumptions are made about the interaction; for example, it assumes that the pump remains undepleted. The nonlinear scattering method is also only capable of modeling interactions between disparate wavelengths, and cannot easily predict the output from an excitation source with a broad spectrum. As we would typically use pulsed sources, and since the ZIM platform is relatively lossy, this model unfortunately cannot accurately model all of the aspects of the nonlinear interaction.

A more powerful method is the nonlinear finite-difference time-domain (NL-FDTD) method, which directly solves the time-dependent nonlinear wave equation for a $\chi^{(3)}$ nonlinearity with very few approximations [145]. Like nonlinear scattering theory, NL-FDTD is capable of including realistic material models and can accurately estimate radiative propagation losses. It also calculates the vector components for both fields at every point in space, a necessary component when taking modal overlap into account in a nonlinear process. Unlike nonlinear scattering theory, NL-FDTD has the capability to specify nearly arbitrary sources, and can monitor the precise powers of outputs instead of just relative powers.

This flexibility comes at a price — NL-FDTD is unfortunately extremely computationally cumbersome. Also, even though we can specify the spectrum of the input source, there exists a limit on the amount of power that can be injected into the simulation before it diverges. These points make this method relatively challenging to apply, limiting the number and types of questions that we could potentially ask.

For the final simulation in this chapter, we propagate ultrafast pulses through

the zero-index waveguides developed in Chapter 6. The observation of a backwards phase-matched signal in the results of this simulation would be the most convincing proof that these effects would be observable in a realistic physical system.

We measure the output from a fiber-based 80-fs pulsed laser source centered at $\lambda = 1550$ nm. This measurement acts as the input source in the simulation. Given realistic coupling and propagation losses, the pulse could achieve a peak power of 7 W at the device; however, in order to avoid numerical divergences, the peak power is set to 1.75 W in the simulation. The linear material parameters (*e.g.*, the complex refractive index) are measured using spectroscopic ellipsometry. We use $\chi^{(3)} = 2.71 \times 10^{-19} \text{ m}^2/\text{V}^2$ as the nonlinear coefficient for silicon [146]. In order to confirm that the generated nonlinear signal originates in the ZIM and not in the waveguide that guides light to it, we set the nonlinearity in the waveguides to zero.

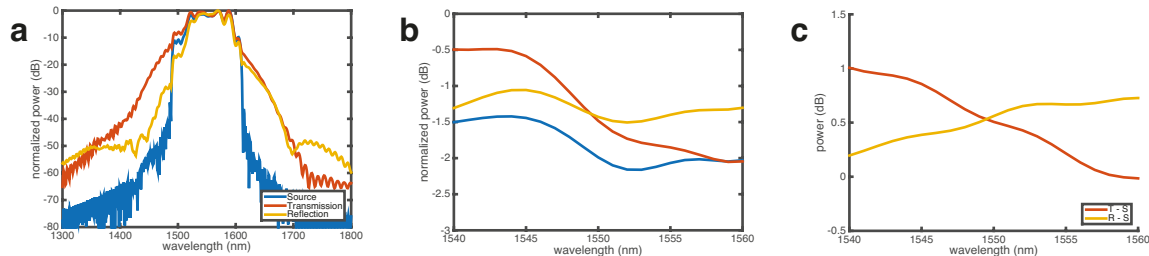


Figure 7.8: Nonlinear finite-difference time-domain simulation of zero-index waveguide. **a)** We excite a zero-index waveguide with an 80-fs source. Both the reflected and transmitted outputs are spectrally broadened. **b)** Same as (a) zoomed into a 20 nm bandwidth surrounding the zero-index wavelength. Photons generated at longer wavelengths preferentially propagate backwards, indicating backward-phase-matching. **c)** Same as (b), normalized to the source.

We excite 5 unit cells of the zero-index waveguide structure from Section 6.2.1 in Chapter 6. We collect both the transmitted and reflected signals for a broad bandwidth, ranging from $\lambda = 1300$ nm to 1800 nm. All of the pulses are normalized

to their peaks values to neglect any linear propagation loss (Fig. 7.8a). We observe significant broadening of the pulse in both the transmitted and reflected signals when compared to the input source, corresponding to a nonlinear interaction. Secondly, we note that the spectrum of the transmission pulse is different from that of the reflected pulse. This indicates that we have different phase-matching behaviour along the different propagation directions, and that the reflected signal is *not* a purely linear reflection of the forward-propagating phase-matched signal.

A closer look around the zero-index wavelength at $\lambda = 1550$ nm reveals that the transmitted intensity is relatively stronger at shorter wavelengths, whereas the reflected intensity is larger above the zero-index wavelength (Fig. 7.8b). The crossover point between these two regimes happens precisely at the structure's zero-index wavelength, at $\lambda = 1550$ nm. Normalizing the two outputs to the source makes this trend even more obvious (Fig. 7.8c). This agrees with our intuition: a pair of photons at $\omega_0 = 2\pi c/(1550 \text{ nm})$ combine to generate two photons at $\omega_0 \pm \Delta\omega$ for some small $\Delta\omega$. The “positive-index photons” that are generated at shorter wavelengths (higher frequencies) are phase-matched in the forward-propagating direction. Meanwhile, the “negative-index photons” at longer wavelengths (lower frequencies) are simultaneously phase-matched in the backward-propagating direction. This is convincing proof that simultaneous multi-directional phase-matching can be experimentally achieved on-chip, in the presence of large realistic losses and dispersion. We expect this effect to be even more pronounced for larger powers, which are achievable given the sources available.

7.4 Conclusion

We have studied the phase-matching characteristics of dispersionless bulk zero-index media, lossless photonic Dirac-cone metamaterials and realistic 3D Dirac-cone metamaterials using multiple analytic and numeric methods. We have derived that a zero or negative index material is necessary to achieve backward-phase-matching in four-wave mixing processes. We have found that photonic Dirac-cone-metamaterial platforms are in fact capable of simultaneously generating phase-matched signals in all directions. We have also observed the surprising property that the generated nonlinear signal in a zero-index medium is proportional to the device area instead of the propagation length. Thus, this phase-matched signal generation is independent of shape, ZIM size, and excitation direction. These properties enable a new generation of nonlinear photonic devices with unprecedented flexibility as well as compact device footprints. The ability to tune the phase-matched direction opens opportunities for remote sensing and for integrated lasing.

Chapter 8

Summary and outlook

In this final chapter, we will outline the major conclusions drawn from the individual chapters and will present further research directions based on the work developed in this dissertation.

In Chapter 2, we develop a controlled and reliable procedure for the fabrication of TiO₂ nanophotonic devices. This procedure uses scalable CMOS-compatible fabrication processes and can be used to structure a multitude of integrated photonic components such as photonic crystals and resonators. In the case of polycrystalline anatase, we have shown that this procedure has allowed us to achieve propagation losses that near the film propagation loss (0.40 dB/mm). This value compares favourably to early results using polycrystalline silicon [68]. It is low enough to observe some nonlinear processes, such as low-threshold harmonic generation. However, improvements are necessary to demonstrate more exciting on-chip applications, such as frequency combs or nonlinear interferometers [80, 81]. The primary contribution to propagation losses in our thin films come from the nanocrystal structure of which

the film is composed. Thus emerges a clear research direction — developing smoother TiO₂ substrates with intrinsically lower losses. Single-crystal rutile TiO₂, which is lattice matched to MgF₂, has recently been epitaxially grown with high optical quality [147]. There has also been promising work reported by the researchers at the University of Eastern Finland on low-loss TiO₂ thin films deposited using atomic layer deposition [54, 148, 149]. Beyond the exploration of different substrates, the etch recipe could be further optimized to obtain smoother etch profiles and vertical sidewalls, as has been demonstrated in other material platforms [79, 150, 151].

In Chapter 3, we use the fabrication process outlined in Chapter 2 to demonstrate ring resonators in polycrystalline anatase with large loaded quality factors up to $Q \approx 2.5 \times 10^4$ and propagation losses as low as 0.40 dB/mm. The deposition of polycrystalline anatase is substrate-independent by nature, allowing for easy vertical integration. We used these resonators to extract the thermo-optic coefficient for anatase and found it to be negative, in general agreement with literature values for TiO₂ [19, 57]. By combining TiO₂ with a SiO₂ cladding, this effect could be used to design temperature-insensitive photonic devices. To the best of our knowledge, this is the first and only material platform with a demonstrated large nonlinearity to possess this unique combination of properties, enabling compact, device-dense athermal nonlinear devices.

During our study of anatase rings, we observed characteristic asymmetries in the resonances. In Chapter 4, we treat these asymmetries more quantitatively and recreate them using full-wave simulations. We concluded that these asymmetries were linear in origin and were due to coherently scattered reflections within the waveguide

caused by fabrication imperfections. We derived a new asymmetric transfer function for ring resonators in the presence of reflections. This transfer function can be used reliably to extract propagation losses for a thorough fabrication characterization. We show that this model outperforms the typical symmetric transfer function at extracting parameters from realistic fabricated devices. It also predicts a threshold value for reflections above which asymmetries appear more pronounced. In a theoretical sense, the theory of coupled cavities is already well known. However, this particular implementation points to a common origin for these effects that could be surprising to experimentalists.

The second half of the thesis, starting with Chapter 5, is based on a new CMOS-compatible platform for obtaining an effective refractive index near zero on an integrated photonic chip. This platform consists of a square array of air columns in a 220-nm thick silicon thin film and is based on photonic-Dirac cones at the center of the Brillouin zone formed from the degeneracy of a quadrupole mode and two dipole modes. We experimentally measure the refractive index of a prism composed of this metamaterial and unambiguously demonstrate that it has a refractive index near zero. This marks the first demonstration of an all-dielectric, monolithic zero-index platform with a low profile of only 220 nm. As a consequence, it features intrinsic compatibility with all the devices that have been demonstrated using the SOI platform and can be trivially fabricated simultaneously with established components such as single-mode waveguides, resonators, photonic crystal waveguides, *etc.* This evolutionary step finally enables the widespread industrial adoption of integrated zero-index metamaterials. The teachings provided in this chapter can also be used to develop

zero-index metamaterials based on other platforms with desirable material properties, such as using TiO_2 for its transparency window, nonlinear properties and negative thermo-optic coefficient [15, 53, 61], LiNbO_3 for its large $\chi^{(2)}$ nonlinearity [126, 152] or diamond for its mechanical properties [153, 154] and wealth of color centers [155–157].

Chapter 6 focuses on a particular embodiment of this metamaterial, arranging it along a single propagating dimension and forming a waveguide. Devices with this geometry are better-suited towards applications that require high coupling efficiencies and high peak intensities. We measured the effective index of the waveguide using a new on-chip interferometry technique that does not necessitate the use of additional interferometry structures or equipment. This method allows us to image a standing wave with an effective wavelength twice the length of the structure ($\lambda_{\text{eff}} > 30 \mu\text{m}$). By integrating this waveguide with silicon-based photonic band gap materials, we experimentally demonstrate a reduction in the propagation loss by up to 30%. The photonic band gap restricts lossy radiation in-plane; however, total propagation losses remain prohibitively high ($\approx 1 \text{ dB}/\mu\text{m}$) due to poor confinement in the out-of-plane direction. These losses could be mitigated in whole at the zero-index frequency by embedding the low- Q dipole mode in a photonic bound state within the continuum [110]. Current theoretical work shows promising results with respect to achieving reasonable propagation losses ($\approx 10 \text{ dB/cm}$) in Dirac cone metamaterials [112]; unfortunately, so far, these proposed designs also suffer from considerable sensitivity to fabrication parameters. Designing a fabrication-imperfection-tolerant lossless zero-index metamaterial would represent the final significant step forward in making zero-index materials valuable to the broader photonics community.

Finally, we discuss the application of zero-index metamaterials in fundamental nonlinear optical phenomena in Chapter 7. We provide a brief theoretical background on backward phase-matching in bulk media and numerically explore this effect using full wave simulations. We find that an isotropic refractive index near zero enables some surprising results with regards to phase matching. First, nonlinear signals can be generated in multiple directions simultaneously. Second, the pump beam can be equivalently used to excite the medium from multiple directions. Finally, the magnitude of the generated signal becomes proportional to the area of the nonlinear medium instead of just the propagation length. We propose to verify these points experimentally using the zero-index waveguides developed in previous chapters. Using nonlinear full wave simulations, we demonstrate that these effects are observable in this type of device, despite the presence of realistic losses and dispersion. This result helps to decouple the structure of an integrated device from its phase-matching properties. Using a zero-index medium, a nonlinear devices can be reorganized as befits the application, *e.g.*, to reduce the device's footprint, to reduce propagation loss or to increase the overlap between different modes. Integrated nonlinear devices formed of a zero-index medium can even be pumped from out-of-plane, avoiding problematic effects such as waveguide dispersion or coupling inefficiencies. Together, these benefits have the potential to dramatically simplify nonlinear devices, making them more flexible and drastically reducing their footprint.

Appendix A

Nonlinear scattering theory

A.1 Introduction

Nonlinear scattering theory is a powerful theoretical tool that can be used to predict the nonlinear emission of an arbitrary nanostructure. It is capable of making predictions in times when analytic solutions are challenging or elusive to obtain. This theory does not depend on the slowly varying envelope approximation, does not employ perturbation theory and does not generate pulse propagation equations or coupled equations of any kind (like the derivation in Agrawal's *Nonlinear Fiber Optics* [158]). It is an alternative way of solving the nonlinear wave equation under the undepleted pump approximation (*i.e.*, the nonlinear polarization is much smaller than the linear polarization at all times) that is based on Lorentz reciprocity. For this reason it works under all of the conditions that Lorentz reciprocity does: ϵ and μ may be complex and anisotropic, but must be symmetric (*i.e.*, no magneto-optic materials).

The following chapter closely follows the derivations originally performed by

O'Brien *et. al* from Zhang's group at Berkeley [44]. I have added some intermediate steps where they were skipped, so this document is even more comprehensive. First, we will derive Lorentz reciprocity, and we will use it to describe nonlinear scattering theory. We will apply Lorentz reciprocity to a pair of simple test cases (*e.g.*, a dipole source and a plane wave). Finally, most instructively, we will use nonlinear scattering theory to derive the second harmonic signal generated by a powerful pump propagating along 1 dimension and we will compare this result to other analytic and numerical solutions. The point is to gain an understanding of both how and why the theory works, and to learn how to apply it to our own structures.

A.2 Solution to the inhomogeneous wave equation with a source current

We begin with the electromagnetic inhomogeneous wave equation:

$$\vec{\nabla}^2 \vec{E} - \frac{1}{c^2} \frac{\partial^2 \vec{E}}{\partial t^2} = \mu_0 \frac{\partial \vec{J}}{\partial t}. \quad (\text{A.1})$$

This equation describes the waves \vec{E} that are driven by a changing source current \vec{J} . The simplest case of a source is an oscillating dipole (*e.g.*, a Hertzian dipole of length Δl and current I_0 yields a source of $\vec{J} = I_0 \Delta l e^{-i\omega t} \hat{j}$).

Alternatively, we can write Eq. A.1 in terms of a magnetic vector potential \vec{A} using the Lorenz gauge (chosen to satisfy $\vec{\nabla} \cdot \vec{A} + \frac{1}{c^2} \frac{\partial^2 \phi}{\partial t^2} = 0$, yielding $\vec{E} = -\vec{\nabla} \phi - \frac{\partial \vec{A}}{\partial t}$) to eliminate the time derivative in the source term:

$$\vec{\nabla}^2 \vec{A} - \frac{1}{c^2} \frac{\partial^2 \vec{A}}{\partial t^2} = \mu_0 \vec{J}.$$

This formulation is preferred because there exists an analytic equation for \vec{A} for any given current density \vec{J} . As long as the potential goes to zero as we approach infinity, the vector potential driven by \vec{J} within a volume V' is obtained using Green's theorem:

$$\vec{A}(\vec{r}, t) = \frac{\mu_0}{4\pi} \int_V \frac{\vec{J}(\vec{r}', t') e^{ik|\vec{r}-\vec{r}'|}}{|\vec{r}-\vec{r}'|} dV',$$

where t' is the retarded time $t' = t - |\vec{r}-\vec{r}'|/c$. \vec{E} is then obtained by applying a time derivative to \vec{A} .

A.3 Lorentz reciprocity theorem

Equation A.1 can be written in time-harmonic form (where $\partial/\partial t \rightarrow -iw$) as

$$\vec{\nabla}^2 \vec{E} + \frac{\omega^2}{c^2} \vec{E} = -i\mu_0 \omega \vec{J}.$$

In this form, we can define a new Hermitian operator \hat{O} that we use to relate \vec{E} to \vec{J} :

$$\hat{O} \equiv \frac{i}{\mu_0 \omega} \left(\vec{\nabla}^2 + \frac{\omega^2}{c^2} \right),$$

such that

$$\hat{O} \vec{E} = \vec{J}.$$

For a pair of commutable vector fields \vec{F} and \vec{G} , we can define an inner product (\vec{F}, \vec{G}) to be

$$\begin{aligned} (\vec{F}, \vec{G}) &\equiv \int \vec{F} \cdot \vec{G} dV \\ &= \int \vec{G} \cdot \vec{F} dV = (\vec{G}, \vec{F}). \end{aligned}$$

Because the operator \hat{O} is Hermitian, $(\hat{O}\vec{F}, \vec{G}) = (\vec{F}, \hat{O}\vec{G})$ under the inner product in Eq. A.2 since

$$\begin{aligned} (\hat{O}\vec{F}, \vec{G}) &\equiv \int (\hat{O}\vec{F}) \cdot \vec{G} dV \\ &= \int \vec{G} \cdot (\hat{O}\vec{F}) dV \\ &= \int (\vec{G}\hat{O}) \cdot \vec{F} dV \\ &= \int \vec{F} \cdot (\hat{O}\vec{G}) dV \\ &= (\vec{F}, \hat{O}\vec{G}). \end{aligned} \quad (\text{A.2})$$

You can quickly convince yourself that this proof is valid — it obviously works for the linear part of the operator that is proportional to ω^2 , and the second half of the operator is analogous to the momentum operator in quantum mechanics.

Because of this property, we obtain a striking result. First, we need a pair of sources \vec{J}_1 and \vec{J}_2 that create a pair of corresponding fields $\hat{O}\vec{E}_1 = \vec{J}_1$ and $\hat{O}\vec{E}_2 = \vec{J}_2$.

We take the inner product of one field with the other current, which yields

$$\begin{aligned} (\vec{E}_1, \vec{J}_2) &= (\vec{E}_1, \hat{O}\vec{E}_2) \\ &= (\hat{O}\vec{E}_1, \vec{E}_2) \\ &= (\vec{J}_1, \vec{E}_2). \end{aligned}$$

This is called Lorentz's reciprocity theorem:

$$\begin{aligned} (\vec{E}_1, \vec{J}_2) &= (\vec{E}_2, \vec{J}_1) \\ \implies \int \vec{E}_1 \cdot \vec{J}_2 dV &= \int \vec{E}_2 \cdot \vec{J}_1 dV. \end{aligned} \quad (\text{A.3})$$

It is a little difficult to directly interpret what the result in Eq. A.3 means. In order to make use of it, one needs to know the composition of some source $\vec{J}_1(\vec{r}_1)$ at

a location \vec{r}_1 and its field distribution $\vec{E}_1(\vec{r}_2)$ at a different location \vec{r}_2 . Given this knowledge, the theorem can be used to determine the field \vec{E}_2 at \vec{r}_1 (the location of the original source) that is generated by any arbitrary source $\vec{J}_2(\vec{r}_2)$ located at \vec{r}_2 . We will evaluate this theorem more closely in the following sections by studying a pair of simple examples.

A.4 Example 1: A Hertzian dipole source

For our first concrete example, the current source \vec{J}_2 comprises a Hertzian dipole at \vec{r}_2 with a current I_0 and a length Δl , oscillating at a frequency ω :

$$\vec{J}_2(\vec{r}, \omega) = I_0 \Delta l \delta^3(\vec{r} - \vec{r}_2) e^{-i\omega t} \hat{j}. \quad (\text{A.4})$$

Without loss of generality, we align the dipole along the direction \hat{j} . The field that it emits \vec{E}_2 is calculated using Eq. A.2 to be:

$$\vec{E}_2(\vec{r}, \omega) = -\frac{i\omega\mu I_0 \Delta l}{4\pi |\vec{r} - \vec{r}_2|} e^{-i(\omega t - k|\vec{r} - \vec{r}_2|)} \hat{j}. \quad (\text{A.5})$$

Now, both \vec{J}_2 and \vec{E}_2 , which originate at \vec{r}_2 , are known at every point \vec{r} .

Suppose we have an arbitrary scatterer (*e.g.*, a nonlinear scatterer) at some different location \vec{r}_1 . When excited, this scatterer creates a current \vec{J}_1 which generates some unknown nonlinear fields. This current source is created by a changing nonlinear polarization \vec{P}^{NL} :

$$\begin{aligned} \vec{J}_1(\vec{r}, \omega) &= \frac{\partial \vec{P}^{\text{NL}}(\vec{r}, \omega)}{\partial t} \\ &= -i\omega \vec{P}^{NL}(\vec{r}, \omega). \end{aligned} \quad (\text{A.6})$$

\vec{P}^{NL} depends on the nonlinear process of interest. For example, \vec{P}^{NL} could represent second harmonic generation (SHG), where 2 fields of frequency ω combine to excite a polarization of frequency 2ω :

$$\begin{aligned}\vec{P}_x^{\text{NL}}(2\omega) &= \epsilon_0 \chi_{xjk}^{(2)} E_j(\omega) E_k(\omega) \hat{i} \\ &= \epsilon_0 \chi^{(2)} \left(E_0 e^{-i(\omega t - \vec{k}(\omega) \cdot \vec{r})} + E_0 e^{i(\vec{k}(\omega) \cdot \vec{r} - \omega t)} \right) \left(E_0 e^{-i(\omega t - \vec{k}(\omega) \cdot \vec{r})} + E_0 e^{i(\omega t - \vec{k}(\omega) \cdot \vec{r})} \right) \hat{i} \\ &= \epsilon_0 \chi^{(2)} E_0^2 e^{-i((2\omega)t - 2\vec{k}(\omega) \cdot \vec{r})} + \text{c.c.}\end{aligned}\quad (\text{A.7})$$

We neglect the complex conjugate terms at the end, and choose to just take the ‘real’ part of the solution at the final step.

At this point, \vec{J}_1 , \vec{J}_2 and \vec{E}_2 are all known at every point in space. We use Eq. A.3 to obtain \vec{E}_1 :

$$\begin{aligned}\int \vec{E}_1 \cdot \vec{J}_2 dV &= \int \vec{E}_2 \cdot \vec{J}_1 dV \\ \int \vec{E}_1 \cdot \left(I_0 \Delta l \delta^3(\vec{r} - \vec{r}_2) e^{-i\omega t} \hat{j} \right) dV &= - \int \vec{E}_2 \cdot i\omega \vec{P}^{\text{NL}} dV \\ (I_0 \Delta l e^{-i\omega t}) \vec{E}_1(\vec{r}_2, \omega) \cdot \hat{j} &= -i\omega \int \vec{E}_2 \cdot \vec{P}^{\text{NL}} dV \\ \implies \vec{E}_1(\vec{r}_2, \omega) \cdot \hat{j} &= -\frac{i\omega e^{i\omega t}}{I_0 \Delta l} \int \vec{E}_2 \cdot \vec{P}^{\text{NL}} dV.\end{aligned}\quad (\text{A.8})$$

The relevant part of Eq. A.8 states that

$$\vec{E}_{\text{nonlinear}}(\vec{r}_{\text{dipole location}}) \cdot \hat{j} \propto \int \vec{E}_{\text{dipole}} \cdot \vec{P}^{\text{NL}} dV,$$

that is, at an arbitrary point \vec{r} , the detectable field \vec{E} that is generated by a nonlinear polarization \vec{P}^{NL} is proportional to the overlap of \vec{P}^{NL} with the field that is created by an imaginary dipole placed at \vec{r} . As we will show in the following section, this result from Eq. A.8 can be expanded to any arbitrary source \vec{E} at any location \vec{r} , and not just a dipole source.

A.5 Example 2: A plane wave source

In a practical experiment, structures will be excited by plane waves. From a distance, this is what a dipole source will look like, anyway. We begin by inserting the fields created by a dipole (Eq. A.5) into Eq. A.8:

$$\begin{aligned}\vec{E}_1(\vec{r}_2) \cdot \hat{j} &= -\frac{i\omega e^{i\omega t}}{I_0 \Delta l} \int \vec{E}_2 \cdot \vec{P}^{\text{NL}}(\vec{r}) dV \\ &= -\frac{\omega^2 \mu}{4\pi} \int \frac{e^{ik|\vec{r}-\vec{r}_2|}}{|\vec{r}-\vec{r}_2|} (\vec{P}^{\text{NL}}(\vec{r}) \cdot \hat{j}) dV.\end{aligned}$$

This is true for any direction \hat{j} , so

$$\vec{E}_1(\vec{r}_2) = -\frac{\omega^2 \mu}{4\pi} \int \frac{e^{ik|\vec{r}-\vec{r}_2|}}{|\vec{r}-\vec{r}_2|} \vec{P}^{\text{NL}}(\vec{r}) dV. \quad (\text{A.9})$$

We define $r \equiv |\vec{r} - \vec{r}_2| \approx |\vec{r}_2|$, the distance between the location of interest (*e.g.*, the location of the detector) and the nanostructure. We would typically excite a nanostructure using a plane wave that originates very far away, which justifies this approximation. We also define a field $\vec{E} \equiv |E_0|e^{-i(\omega t - kr)}$, which comprises a plane wave of magnitude E_0 . Together, these definitions simplify Eq. A.9 to

$$\vec{E}_{\text{NL}}(\vec{r}) = -\frac{\omega^2 \mu e^{i\omega t}}{4\pi r} \int \vec{P}^{\text{NL}} \cdot \frac{\vec{E}}{|E_0|} dV. \quad (\text{A.10})$$

Equation A.10 is actually the only equation that is printed in the main text of Ref. [44]. It is the only equation that needs to be applied when using the nonlinear scattering theory method.

Below is the prescription with which this method can be used to numerically estimate the nonlinearities of an arbitrary structure:

1. The structure is excited with a plane wave at the pump frequencies ω_p that form the nonlinear polarization. This leads to a time-harmonic field distribution

$\vec{E}(\omega_p)$ within the nanostructure. Those distributions are used to create $\vec{P}^{\text{NL}}(\omega_s)$ using, for example, Eq. A.7.

2. In a separate simulation, the structure is excited with a plane wave that originates ‘from the detector’ at the generated signal frequency ω_s . This leads to a second time-harmonic field distribution $\vec{E}_2(\omega_s)$ within the nanostructure.
3. The generated nonlinear field is proportional to the integral over the nonlinear medium of the overlap of these two fields, as described in Eq. A.10.

The recipe above somewhat elucidates what is contained within Eq. A.10. First, the pump fields excite the structure and combine within it to form a nonlinear polarization. Next, this oscillating nonlinear polarization radiates a nonlinear signal. The part of the nonlinear signal that can be detected is the part that most resembles a mode originating from the detector. This third line is encompassed in the overlap integral in Eq. A.10 and is perhaps the most nuanced part of the theorem. Intuitively, a propagating mode that perfectly excites the detector would overlap perfectly with a mode that originates from the detector — akin to reversing the arrow of time.

A.6 Second Harmonic Generation in a 1D nonlinear medium

Still following O’Brien’s manuscript, we study second harmonic generation propagating along the \vec{z} -axis in a 1-dimensional nonlinear medium with the $\vec{P}_x^{\text{NL}}(2\omega)$ derived

in Eq. A.7:

$$\vec{P}_x^{\text{NL}}(z, 2\omega) = \epsilon_0 \chi^{(2)} E_0^2 e^{i(2k(\omega)z - (2\omega)t)} \hat{i}. \quad (\text{A.11})$$

This nonlinear polarization acts as a source \vec{J}_1 :

$$\vec{J}_1(z, 2\omega) = i\omega \epsilon_0 \chi^{(2)} E_0^2 e^{i(2k(\omega)z - (2\omega)t)} \hat{i}. \quad (\text{A.12})$$

We place a detector at $\vec{r}_2 = z_2$. In order to estimate the generated fields at this location, we place a Hertzian dipole source $\vec{J}_2(2\omega)$ from Eq. A.4 at this location and make use of the derivations in section A.4:

$$\begin{aligned} \vec{J}_2(z, 2\omega) &= I_0 \Delta l \delta(z - z_2) e^{-i2\omega t} \hat{i} \\ \implies \vec{E}_2(z, 2\omega) &= \frac{2\omega \mu I_0 \Delta l}{2k(2\omega)} e^{-i(2\omega t - k(2\omega)|z - z_2|)} \hat{i}. \end{aligned}$$

Without loss of generality, we assume the detector dipole source is on the right hand side at $z_2 = L > z$ and so $|z - z_2| \rightarrow (L - z)$. Thus, the detector fields are moving to the left:

$$\vec{E}_2(z, 2\omega) = \frac{2\omega \mu I_0 \Delta l e^{ik(2\omega)L}}{2k(2\omega)} e^{-i(2\omega t + k(2\omega)z)} \hat{i}.$$

This means that the 1D equivalent to Eq. A.10 is

$$\vec{E}_1(\vec{r}_2, 2\omega) \cdot \hat{i} = \frac{i2\omega e^{i2\omega t}}{I_0 \Delta l} \int \vec{E}_2 \cdot \vec{P}^{\text{NL}} dz.$$

Inserting \vec{E}_2 and \vec{P}^{NL} yields

$$\begin{aligned} \vec{E}_1(\vec{r}_2, 2\omega) \cdot \hat{i} &= \frac{i2\omega e^{i2\omega t}}{I_0 \Delta l} \int \frac{2\omega \mu I_0 \Delta l e^{ik(2\omega)L}}{2k(2\omega)} e^{-i(2\omega t + k(2\omega)z)} \cdot \epsilon_0 \chi^{(2)} E_0^2 e^{i(2k(\omega)z - (2\omega)t)} dz \\ &= \frac{i2\omega^2 \mu \epsilon_0 \chi^{(2)} E_0^2}{k(2\omega)} e^{ik(2\omega)L} e^{-i2\omega t} \int_0^L e^{i(k(2\omega)z - 2k(\omega)z)} dz. \end{aligned}$$

The left-hand term is the overall magnitude of the generated nonlinear field and the integral defines the usual phase-matching term that is obtained when solving the

nonlinear wave equation, with the usual phase-mismatch $\Delta k \equiv k(2\omega) - 2k(\omega)$. Importantly, this derivation demonstrates that phase-matching is *built into* this method!

O'Brien *et. al* compare this solution to the solution of the wave equation and find excellent agreement:

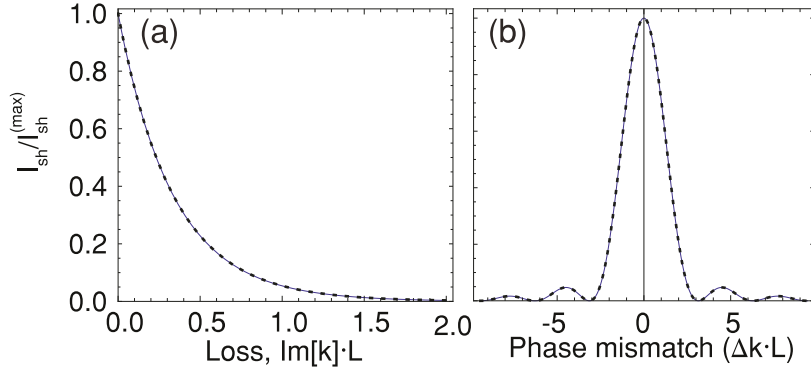


Figure A.1: **a)** Second harmonic intensity as a function of material loss, calculated from nonlinear scattering theory (blue) and a direct solution of the nonlinear wave equation (black dashed). **b)** Second harmonic intensity as a function of phase mismatch, calculated from nonlinear scattering theory (blue) and a direct solution of the nonlinear wave equation (black dashed). The nonlinear scattering theory calculations are in agreement with the direct solution of the nonlinear wave equation (from Ref. [44]).

Bibliography

- [1] K. C. Kao and G. A. Hockham. Dielectric-fibre surface waveguides for optical frequencies. *Proceedings of the Institution of Electrical Engineers*, 113(7):1151, 1966.
- [2] K. Nagayama, M. Kakui, M. Matsui, T. Saitoh, and Y. Chigusa. Ultra-low-loss (0.1484 dB/km) pure silica core fibre and extension of transmission distance. *Electronics Letters*, 38(20):1168–1169, 2002.
- [3] Robert W. Keyes. Optical logic - in the light of computer technology. *Journal of Modern Optics*, 32(5):525–535, 1985.
- [4] H. John Caulfield, Chandra S. Vikram, and Andrey Zavalin. Optical logic redux. *Optik*, 117(5):199–209, 2006.
- [5] David A. B. Miller. Are optical transistors the logical next step? *Nature Photonics*, 4(1):3–5, jan 2010.
- [6] Yoshihiro Akahane, Takashi Asano, Bong-shik Song, and Susumu Noda. High-Q photonic nanocavity in a two-dimensional photonic crystal. *Nature*, 425(October):944, 2003.
- [7] Jacob S. Levy, Alexander Gondarenko, Mark A. Foster, Amy C. Turner-Foster, Alexander L. Gaeta, and Michal Lipson. CMOS-compatible multiple-wavelength oscillator for on-chip optical interconnects. *Nature Photonics*, 4(1):37–40, jan 2010.
- [8] Carlos Ríos, Matthias Stegmaier, Peiman Hosseini, Di Wang, Torsten Scherer, C. David Wright, Harish Bhaskaran, and Wolfram H. P. Pernice. Integrated all-photonics non-volatile multi-level memory. *Nature Photonics*, 9(11):725–732, sep 2015.
- [9] Michal Lipson. Guiding, modulating, and emitting light on silicon - challenges and opportunities. *Journal of Lightwave Technology*, 23(12):4222–4238, 2005.
- [10] Bahram Jalali and Sasan Fathpour. Silicon photonics. *Journal of Lightwave Technology*, 24(12):4600–4615, 2006.

- [11] Richard Soref. The past, present, and future of silicon photonics. *IEEE Journal of Selected Topics in Quantum Electronics*, 12(6):1678–1687, 2006.
- [12] Tom Baehr-Jones, Thierry Pinguet, Patrick Lo Guo-Qiang, Steven Danziger, Dennis Prather, and Michael Hochberg. Myths and rumours of silicon photonics. *Nature Photonics*, 6(4):206–208, mar 2012.
- [13] J. Leuthold, C. Koos, and W. Freude. Nonlinear silicon photonics. *Nature Photonics*, 4:535–544, 2010.
- [14] M. Landmann, E. Rauls, and W. G. Schmidt. The electronic structure and optical response of rutile, anatase and brookite TiO₂. *Journal of Physics: Condensed Matter*, 24(19):195503, may 2012.
- [15] Jonathan D. B. Bradley, Christopher C. Evans, Jennifer T. Choy, Orad Reshef, Parag B. Deotare, François Parsy, Katherine C. Phillips, Marko Lončar, and Eric Mazur. Submicrometer-wide amorphous and polycrystalline anatase TiO₂ waveguides for microphotonic devices. *Optics Express*, 20(21):23821–31, oct 2012.
- [16] Stephen R. Friberg and Peter W. Smith. Nonlinear optical glasses for ultra-fast optical switches. *IEEE Journal of Quantum Electronics*, 23(12):2089–2094, 1987.
- [17] Christopher C. Evans, Jonathan D. B. Bradley, Erwin A. Martí-Panameño, and Eric Mazur. Mixed two- and three-photon absorption in bulk rutile (TiO₂) around 800 nm. *Optics Express*, 20(3):3118–3128, 2012.
- [18] Stefan Wiechmann and Jörg Müller. Thermo-optic properties of TiO₂, Ta₂O₅ and Al₂O₃ thin films for integrated optics on silicon. *Thin Solid Films*, 517(24):6847–6849, oct 2009.
- [19] Biswajeet Guha, Jaime Cardenas, and Michal Lipson. Athermal silicon microring resonators with titanium oxide cladding. *Optics Express*, 21(22):26557–26563, 2013.
- [20] Zhiyi Zhang, Ping Zhao, Peng Lin, and Fengguo Sun. Thermo-optic coefficients of polymers for optical waveguide applications. *Polymer*, 47(14):4893–4896, jun 2006.
- [21] Alexander Y. Piggott, Jesse Lu, Konstantinos G. Lagoudakis, Jan Petykiewicz, Thomas M. Babinec, and Jelena Vučković. Inverse design and demonstration of a compact and broadband on-chip wavelength demultiplexer. *Nature Photonics*, 9(May):374–377, 2015.

- [22] Qian Zhao, Ji Zhou, Fuli Zhang, and Didier Lippens. Mie resonance-based dielectric metamaterials. *Materials Today*, 12(12):60–69, 2009.
- [23] D. Schurig, J. J. Mock, B. J. Justice, S. A. Cummer, J. B. Pendry, A. F. Starr, and D. R. Smith. Metamaterial electromagnetic cloak at microwave frequencies. *Science*, 314(5801):977–980, 2006.
- [24] Henri J. Lezec, Jennifer A. Dionne, and Harry A. Atwater. Negative refraction at visible frequencies. *Science*, 316(5823):430–432, 2007.
- [25] Jason Valentine, Shuang Zhang, Thomas Zentgraf, Erick Ulin-Avila, Dentcho A. Genov, Guy Bartal, and Xiang Zhang. Three-dimensional optical metamaterial with a negative refractive index. *Nature*, 455(7211):376–379, 2008.
- [26] M. Decker, M. Ruther, C. E. Kriegler, J. Zhou, C. M. Soukoulis, S. Linden, and M. Wegener. Strong optical activity from twisted-cross photonic metamaterials. *Optics Letters*, 34(16):2501–2503, 2009.
- [27] Yonghao Cui, Lei Kang, Shoufeng Lan, Sean Rodrigues, and Wenshan Cai. Giant chiral optical response from a twisted-arc metamaterial. *Nano Letters*, 14(2):1021–1025, feb 2014.
- [28] Romain Fleury and Andrea Alu. Enhanced superradiance in epsilon-near-zero plasmonic channels. *Physical Review B*, 87(20):1–5, 2013.
- [29] Mário Silveirinha and Nader Engheta. Tunneling of electromagnetic energy through subwavelength channels and bends using ϵ -near-zero materials. *Physical Review Letters*, 97(15):1–4, 2006.
- [30] Mário G. Silveirinha and Nader Engheta. Theory of supercoupling, squeezing wave energy, and field confinement in narrow channels and tight bends using ϵ -near-zero metamaterials. *Physical Review B*, 76(24):245109, dec 2007.
- [31] Mário G. Silveirinha, Andrea Alù, Brian Edwards, and Nader Engheta. Overview of Theory and Applications of Epsilon-Near-Zero Materials. 2008.
- [32] Mohammad Memarian and George V. Eleftheriades. Dirac leaky-wave antennas for continuous beam scanning from photonic crystals. *Nature Communications*, 6:5855, jan 2015.
- [33] You Zhou, Xin-Tao He, Fu-Li Zhao, and Jian-Wen Dong. Proposal for achieving in-plane magnetic mirrors by silicon photonic crystals. *Optics Letters*, 41(10):2209–2212, 2016.

- [34] Haim Suchowski, Kevin O'Brien, Zi Jing Wong, Alessandro Salandrino, Xiaobo Yin, and Xiang Zhang. Phase mismatch-free nonlinear propagation in optical zero-index materials. *Science*, 342(6163):1223–1226, 2013.
- [35] M. Zahirul Alam, Israel De Leon, and Robert W. Boyd. Large optical nonlinearity of indium tin oxide in its epsilon-near-zero region. *Science*, 352(6287):795–797, may 2016.
- [36] T. J. Kippenberg, R. Holzwarth, and S. A. Diddams. Microresonator-based optical frequency combs. *Science*, 332(6029):555–559, 2011.
- [37] Anthony E. Siegman. *Lasers*. University Science Books, Sausalito, CA, revised edition, 1986.
- [38] Jennifer T. Choy, Jonathan D. B. Bradley, Parag B. Deotare, Ian B. Burgess, Christopher C. Evans, Eric Mazur, and Marko Lončar. Integrated TiO₂ resonators for visible photonics. *Optics Letters*, 37(4):539–541, 2012.
- [39] L. E. Ocola and A. Stein. Effect of cold development on improvement in electron-beam nanopatterning resolution and line roughness. *Journal of Vacuum Science & Technology B: Microelectronics and Nanometer Structures*, 24(6):3061, 2006.
- [40] Marko Lončar, Dušan Nedeljković, Theodor Doll, Jelena Vučković, Axel Scherer, and Thomas P. Pearsall. Waveguiding in planar photonic crystals. *Applied Physics Letters*, 77(13):1937, 2000.
- [41] Matthew Borselli, Thomas J. Johnson, and Oskar Painter. Beyond the Rayleigh scattering limit in high-Q silicon microdisks: theory and experiment. *Optics Express*, 13(5):1515–1530, 2005.
- [42] Wenshan Cai and Vladimir Shalaev. *Optical Metamaterials*. Springer, New York, NY, 2010.
- [43] Raji Shankar, Irfan Bulu, and Marko Lončar. Integrated high-quality factor silicon-on-sapphire ring resonators for the mid-infrared. *Applied Physics Letters*, 102(5):051108, 2013.
- [44] Kevin O'Brien, Haim Suchowski, Junsuk Rho, Alessandro Salandrino, Boubacar Kante, Xiaobo Yin, and Xiang Zhang. Predicting nonlinear properties of metamaterials from the linear response. *Nature Materials*, 14:379–383, 2015.
- [45] Christopher C. Evans, Katia Shtyrkova, Orad Reshef, Michael Moebius, Jonathan D. B. Bradley, Sarah Griesse-Nascimento, Erich Ippen, and

- Eric Mazur. Multimode phase-matched third-harmonic generation in sub-micrometer-wide anatase TiO₂ waveguides. *Optics Express*, 23(6):7832–7841, 2015.
- [46] Timothy Lee, Neil G. R. Broderick, and Gilberto Brambilla. Resonantly enhanced third harmonic generation in microfiber loop resonators. *Journal of the Optical Society of America B*, 30(3):505, feb 2013.
- [47] M. D. Henry, S. Walavalkar, A. Homyk, and A. Scherer. Alumina etch masks for fabrication of high-aspect-ratio silicon micropillars and nanopillars. *Nanotechnology*, 20(25):255305, 2009.
- [48] Michael J. Burek, Nathalie P. de Leon, Brendan J. Shields, Birgit J. M. Hausmann, Yiwen Chu, Qimin Quan, Alexander S. Zibrov, Hongkun Park, Mikhail D. Lukin, and Marko Lončar. Free-standing mechanical and photonic nanostructures in single-crystal diamond. *Nano Letters*, 12(12):6084–6089, 2012.
- [49] Alexander A. High, Robert C. Devlin, Alan Dibos, Mark Polking, Dominik S. Wild, Janos Perczel, Nathalie P. de Leon, Mikhail D. Lukin, and Hongkun Park. Visible-frequency hyperbolic metasurface. *Nature*, 522(7555):192–196, 2015.
- [50] Masayuki Furuhashi, Masazumi Fujiwara, Takahito Ohshiro, Makusu Tsutsui, Kazuki Matsubara, Masateru Taniguchi, Shigeki Takeuchi, and Tomoji Kawai. Development of microfabricated TiO₂ channel waveguides. *AIP Advances*, 1(3):32102–32105, 2011.
- [51] C. D. W. Wilkinson and M. Rahman. Dry etching and sputtering. *Philosophical Transactions of the Royal Society A: Mathematical, Physical and Engineering Sciences*, 362(1814):125–138, jan 2004.
- [52] F. Simescu, D. Coiffard, M. Lazar, P. Brosselard, and D. Planson. Study of trenching formation during SF₆/O₂ reactive ion etching of 4H-SiC. *Journal of optoelectronics and advanced materials*, 12(3):766–769, 2010.
- [53] Orad Reshef, Katia Shtyrkova, Michael G. Moebius, Sarah Griesse-Nascimento, Steven Spector, Christopher C. Evans, Erich Ippen, and Eric Mazur. Polycrystalline anatase titanium dioxide microring resonators with negative thermo-optic coefficient. *Journal of the Optical Society of America B*, 32(11):2288–2293, nov 2015.
- [54] Markus Häyrynen, Matthieu Roussey, Vishal Gandhi, Petri Stenberg, Antti Säynätjoki, Lasse Karvonen, Markku Kuittinen, and Seppo Honkanen. Low-loss titanium dioxide strip waveguides fabricated by atomic layer deposition. *Journal of Lightwave Technology*, 32(2):208–212, jan 2014.

- [55] Masayuki Furuhashi, Masazumi Fujiwara, Takahito Ohshiro, Kazuki Matsubara, Makusu Tsutsui, Masateru Taniguchi, Shigeki Takeuchi, and Tomoji Kawai. Embedded TiO₂ waveguides for sensing nanofluorophores in a microfluidic channel. *Applied Physics Letters*, 101(15):153115, 2012.
- [56] Feng Qiu, Andrew M. Spring, Feng Yu, Isao Aoki, Akira Otomo, and Shiyoshi Yokoyama. Thin TiO₂ core and electro-optic polymer cladding waveguide modulators. *Applied Physics Letters*, 102(23):233504, 2013.
- [57] Junsoo Park, Sahin Kaya Ozdemir, Faraz Monifi, Tandeep Chadha, Steven He Huang, Pratim Biswas, and Lan Yang. Titanium dioxide whispering gallery microcavities. *Advanced Optical Materials*, 2(8):711–717, jun 2014.
- [58] Zhuan-Fang Bi, Lei Wang, Xiu-Hong Liu, Shao-Mei Zhang, Ming-Ming Dong, Quan-Zhong Zhao, Xiang-Long Wu, and Ke-Ming Wang. Optical waveguides in TiO₂ formed by He ion implantation. *Optics Express*, 20(6):6712–9, mar 2012.
- [59] Christopher C. Evans, Chengyu Liu, and Jin Suntivich. Low-loss titanium dioxide waveguides and resonators using a dielectric lift-off fabrication process. *Optics Express*, 23(9):11160, 2015.
- [60] Adrien Borne, Patricia Segonds, Benoit Boulanger, Corinne Félix, and Jérôme Debray. Refractive indices, phase-matching directions and third order nonlinear coefficients of rutile TiO₂ from third harmonic generation. *Optical Materials Express*, 2(12):1797, nov 2012.
- [61] Christopher C. Evans, Katia Shtyrkova, Jonathan D. B. Bradley, Orad Reshef, Erich Ippen, and Eric Mazur. Spectral broadening in anatase titanium dioxide waveguides at telecommunication and near-visible wavelengths. *Optics Express*, 21(15):18582–18591, 2013.
- [62] Jock Bovington, Rui Wu, Kwang-Ting Cheng, and John E. Bowers. Thermal stress implications in athermal TiO₂ waveguides on a silicon substrate. *Optics Express*, 22(1):661–6, jan 2014.
- [63] Stevan S. Djordjevic, Kuanping Shang, Binbin Guan, Stanley T. S. Cheung, Ling Liao, Juthika Basak, Hai-Feng Liu, and S. J. B. Yoo. CMOS-compatible, athermal silicon ring modulators clad with titanium dioxide. *Optics Express*, 21(12):13958–13968, 2013.
- [64] S. Feng, K. Shang, J. T. Bovington, R. Wu, K-T. Cheng, J. E. Bowers, and S. J. B. Yoo. Athermal characteristics of TiO₂-clad silicon waveguides at 1.3μm. In *IEEE Photonics Conference*, volume 3, pages 116–117, San Diego, California, dec 2014. IEEE.

- [65] Fan Zhang, Rong-Jun Zhang, Dong-Xu Zhang, Zi-Yi Wang, Ji-Ping Xu, Yu-Xiang Zheng, Liang-Yao Chen, Ren-Zhong Huang, Yan Sun, Xin Chen, Xiang-Jian Meng, and Ning Dai. Temperature-dependent optical properties of titanium oxide thin films studied by spectroscopic ellipsometry. *Applied Physics Express*, 6(12):121101, dec 2013.
- [66] Feng Qiu, Andrew M. Spring, and Shiyoshi Yokoyama. Athermal and high-Q hybrid TiO₂ - Si₃N₄ ring resonator via an etching-free fabrication technique. *ACS Photonics*, 2(3):405–409, mar 2015.
- [67] Payam Alipour, Ehsan Shah Hosseini, Ali Asghar Eftekhar, Babak Momeni, and Ali Adibi. Athermal performance in high-Q polymer-clad silicon microdisk resonators. *Optics Letters*, 35(20):3462–4, oct 2010.
- [68] Kyle Preston, Bradley Schmidt, and Michal Lipson. Polysilicon photonic resonators for large-scale 3D integration of optical networks. *Optics Express*, 15(25):17283–90, dec 2007.
- [69] Richard J. Colton, Alberto M. Guzman, and J. Wayne Rabalais. Photochromism and electrochromism in amorphous transition metal oxide films. *Accounts of Chemical Research*, 11:170–176, 1978.
- [70] Yoshihisa Ohko, Tetsu Tatsuma, Tsuyoshi Fujii, Kenji Naoi, Chisa Niwa, Yoshinobu Kubota, and Akira Fujishima. Multicolour photochromism of TiO₂ films loaded with silver nanoparticles. *Nature Materials*, 2(1):29–31, jan 2003.
- [71] Amnon Yariv. Universal relations for coupling of optical power between microresonators and dielectric waveguides. *Electronics Letters*, 36(4):321–322, 2000.
- [72] John E. Heebner, Vincent Wong, Aaron Schweinsberg, Robert W. Boyd, and Deborah J. Jackson. Optical transmission characteristics of fiber ring resonators. *IEEE Journal of Quantum Electronics*, 40(6):726–730, 2004.
- [73] W. R. McKinnon, D. X. Xu, C. Storey, E. Post, A. Densmore, A. Delâge, P. Waldron, J. H. Schmid, and S. Janz. Extracting coupling and loss coefficients from a ring resonator. *Optics Express*, 17(21):18971–82, oct 2009.
- [74] Shanhui Fan. Sharp asymmetric line shapes in side-coupled waveguide-cavity systems. *Applied Physics Letters*, 80(6):908, 2002.
- [75] Ting Hu, Ping Yu, Chen Qiu, Huiye Qiu, Fan Wang, Mei Yang, Xiaoqing Jiang, Hui Yu, and Jianyi Yang. Tunable Fano resonances based on two-beam interference in microring resonator. *Applied Physics Letters*, 102(1):011112, 2013.

- [76] Feng Qiu, Andrew M. Spring, Feng Yu, and Shiyoshi Yokoyama. Complementary metal-oxide-semiconductor compatible athermal silicon nitride/titanium dioxide hybrid micro-ring resonators. *Applied Physics Letters*, 102:051106, 2013.
- [77] Yasumasa Okada and Yozo Tokumaru. Precise determination of lattice parameter and thermal expansion coefficient of silicon between 300 and 1500 K. *Journal of Applied Physics*, 56(1984):314–320, 1984.
- [78] Ling Liao, Desmond R. Lim, Anuradha M. Agarwal, Xiaoman Duan, Kevin K. Lee, and Lionel C. Kimerling. Optical transmission losses in polycrystalline silicon strip waveguides: effects of waveguide dimensions, thermal treatment, hydrogen passivation, and wavelength. *Journal of Electronic Materials*, 29(12):1380–1386, 2000.
- [79] K. T. Vu and S. J. Madden. Reactive ion etching of tellurite and chalcogenide waveguides using hydrogen, methane, and argon. *Journal of Vacuum Science & Technology A: Vacuum, Surfaces, and Films*, 29(1):011023, jan 2011.
- [80] B. J. M. Hausmann, I. Bulu, V. Venkataraman, P. Deotare, and Marko Lončar. Diamond nonlinear photonics. *Nature Photonics*, 8(5):369–374, apr 2014.
- [81] Jacob S. Levy, Mark A. Foster, Alexander L. Gaeta, and Michal Lipson. Harmonic generation in silicon nitride ring resonators. *Optics Express*, 19(12):11415–21, jun 2011.
- [82] B. E. Little, S. T. Chu, H. A. Haus, J. Foresi, and J. P. Laine. Microring resonator channel dropping filters. *Journal of Lightwave Technology*, 15(6):998–1005, 1997.
- [83] Tymon Barwicz, Milos Popović, Peter Rakich, Michael Watts, Hermann Haus, Erich Ippen, and Henry Smith. Microring-resonator-based add-drop filters in SiN: fabrication and analysis. *Optics Express*, 12(7):1437–1442, 2004.
- [84] Robert W. Boyd, Daniel J. Gauthier, and Alexander L. Gaeta. Applications of slow light in telecommunications. *Optics & Photonic News*, 17(4):18, 2006.
- [85] Vilson R. Almeida, Carlos A. Barrios, Roberto R. Panepucci, and Michal Lipson. All-optical control of light on a silicon chip. *Nature*, 431(October):1081–1084, 2004.
- [86] Po Dong, Stefan F. Preble, and Michal Lipson. All-optical compact silicon comb switch. *Optics Express*, 15(15):9600, 2007.
- [87] John E. Heebner, Robert W. Boyd, and Q-Han Park. Slow light, induced dispersion, enhanced nonlinearity, and optical solitons in a resonator-array waveguide. *Physical Review E*, 65(3):036619, 2002.

- [88] Mark A. Foster, Amy C. Turner, Jay E. Sharping, Bradley S. Schmidt, Michal Lipson, and Alexander L. Gaeta. Broad-band optical parametric gain on a silicon photonic chip. *Nature*, 441(7096):960–963, 2006.
- [89] Yoshitomo Okawachi, Kasturi Saha, Jacob S. Levy, Y. Henry Wen, Michal Lipson, and Alexander L. Gaeta. Octave-spanning frequency comb generation in a silicon nitride chip. *Optics Letters*, 36(17):3398–3400, 2011.
- [90] Boris Luk'yanchuk, Nikolay I. Zheludev, Stefan A. Maier, Naomi J. Halas, Peter Nordlander, Harald Giessen, and Chong Tow Chong. The Fano resonance in plasmonic nanostructures and metamaterials. *Nature Materials*, 9(9):707–715, 2010.
- [91] John E. Heebner and Robert W. Boyd. Enhanced all-optical switching by use of a nonlinear fiber ring resonator. *Optics Letters*, 24(12):847–849, 1999.
- [92] Vilson R. Almeida and Michal Lipson. Optical bistability on a silicon chip. *Optics Letters*, 29(20):2387–2389, 2004.
- [93] W. Bogaerts, P. De Heyn, T. Van Vaerenbergh, K. De Vos, S. Kumar Selvaraja, T. Claes, P. Dumon, P. Bienstman, D. Van Thourhout, and R. Baets. Silicon microring resonators. *Laser & Photonics Reviews*, 6(1):47–73, 2012.
- [94] Amnon Yariv. *Optical electronics*. Saunders College Publishing, Philadelphia, 4th edition, 1991.
- [95] Manfred Hammer and Olena V. Ivanova. Effective index approximations of photonic crystal slabs: a 2-to-1-D assessment. *Optical and Quantum Electronics*, 41(4):267–283, mar 2009.
- [96] Yurii Vlasov and Sharee McNab. Losses in single-mode silicon-on-insulator strip waveguides and bends. *Optics Express*, 12(8):1622–1631, 2004.
- [97] Xueqin Huang, Yun Lai, Zhi Hong Hang, Huihuo Zheng, and C. T. Chan. Dirac cones induced by accidental degeneracy in photonic crystals and zero-refractive-index materials. *Nature Materials*, 10(8):582–586, 2011.
- [98] Parikshit Moitra, Yuanmu Yang, Zachary Anderson, Ivan I. Kravchenko, Dayrl P. Briggs, and Jason Valentine. Realization of an all-dielectric zero-index optical metamaterial. *Nature Photonics*, 7(10):791–795, aug 2013.
- [99] Yang Li, Shota Kita, Philip Muñoz, Orad Reshef, Daryl I. Vulis, Mei Yin, Marko Lončar, and Eric Mazur. On-chip zero-index metamaterials. *Nature Photonics*, 9(11):738–742, oct 2015.

- [100] Shota Kita, Yang Li, Philip Muñoz, Orad Reshef, Daryl Vulis, Bobby Day, Charles Lieber, Eric Mazur, and Marko Lončar. On-chip super-robust all-dielectric zero-index material. In *CLEO: Quantum Electronics and Laser Science*, page FM3C.2, San Jose, California, 2015. Optical Society of America.
- [101] Daryl I. Vulis, Orad Reshef, Philip Muñoz, Shota Kita, Yang Li, Marko Lončar, and Eric Mazur. Integrated super-couplers based on zero-index metamaterials. In Said Zouhdi and Vinod M. Menon, editors, *META Conference*, pages 823–833, New York, NY, 2015. Maney Publishing.
- [102] Orad Reshef, Yang Li, Mei Yin, Lysander Christakis, Daryl I. Vulis, Philip Camayd-Muñoz, Shota Kita, Marko Lončar, and Eric Mazur. Phase-matching in Dirac-dome-based zero-index metamaterials. In *CLEO: Applications and Technology*, page jTu5A.53, San Jose, California, 2016. Optical Society of America.
- [103] Ahmed M. Mahmoud and Nader Engheta. Wave-matter interactions in epsilon-and-mu-near-zero structures. *Nature Communications*, 5:5638, dec 2014.
- [104] P. Kaspar, R. Kappeler, D. Erni, and H. Jäckel. Relevance of the light line in planar photonic crystal waveguides with weak vertical confinement. *Optics Express*, 19(24):24344, 2011.
- [105] Wim Bogaerts, Roel Baets, Pieter Dumon, Vincent Wiaux, Stephan Beckx, Dirk Taillaert, Bert Luyssaert, Joris Van Campenhout, Peter Bienstman, and Dries Van Thourhout. Nanophotonic waveguides in silicon-on-insulator fabricated with CMOS technology. *Journal of Lightwave Technology*, 23(1):401–412, 2005.
- [106] Bo Zhen, Chia Wei Hsu, Yuichi Igarashi, Ling Lu, Ido Kaminer, Adi Pick, Song-Liang Chua, John D. Joannopoulos, and Marin Soljačić. Spawning rings of exceptional points out of Dirac cones. *Nature*, 525(7569):354–358, sep 2015.
- [107] D. R. Smith, D. C. Vier, Th. Koschny, and C. M. Soukoulis. Electromagnetic parameter retrieval from inhomogeneous metamaterials. *Physical Review E*, 71(3):036617, 2005.
- [108] S. Kocaman, M. S. Aras, P. Hsieh, J. F. McMillan, C. G. Biris, N. C. Panoiu, M. B. Yu, D. L. Kwong, A. Stein, and C. W. Wong. Zero phase delay in negative-refractive-index photonic crystal superlattices. *Nature Photonics*, 5(8):499–505, jul 2011.
- [109] Kevin O'Brien, N. D. Lanzillotti-Kimura, Haim Suchowski, Boubacar Kante, Yongshik Park, Xiaobo Yin, and Xiang Zhang. Reflective interferometry for optical metamaterial phase measurements. *Optics Letters*, 37(19):4089, 2012.

- [110] Chia Wei Hsu, Bo Zhen, Jeongwon Lee, Song-Liang Chua, Steven G. Johnson, John D. Joannopoulos, and Marin Soljačić. Observation of trapped light within the radiation continuum. *Nature*, 499(7457):188–91, jul 2013.
- [111] Yi Yang, Chao Peng, Yong Liang, Zhengbin Li, and Susumu Noda. Analytical perspective for bound states in the continuum in photonic crystal slabs. *Physical Review Letters*, 113(3):1–5, 2014.
- [112] Philip Muñoz, Shota Kita, Olivia Mello, Orad Reshef, Daryl I. Vulis, Yang Li, Marko Loncar, and Eric Mazur. Lossless integrated Dirac-cone metamaterials. In *CLEO: Applications and Technology*, page JW2A.24, San Jose, California, 2016. Optical Society of America.
- [113] D. F. Walls. Squeezed states of light. *Nature*, 306(5939):141–146, nov 1983.
- [114] Hans-Albert Bachor and Timothy C. Ralph. *A guide to experiments in quantum optics*. Wiley, Berlin, Germany, 2nd edition, 2004.
- [115] Paul G. Kwiat, Klaus Mattle, Harald Weinfurter, Anton Zeilinger, Alexander V. Sergienko, and Yanhua Shih. New high-intensity source of polarization-entangled photon pairs. *Physical Review Letters*, 75(24):4337–4341, 1995.
- [116] Anton Zeilinger, Michael A. Horne, Harald Weinfurter, and Marek Zukowski. Three-particle entanglements from two entangled pairs. *Physical Review B*, 78(16):3031–3034, 1997.
- [117] Dik Bouwmeester, J. W. Pan, Matthew Daniell, Harald Weinfurter, and Anton Zeilinger. Observation of three-photon Greenberger-Horne-Zeilinger entanglement. *Physical Review Letters*, 82(7):1345–1349, 1999.
- [118] Lothar Schermelleh, Rainer Heintzmann, and Heinrich Leonhardt. A guide to super-resolution fluorescence microscopy. *The Journal of Cell Biology*, 190(2):165–175, jul 2010.
- [119] Mats G. L. Gustafsson. Nonlinear structured-illumination microscopy: wide-field fluorescence imaging with theoretically unlimited resolution. *Proceedings of the National Academy of Sciences of the United States of America*, 102(37):13081–13086, 2005.
- [120] Shaul Mukamel. *Principles of nonlinear optical spectroscopy*. Oxford University Press, New York, NY, paperback edition, 1999.
- [121] Norman B. Colthup, Lawrence H. Daly, and Stephen E. Wiberley. *Introduction to infrared and Raman spectroscopy*. Academic Press, New York, NY, 2nd edition, 1975.

- [122] K. M. Davis, K. Miura, N. Sugimoto, and K. Hirao. Writing waveguides in glass with a femtosecond laser. *Optics Letters*, 21(21):1729, 1996.
- [123] Rafael R. Gattass and Eric Mazur. Femtosecond laser micromachining in transparent materials. *Nature Photonics*, 2(4):219–225, 2008.
- [124] Joachim Fischer and Martin Wegener. Three-dimensional optical laser lithography beyond the diffraction limit. *Laser & Photonics Reviews*, 7(1):22–44, 2013.
- [125] J. E. Midwinter and J. Warner. The effects of phase matching method and of uniaxial crystal symmetry on the polar distribution of second-order non-linear optical polarization. *British Journal of Applied Physics*, 16:1135, 1965.
- [126] M. Yamada, N. Nada, M. Saitoh, and K. Watanabe. First-order quasi-phase matched LiNbO₃ waveguide periodically poled by applying an external field for efficient blue second-harmonic generation. *Applied Physics Letters*, 62:435–436, 1993.
- [127] J. A. Armstrong, N. Bloembergen, J. Ducuing, and P. S. Pershan. Interactions between light waves in a nonlinear dielectric. *Physical Review*, 127:1918–1939, 1962.
- [128] Mark A. Foster, Amy C. Turner, Michal Lipson, and Alexander L. Gaeta. Nonlinear optics in photonic nanowires. *Optics Express*, 16(2):1300–1320, 2008.
- [129] M. G. Moebius, F. Herrera, S. Griesse-Nascimento, O. Reshef, C. C. Evans, G. G. Guerreschi, A. Aspuru-Guzik, and E. Mazur. Efficient photon triplet generation in integrated nanophotonic waveguides. *Optics Express*, 24(9):9932–9954, 2016.
- [130] A. K. Popov, V. V. Slabko, and V. M. Shalaev. Second harmonic generation in left-handed metamaterials. *Laser Physics Letters*, 3:293, 2006.
- [131] A. K. Popov and V. M. Shalaev. Negative-index metamaterials: second-harmonic generation, Manley-Rowe relations and parametric amplification. *Applied Physics B*, 84(1-2):131–137, jul 2006.
- [132] Alec Rose and David R. Smith. Overcoming phase mismatch in nonlinear metamaterials. *Optical Materials Express*, 1(7):1232–1243, 2011.
- [133] Jongwon Lee, Mykhailo Tymchenko, Christos Argyropoulos, Pai-Yen Chen, Feng Lu, Frederic Demmerle, Gerhard Boehm, Markus-Christian Amann, Andrea Alù, and Mikhail A. Belkin. Giant nonlinear response from plasmonic metasurfaces coupled to intersubband transitions. *Nature*, 511(7507):65–9, 2014.

- [134] Nadav Segal, Shay Keren-Zur, Netta Hendler, and Tal Ellenbogen. Controlling light with metamaterial-based nonlinear photonic crystals. *Nature Photonics*, 9(3):180–184, 2015.
- [135] Guixin Li, Shumei Chen, Nitipat Pholchai, Bernhard Reineke, Polis Wing Han Wong, Edwin Yue Bun Pun, Kok Wai Cheah, Thomas Zentgraf, and Shuang Zhang. Continuous control of the nonlinearity phase for harmonic generations. *Nature Materials*, 14(6):607–612, apr 2015.
- [136] Euclides Almeida, Guy Shalem, and Yehiam Prior. Subwavelength nonlinear phase control and anomalous phase matching in plasmonic metasurfaces. *Nature Communications*, 7(10367):1–7, 2016.
- [137] Jongwon Lee, Nishant Nookala, J. Sebastian Gomez-Diaz, Mykhailo Tymchenko, Frederic Demmerle, Gerhard Boehm, Markus-Christian Amann, Andrea Alù, and Mikhail A. Belkin. Ultrathin second-harmonic metasurfaces with record-high nonlinear optical response. *Advanced Optical Materials*, 4(5):664–670, may 2016.
- [138] Shoufeng Lan, Lei Kang, David T. Schoen, Sean P. Rodrigues, Yonghao Cui, Mark L. Brongersma, and Wenshan Cai. Backward phase-matching for nonlinear optical generation in negative-index materials. *Nature Materials*, 14(8):807–811, jun 2015.
- [139] Jonas Hansryd, Peter A. Andrekson, Mathias Westlund, Jie Li, and Per Olof Hedekvist. Fiber-based optical parametric amplifiers and their applications. *IEEE Journal on Selected Topics in Quantum Electronics*, 8(3):506–520, 2002.
- [140] M. A. Foster, K. D. Moll, and Alexander L. Gaeta. Optimal waveguide dimensions for nonlinear interactions. *Optics Express*, 12(13):2880–2887, 2004.
- [141] Rafael R. Gattass, Geoffry T. Svacha, Limin Tong, and Eric Mazur. Supercontinuum generation in submicrometer diameter silica fibers. *Optics Express*, 14(20):9408–9414, 2006.
- [142] Amy C. Turner, Christina Manolatou, Bradley S. Schmidt, Michal Lipson, Mark A. Foster, Jay E. Sharping, and Alexander L. Gaeta. Tailored anomalous group-velocity dispersion in silicon channel waveguides. *Optics Express*, 14(10):4357–4362, 2006.
- [143] Sangsik Kim, Kyunghun Han, Cong Wang, Jose A. Jaramillo-Villegas, Xiaoxiao Xue, Chengying Bao, Yi Xuan, Daniel E. Leaird, Andrew M. Weiner, and Ming-hao Qi. Frequency comb generation in 300 nm thick SiN concentric-racetrack-resonators: overcoming the material dispersion limit. arXiv:1607.01850, jul 2016.

- [144] Lin Zhang, Yang Yue, Yinying Xiao-Li, Jian Wang, Raymond G. Beausoleil, and Alan E. Willner. Flat and low dispersion in highly nonlinear slot waveguides. *Optics Express*, 18(12):13187–13193, 2010.
- [145] Dennis M. Sullivan. *Electromagnetic Simulation Using the FDTD Method*. John Wiley & Sons, Inc., Hoboken, NJ, USA, 2nd edition, jun 2013.
- [146] Q. Lin, J. Zhang, G. Piredda, R. W. Boyd, P. M. Fauchet, and G. P. Agrawal. Dispersion of silicon nonlinearities in the near infrared region. *Applied Physics Letters*, 91(2):021111, 2007.
- [147] Christopher C. Evans, Jessica M. R. Burton, Darrell G. Schlom, and Jin Suntivich. Single-crystal titanium dioxide strip-loaded waveguides. In *CLEO: Science and Innovations*, page SF1P.7, San Jose, California, 2016. Optical Society of America.
- [148] Tapani Alasaarela, Lasse Karvonen, Henri Jussila, Antti Säynätjoki, Soroush Mehravar, Robert A. Norwood, Nasser Peyghambarian, Khanh Kieu, Ilkka Tittonen, and Harri Lipsanen. High-quality crystallinity controlled ALD TiO₂ for waveguiding applications. *Optics Letters*, 38(20):3980–3, oct 2013.
- [149] Markus Häyrinen, Matthieu Roussey, Antti Säynätjoki, Markku Kuittinen, and Seppo Honkanen. Titanium dioxide slot waveguides for visible wavelengths. *Applied Optics*, 54(10):2653–2657, 2015.
- [150] Shankar Kumar Selvaraja, Wim Bogaerts, and Dries Van Thourhout. Loss reduction in silicon nanophotonic waveguide micro-bends through etch profile improvement. *Optics Communications*, 284(8):2141–2144, apr 2011.
- [151] Surya Cheemalapati, Mikhail Ladanov, John Winskas, and Anna Pyayt. Optimization of dry etching parameters for fabrication of polysilicon waveguides with smooth sidewall using a capacitively coupled plasma reactor. *Applied Optics*, 53(25):5745–9, 2014.
- [152] Cheng Wang, Michael J. Burek, Zin Lin, Haig A. Atikian, Vivek Venkataraman, I-Chun Huang, Peter Stark, and Marko Lončar. Integrated high quality factor lithium niobate microdisk resonators. *Optics Express*, 22(25):30924–33, 2014.
- [153] Patrik Rath, Svetlana Khasminskaya, Christoph Nebel, Christoph Wild, and Wolfram H. P. Pernice. Diamond-integrated optomechanical circuits. *Nature Communications*, 4:1690, 2013.
- [154] Michael J. Burek, Yiwen Chu, Madelaine S. Z. Liddy, Parth Patel, Jake Rochman, Srujan Meesala, Wooyoung Hong, Qimin Quan, Mikhail D. Lukin, and Marko Lončar. High quality-factor optical nanocavities in bulk single-crystal diamond. *Nature Communications*, 5(617):5718, dec 2014.

- [155] M. V. Gurudev Dutt, L. Childress, L. Jiang, E. Togan, J. Maze, F. Jelezko, A. S. Zibrov, P. R. Hemmer, and M. D. Lukin. Quantum register based on individual electronic and nuclear spin qubits in diamond. *Science*, 316(5829):1312–1316, 2007.
- [156] Birgit J. M. Hausmann, Brendan Shields, Qimin Quan, Patrick Maletinsky, Murray McCutcheon, Jennifer T. Choy, Tom M. Babinec, Alexander Kubanek, Amir Yacoby, Mikhail D. Lukin, and Marko Lončar. Integrated diamond networks for quantum nanophotonics. *Nano Letters*, 12(3):1578–1582, 2012.
- [157] A. Sipahigil, K. D. Jahnke, L. J. Rogers, T. Teraji, J. Isoya, A. S. Zibrov, F. Jelezko, and M. D. Lukin. Indistinguishable photons from separated silicon-vacancy centers in diamond. *Physical Review Letters*, 113(11):1–5, 2014.
- [158] Govind P. Agrawal. *Nonlinear Fiber Optics*. Academic Press, Boston, MA, 4th edition, 2007.